UNIVERSITY of CALIFORNIA
Santa Barbara

Observable Consequences of Rotation for Stars, Brown Dwarfs, and Star Clusters

A dissertation submitted in partial satisfaction of the
requirements for the degree of

Doctor of Philosophy

in

Physics

by

Mikhail Lipatov

Committee in charge:

Professor Timothy D. Brandt, Chair

Professor Andy Howell

Professor Lars Bildsten

September 2022

The dissertation of Mikhail Lipatov is approved:

Professor Andy Howell

Professor Lars Bildsten

Professor Timothy D. Brandt, Chair

September 2022

Observable Consequences of Rotation for

Stars, Brown Dwarfs, and Star Clusters

by

Mikhail Lipatov

To my mom, Yelena Amitina.

Acknowledgements

Technical Acknowledgements and Attributions:

Specific intensities on a grid of plane-parallel atmosphere model parameters form an essential input to software `PARS`. In Chapters 2 and 4, `PARS` uses a publicly available intensity grid for the stellar atmosphere model `ATLAS9` by Castelli & Kurucz (2004). In Chapter 3, `PARS` makes use of an intensity grid for an atmosphere model that is appropriate for brown dwarfs. This grid was kindly provided by Natasha Batalha, who computed the intensities using radiative transfer code `PICASO` (Batalha et al., 2022) and the Sonora brown dwarf 1D climate and chemistry models (Marley et al., 2021).

The analysis in Chapter 4 greatly depends on the `MIST` stellar evolution model library with a range of rotational velocities (Choi et al., 2016; Gossage et al., 2018, 2019). Seth Gossage and Aaron Dotter made `MIST` available for the analysis and specified the physical meaning of several important model parameters. `MIST` is based on the `MESA` stellar evolution code (Paxton et al., 2011, 2013, 2015).

In addition to depending on the stellar evolution models, the analysis in Chapter 4 relies on the spectroscopic rotational velocity measurements for stars in the globular cluster NGC 1846, which were derived by Kamann et al. (2020), based on the data that these authors collected with the Multi Unit Spectroscopic Explorer (`MUSE`) on the Very Large Telescope. Nathan Bastian and Sebastian Kamann graciously provided these data, along with the magnitudes of the corresponding stars. The magnitudes had been previously collected with the Hubble Space Telescope (`HST`).

The work in this thesis makes extensive use of the following `Python` libraries: The NumPy Array (van der Walt et al., 2011), Matplotlib (Hunter, 2007), and SciPy (Virtanen et al., 2020).

Personal Acknowledgements:

First and foremost, I wish to thank my advisor, Dr. Timothy Brandt, for the past four years of guidance and support. Thank you for your patient explanations of difficult concepts in simple an clear language. Thank you for the care with which you fostered my intellectual development, for guiding me in this interesting and important work. The experience of working with you and learning from you is invaluable. I am also extremely grateful to Dr. Lars Bildsten and the members of his group, who welcomed me at their group meetings and helped me understand the inner workings of stars. I thank the organizers and the participants of Astro Tea, the physics department's astrophysics journal club, for creating and maintaining a terrific environment where people can share in the excitement about ground-breaking astrophysics research.

I want to thank my wonderful family for their boundless, unconditional love and support. You are the closest, most important friends I have in this life. Your faith in me carries me through the darkest times, in all my endeavors.

My sincere thanks to Dr. David Weld and the members of his atomic physics laboratory, for giving me an intellectual home in the physics department during the first two years of my PhD. I am especially grateful to Dr. Ruwan Senaratne, Dr. Kevin Singh, and Dr. Cora Fujiwara, who were my principal mentors in the Weld lab during that time.

Finally, I want to thank my graduate student friends Dr. Melissa Quinnan, Jamie Burke, Dr. Jared Goldberg, Will Schultz, and Sunny Wong. Thank you for your camaraderie, for listening to me ramble, for sharing the experience of this doctoral program with me.

Curriculum Vitæ

Mikhail Lipatov

Education

2022	(Expected) Ph.D., Physics, University of California, Santa Barbara, CA
2020	M.A., Physics, University of California, Santa Barbara, CA
2002	B.A., Physics, Harvard University, Cambridge, MA

Select Publications

"Effects of Rotation on the Spectra of Brown Dwarfs", **M. Lipatov**, T.D. Brandt, and N.E. Batalha *Submitted to Monthly Notices of the Royal Astronomical Society (MNRAS) 2022.*

"Rotational Variation Allows for Narrow Age Spread in the Extended Main Sequence Turnoff of Massive Cluster NGC 1846", **M. Lipatov**, T.D. Brandt, and S. Gossage *ApJ* 934, 105 (2022).

"Synthetic Spectra of Rotating Stars", **M. Lipatov** and T.D. Brandt *ApJ* 901, 100 (2020).

"Quantifying and Controlling Prethermal Nonergodicity in Interacting Floquet Matter", K. Singh, K.M. Fujiwara, Z.A. Geiger, E.Q. Simmons, **M. Lipatov**, A. Cao, P. Dotti, S.V. Rajagopal, R. Senaratne, T. Shimasaki, M. Heyl, A. Eckardt, and D.M. Weld *Phys Rev X* 9:041021 (2019).

"Transport in Floquet-Bloch Bands", K.M. Fujiwara, K. Singh, Z.A. Geiger, R. Senaratne, S.V. Rajagopal, **M. Lipatov**, and D.M. Weld *Phys Rev Lett* 122:010402 (2019).

"Experimental Realization of a Relativistic Harmonic Oscillator", K.M. Fujiwara, Z.A. Geiger, K. Singh, R. Senaratne, S.V. Rajagopal, **M. Lipatov**, T. Shimasaki, and D.M. Weld *New J Phys* 20:063027 (2018).

"Observation and Uses of Position-Space Bloch Oscillations in an Ultracold Gas", Z.A. Geiger, K.M. Fujiwara, K. Singh, R. Senaratne, S.V. Rajagopal, **M. Lipatov**, T. Shimasaki, R. Driben, V.V. Konotop, T. Meier, and D.M. Weld *Phys Rev Lett* 120:213201 (2018).

"Crystallite Size Dependency of Thermal Expansion in Ceria Nanoparticles", P.P. Rodenbough, **M. Lipatov**, S.-W. Chan *Mater Chem Phys* 192:311-316 (2017).

Abstract

Observable Consequences of Rotation for

Stars, Brown Dwarfs, and Star Clusters

by

Mikhail Lipatov

It is reasonable to suppose that a typical newborn star or brown dwarf inherits much of its progenitor molecular cloud's angular momentum. This leads to the suggestion that such an object ought to have a rotational velocity that is close to the Keplerian breakup limit, resulting in significant centrifugal expansion at the equator. According to models of internal energy transport, this expansion ought to make the poles of a rotator significantly hotter than its equator, so that the inclination of its rotational axis greatly affects both the shape of its observed spectrum and its total observed flux. These predictions are consistent with the interferometric and spectroscopic observations of stellar and sub-stellar objects whose rotational speeds are frequently at appreciable fractions of the Keplerian limit.

In particular, the oblate shapes, surface temperature variations, and spectral line broadening of many early-type stars indicate large rotational velocities. Via its effects on surface temperature and shape, rotation has a significant effect on these stars' spectra. Thus, in order to infer the structural and life history parameters of these objects from

their spectra, one must carefully integrate specific intensity over the two-dimensional surfaces of corresponding stellar models. Toward this end, in Chapter 2, we offer `PARS` (Paint the Atmospheres of Rotating Stars) – an integration scheme based on models that incorporate solid body rotation, Roche mass distribution, and collinearity of gravity and energy flux (Lipatov & Brandt, 2020a). The scheme features a closed-form expression for the azimuthal integral, a high-order numerical approximation of the longitudinal integral, and a precise calculation of surface effective temperature at rotation rates up to 99.9% of the Keplerian limit. Extensions of the scheme include synthetic color-magnitude diagrams and planetary transit curves. An important input to `PARS` in Chapter 2 is a grid of specific intensities for stellar plane-parallel atmosphere models, `ATLAS9`.

Much like the observations of early-type stars, spectroscopy and time-resolved photometry of brown dwarfs are frequently indicative of rotational velocities that are comparable to the breakup limit. Accordingly, in Chapter 3, we apply `PARS` to parameter inference in the case of rotating brown dwarfs, exploring the dependence of these substellar objects' observables on rotational speed and axis inclination. In this case, instead of specific intensities for stellar atmosphere models, we feed `PARS` an intensity grid that is appropriate for brown dwarfs, computed by `PICASO` (a Planetary Intensity Code for Atmospheric Spectroscopy Observations) from Sonora brown dwarf 1D climate and chemistry models. We find that the specific flux of a typical fast-rotating brown dwarf can increase by as much as a factor of 1.5 with movement from an equator-on to a pole-on view. On the other hand, the distinctive effect of rotation on spectral shape increases

toward the equator-on view. The latter effect also increases with lower effective temperature. The bolometric luminosity estimate for a typical fast rotator at extreme inclinations has to be adjusted by as much as $\sim 20\%$ due to the anisotropy of the object's observed flux. We provide a general formula for the calculation of the corresponding adjustment factor in terms of rotational speed and inclination.

Rotation does not only directly affect the spectra of present-day stars, it also significantly alters the evolution of stars throughout their lives, chiefly via its effect on stellar internal transport. By means of both the direct and the evolutionary effects, stellar rotation is possibly responsible for the fact that the color-magnitude diagrams (CMDs) of intermediate-age star clusters ($\lesssim$2 Gyr) are much more complex than those predicted by coeval, non-rotating stellar evolution models. The clusters' observed extended main sequence turnoffs (eMSTOs) could result from variations in stellar age, stellar rotation, or both. The physical interpretation of eMSTOs is largely based on the complex mapping between stellar models—themselves functions of mass, rotation, orientation, and binarity—and the CMD. In Chapter 4, we compute continuous probability densities in three-dimensional color, magnitude, and $v_{\rm e} \sin i$ (i.e., projected equatorial velocity) space for individual stars in a cluster's eMSTO, based on a rotating stellar evolution model. These densities enable the rigorous inference of cluster properties from a stellar model, or, alternatively, constraints on the stellar model from the cluster's CMD. We use the `MIST` stellar evolution models to jointly infer the age dispersion, the rotational distribution, and the binary fraction of the Large Magellanic Cloud cluster NGC 1846. We

derive an age dispersion of $\sim 70-80\,\mathrm{Myr}$, approximately half the earlier estimates due to non-rotating models. This finding agrees with the conjecture that rotational variation is largely responsible for eMSTOs. However, the `MIST` models do not provide a satisfactory fit to all stars in the cluster and achieve their best agreement at an unrealistically high binary fraction. The lack of agreement near the main-sequence turnoff suggests specific physical changes to the stellar evolution models, including a lower mass for the Kraft break and potentially enhanced main sequence lifespans for rapidly rotating stars.

Contents

Chapter 1

Introduction

1.1 Observational Consequences of Stellar Rotation

Advances in optical interferometry over the past two decades enable the resolution of nearby stellar surfaces (Monnier, 2003; Zhao et al., 2010; van Belle, 2012). Corresponding observations reveal that at least 4 of the 15 brightest early-type stars have non-spherical shapes and star-scale variation in surface temperature: Vega (Yoon et al., 2010, henceforth YP10), Achernar (Domiciano de Souza et al., 2014), Altair (Bouchaud et al., 2020, henceforth BD20), and Regulus (Che et al., 2011). Rapid rotation can explain these effects. The polar regions of a spinning star are closer to its core and thus hotter than its equatorial regions (Owocki et al., 1994; von Zeipel, 1924; Cranmer & Owocki, 1995). The Keplerian velocity of such a star provides an upper limit to its surface rotation rate (e.g., Ekström et al., 2008). Vega, Achernar, Altair, and Regulus all have inferred rotation rates between 0.62 and 0.84 of the Keplerian limit, and polar temperatures 23% to

35% hotter than their equatorial temperatures. Here and in the rest of this work, Vega's parameters are from Table 1 with horizontal macroturbulence in YP10, Achernar's are from Domiciano de Souza et al. (2014), Altair's are from Table 5 in BD20, and Regulus's are from Table 4 in Che et al. (2011) with the modified von Zeipel model.

When a star's angular size is too small for interferometric resolution, one can invoke the Doppler effect to infer projected rotation from the broadening of individual spectral lines (Elvey, 1930; Herbig & Spalding, 1955). Interpretation of observations in light of this methodology supports the view that many unresolved early-type stars rotate at significant fractions of the Keplerian limit (Glebocki & Gnacinski, 2005; Díaz et al., 2011; Zorec & Royer, 2012). This, in addition to the effect of rotation on the surface temperatures of resolved stars, implies that rapid rotation frequently affects both spectral energy distributions and absorption line profiles of unresolved stars.

An observer viewing the pole of a spinning star will see a larger, hotter surface in projection than one viewing its equator. Through this effect, stellar rotation can explain color-magnitude diagrams of star clusters with single, coeval populations (Brandt & Huang, 2015a; de Juan Ovelar et al., 2019; Gossage et al., 2019). Models of clusters start with the evolution of individual rotating stars from the zero-age main sequence (ZAMS) to the observed epoch. One then needs to integrate specific intensities over the surfaces of stellar models for comparison with the observed spectra, colors, and magnitudes.

The inhomogeneous surface of a rotating star also affects transit light curves: a misaligned planetary or stellar companion will produce a deeper or shallower transit as it

transits a hotter or cooler part of the star (Barnes, 2009). Computing this effect from a full stellar model requires calculating both the integrated spectrum and the specific intensity along a chord of finite thickness running across the projected stellar surface.

In Chapter 2, we present a fast, flexible, and accurate numerical integration scheme to compute synthetic spectra, color-magnitude diagrams, and transit light curves for rapidly rotating stars. The scheme is embodied in publicly available software `PARS` (Paint the Atmospheres of Rotating Stars). The software and the scheme do not take into account the rotational Doppler effect, so that it is mainly applicable to the inference of rotational parameters from broad spectral features, as opposed to specific absorption lines.

1.2 Rotation of Brown Dwarfs

1.2.1 Brown Dwarf Structure and Evolution

When a portion of a giant molecular cloud collapses to form a single gaseous object, the nature and the fate of that object are mainly determined by its mass. Above $75\,M_{\mathrm{Jup}}$, the object is massive enough that its core temperature and pressure enable the fusion of hydrogen, ^{1}H (Basri, 2000). This, by definition, makes the object a main-sequence star, whose temperature and luminosity remain relatively constant for billions of years – except in the rare case that the star's mass significantly exceeds $1\,M_{\odot}$. Between $13\,M_{\mathrm{Jup}}$ and $75\,M_{\mathrm{Jup}}$, however, the collapsed object cannot fuse ^{1}H, although it can still fuse deuterium, ^{2}H (Saumon et al., 1996). This sort of an object is a brown dwarf (BD).

Infra-red excess from young brown dwarfs indicates the presence of accretion disks. This confirms that BDs are formed via the above-mentioned process of molecular cloud collapse, much like stars (Muench et al., 2001; Natta & Testi, 2001). Regardless of their formation mechanism, objects with mass below $13\,M_{\mathrm{Jup}}$ never achieve nuclear fusion in the core and are classified as planets.

The objects that are intermediate between stars and planets in terms of mass – brown dwarfs – are particularly interesting. No such object exists in our own solar system, though the latter does contain several giant planets and a star. According to the theory of brown dwarf formation and evolution, the surface effective temperature of a typical newly formed BD is in the neighborhood of $\sim$2,500 − 3,000 K (Chabrier & Baraffe, 2000). However, this temperature drops relatively quickly, reaching about 50% of its original value by $\sim$500 Myr as the deuterium content dwindles, even for massive brown dwarfs. The cooling process leads to observed brown dwarf temperatures that are as low as $\sim$250 K for low masses and old ages (Luhman, 2014; Phillips et al., 2020).

If we approximate brown dwarfs as black bodies, Wien's displacement law tells us that these objects' surface temperature drop corresponds to a rise in peak spectral wavelength from $\sim 1\,\mu$m well into the infra-red portion of the spectrum. In addition, the temperature drop corresponds to a drop in luminosity. In particular, luminosities of the heaviest BDs decrease past the luminosities of the least massive main-sequence stars around 1 Gyr (Dantona & Mazzitelli, 1985). It wasn't until relatively recently that astronomical detection technology enabled the observation of such low luminosities in the

infra-red. Accordingly, although the existence of brown dwarfs was predicted in the early 1960's (Kumar, 1963; Hayashi & Nakano, 1963) and although BDs are about as common as stars (Bate et al., 2002), the first object unambiguously classified as a brown dwarf was announced as late as 1995 (Basri, 2000; Nakajima et al., 1995; Oppenheimer et al., 1995).

Models of brown dwarf structure and evolution predict that the radii of these objects are generally close to Jupiter's and that these radii decrease with object age as their interiors cool and electron degeneracy becomes an increasingly important source of pressure support (Baraffe et al., 2003; Saumon & Marley, 2008). The former prediction agrees with the observed brown dwarf radii, which are anywhere between $\sim 0.6\,M_{\rm Jup}$ and $\sim 1.4\,M_{\rm Jup}$ (Sorahana et al., 2013; Carmichael et al., 2020).

Due to their relatively low temperatures, brown dwarf atmospheres exhibit a number of complexities that are not present in the atmospheres of stars. In particular, BD spectra deviate strongly from black body spectra due to prominent molecular absorption features (Allard et al., 1997). Furthermore, clouds can form in the potentially rotating atmospheres, adding further complexity (Ackerman & Marley, 2001; Lew et al., 2020; Tan & Showman, 2021). At any given time point, such atmospheric properties strongly depend on surface effective temperature. The atmosphere of a brown dwarf, in turn, determines the shape of its spectrum and regulates its cooling (Chabrier & Baraffe, 2000; Allard et al., 1997).

1.2.2 Rotating Brown Dwarfs

Brown dwarfs spin at a significant rate due to the angular momentum that they inherit from their progenitor molecular clouds. Specifically, observed rotation periods of newly born BDs are $\sim 100\,\mathrm{hr}$, falling to $\sim 10\,\mathrm{hr}$ by $\sim 100\,\mathrm{Myr}$ due the above-mentioned cooling and contraction process (Eislöffel & Scholz, 2007; Crossfield, 2014). The rotational periods of the fastest-rotating brown dwarfs are as low as $\sim 1\,\mathrm{hr}$, corresponding to significant fractions (up to a third) of the Keplerian breakup velocity (Tannock et al., 2021). As noted in Section 1.1, rotation rates at appreciable fractions of the breakup limit cause centrifugal deformation and surface temperature variation in stars (Monnier et al., 2007; Domiciano de Souza et al., 2014). This, in turn, causes the observed spectra, magnitudes, and bolometric fluxes of stars to depend on the inclination of the rotational axis with respect to the observer (Lipatov & Brandt, 2020b, hereafter LB20). Specifically, the intensity of a typical fast rotating star varies by as much as a factor of 1.5 between the two extreme inclinations in spectral regions with appreciable flux, which corresponds to $\gtrsim 0.3$ in visual magnitude difference. Differences in color and spectral line shape are potentially detectable as well. Rotation is expected to be similarly appreciable in brown dwarfs (e.g., Sanghavi & Shporer, 2018).

Inference of brown dwarf parameters based on model atmospheres yields effective temperatures, surface gravities, radii, and metallicities of these objects (Zhang et al., 2021). Currently, such inference is based on nonrotating, spherically symmetric models with uniform surface temperature, even for objects known to be rotating at significant

fractions of the breakup limit (Tannock et al., 2021; Eislöffel & Scholz, 2007; Crossfield, 2014). This can lead to inaccurate estimation of temperatures and luminosities from BD spectra and bolometric fluxes, since the latter observables depend on rotational axis inclination and since the temperature of a rotating brown dwarf varies significantly across its surface. In Chapter 3, we quantify the dependence of BD observables on rotational speed and object orientation, as well as the associated effect on inferred nonrotating model parameters. To accomplish this, we utilize Sonora brown dwarf 1D climate and chemistry models (Marley et al., 2021), the `PICASO` spectroscopy code (Batalha et al., 2019), and `PARS` (Paint the Atmospheres of Rotating Stars) – software that computes observed spectra of self-gravitating, rotating gaseous objects (LB20).

1.3 Clusters with Rotating Stars

1.3.1 Evolution of Rotating Stars

According to modern physical science, fundamental principles can explain the diversity of observed stars via stellar structure and evolution (Arny, 1990; Christensen-Dalsgaard, 2021). An early manifestation of this idea is the Vogt-Russell theorem, a proposition that a star's chemical composition structure and its initial mass (or, simply, mass) fully determine the course of its life (Kaehler, 1978; Carroll & Ostlie, 2007, p. 333). The addition of rotation to the list of life-determining parameters constitutes an important amendment to this proposition.

Generally speaking, stars rotate. This phenomenon has been observed in the movement of the Sun's spots (Howard et al., 1984), the centrifugally deformed shapes of nearby B- and A-type stars (Monnier et al., 2007; Domiciano de Souza et al., 2014), and spectroscopic rotational velocities of unresolved stars (Royer et al., 2002a,b; Healy & McCullough, 2020). Rotation has important consequences for the evolution and observed properties of stars. It mixes extra hydrogen into the core of a main-sequence star, increasing both its luminosity and lifetime (Brott et al., 2011; Eggenberger, 2013). In addition, as noted in Section 1.1, the equatorial regions of a rotating star are cooler and dimmer than its polar regions due to an effect called gravity darkening (von Zeipel, 1924; Espinosa Lara & Rieutord, 2011). This makes the star's magnitudes and colors depend on the inclination of its axis with respect to the observer (e.g., Lipatov & Brandt, 2020b).

Stars inherit their angular momenta from ancestral clouds of gas and dust (Prentice & Ter Haar, 1971; Tomisaka, 2000; Larson, 2010). Subsequently, their rotational speeds evolve to the present day (Maeder & Meynet, 2000). The speeds extend up to appreciable fractions of the centrifugal breakup limit for stars with mass $\gtrsim 1.5\,M_{\odot}$ (Zorec & Royer, 2012; Kamann et al., 2020). Lower-mass stars, on the other hand, spin down rapidly (e.g., see Figure 11 in Godoy-Rivera et al., 2021). This pattern likely results from the emergence of an outer convective zone that supports magnetic field lines that, in turn, rotate with the star and extend away from it. Stellar wind particles move along these lines, depriving the star of angular momentum. This process, termed magnetic braking, results in the Kraft break – a sharp reduction in observed rotation rates as stellar mass

decreases below $\sim 1.3\,M_{\odot}$ (Kraft, 1967; Noyes et al., 1984). Recent analyses tune models of magnetic braking to clusters, i.e., gravitationally bound collections of stars (Matt et al., 2015; Breimann et al., 2021; Gossage et al., 2021).

1.3.2 Stellar Distributions in Massive Clusters

In this work, we focus on NGC 1846, which belongs to the category of massive ($\gtrsim 10^4\,M_{\odot}$), intermediate-age ($\sim 1-2\,\mathrm{Gyr}$) clusters that reside in the Magellanic Clouds (Bastian & Niederhofer, 2015, hereafter BN15). Like other clusters, it offers an opportunity to tune a model of stellar structure and evolution simultaneously to all of its stars, since their shared cluster membership implies that they share some of their life-determining parameters.

For example, if the stars in a cluster are all formed from the collapse and fragmentation of the same giant molecular cloud (Klessen, 2001; Bate et al., 2003), they should all have the same chemical composition. This picture is not entirely true for massive clusters, which can contain multiple populations (MPs) with different chemical compositions (Bastian & Lardo, 2018; Gratton et al., 2012; Piotto, 2009). On the other hand, massive clusters in the Magellanic Clouds generally show insignificant within-cluster departures from uniform iron abundances [Fe/H] (Piatti & Bailin, 2019; Piatti, 2020; Mucciarelli et al., 2008). This suggests that there is not enough variation in chemical composition to produce appreciable variation in stellar evolution within such clusters. Similarly to [Fe/H] distributions, initial mass distributions in clusters are relatively well-known, with

consequently predictable effects on magnitudes and colors. There is evidence that these mass distributions do not differ significantly from the Salpeter initial mass function (IMF) above $\sim$1 $M_{\odot}$ (Salpeter, 1955; Kroupa, 2001; Chabrier, 2003; Villaume et al., 2017).

Unlike [Fe/H] and mass distributions, rotational and age distributions of stars within clusters are not established. Variations in both rotation and age have been invoked to explain the color spreads of the main sequence turnoff (MSTO), termed extended MSTOs (eMSTOs). One of the first eMSTOs was discovered in NGC 1846 (Mackey & Broby Nielsen, 2007). Initial photometry-based analysis led to the hypothesis that this pattern results from a wide stellar age distribution, i.e., an extended star formation (eSF) period (Goudfrooij et al., 2009; Rubele et al., 2013; Goudfrooij et al., 2011b,a). Subsequently, as eMSTOs were discovered in other clusters, it became apparent that age and rotation spreads could both contribute to this phenomenon, making it difficult to distinguish between the two factors from MSTO photometry alone (Bastian & de Mink, 2009; Bastian & Niederhofer, 2015; Brandt & Huang, 2015b; D'Antona et al., 2017). At the same time, eSF ought to have similar effects on different portions of the CMD – e.g., the MSTO, the sub-giant branch (SGB), and the red clump (RC). BN15 show that, even under the assumption of zero rotational variation, the SGB and RC morphologies in NGC 1846 are consistent with zero age spread and are significantly narrower than expected if eSF causes the cluster's eMSTO. BN15 go on to suggest that their results can be explained by a rotational distribution that widens the MSTO, but does not necessarily widen the SGB or the RC.

A variety of additional evidence conflicts with the hypothesis that eSF causes eMSTOs in NGC 1846 and other massive clusters. For example, Niederhofer et al. (2015) show that, under the assumption of zero rotation, age spreads inferred from eMSTOs correlate with cluster age, an observation that is inconsistent with the idea that the age spread of a cluster is set for the duration of its life. Instead, as the authors demonstrate, the observed correlation is in good agreement with the hypothesis that rotation spreads cause eMSTOs. Furthermore, Bastian et al. (2013) examine a number of clusters at one to several tens of Myr (Young Massive Clusters, or YMCs); at these ages, one expects significant star formation under the eSF hypothesis. The authors do not find evidence of such formation in spectral emission lines and constrain the maximum mass of the material that could be undergoing star formation to no more than 1-2 % of the existing stellar mass content. Along the same line of inquiry, Cabrera-Ziri et al. (2015) show that YMCs do not possess the interstellar gas and dust that can form into stars in the course of eSF.

1.3.3 Analysis of Star Clusters

The morphology of the CMD results from the theory of stellar evolution and the properties—mass, age, composition, rotation, and orientation—of individual stars. In order to infer cluster parameters from the CMD, or to tune models of stellar evolution, we need to compare theoretical and observed CMDs either qualitatively or quantitatively. Recent work, which we review here, has advanced toward ever-more rigorous statistical comparisons between theoretical and observed CMDs.

Some statistical approaches infer the parameters of individual stars. For example, Brandt & Huang (2015c, henceforth BH15) infer the ages and other present-day parameters of stars from color, magnitude, and projected rotational velocity, under the assumption of the `SYCLIST` evolutionary model library (Ekström et al., 2012; Georgy et al., 2013). More recently, Cargile et al. (2020, henceforth C20) accomplish this task under the assumption of the `MIST` library (`MESA` Isochrones and Stellar Tracks; Dotter, 2016; Choi et al., 2016; Gossage et al., 2018, 2019) . Both of these star-by-star approaches are Bayesian, with the goal of computing the stellar parameters' joint posterior distribution. Both BH15 and C20 write down the likelihood of stellar parameters in terms of instrumental uncertainty and multiply the likelihood by the parameters' prior. C20 approximate the resulting posterior by way of a Monte Carlo methodology called nested sampling (Speagle, 2020), while BH15 calculate it on a deterministic grid. Both methods can estimate multi-modal and/or highly covariant posteriors more efficiently than conventional Monte Carlo (MC) methodologies, although the deterministic method is only viable when the dimensionality of the posterior is small.

One can also simultaneously infer the parameters of many stars under the assumption that they share the values for some of these parameters (e.g., age and composition). For example, BH15 marginalize the posteriors of many stars over mass, rotation, and orientation to infer shared parameters in a star cluster. Building on earlier work (Zucker et al., 2019; Schlafly et al., 2014; Green et al., 2014), Zucker et al. (2020, henceforth Z20) follow a similar procedure to infer shared parameters for a different sort of object – a

molecular cloud that lies between the stars along lines of sight.

Intuitively, when the posterior is viewed as a probability density in stellar observable space at constant cloud/cluster parameters, parameter likelihood is the product of density values at the observable-space locations of stars. BH15, Z20, and Green et al. (2014) state this result without proof, but Walmswell et al. (2013) and Breimann et al. (2021, henceforth B21) prove it as a consequence of data generation via a Poissonian process that is inhomogeneous in observable space. The idea of thus multiplying probability density values at observable-space locations of stars to obtain the likelihood of cluster parameters was introduced earlier (Naylor & Jeffries, 2006; van Dyk et al., 2009). B21 evaluate the density values and, consequently, the likelihoods, over a range of cluster parameters. In B21's case, the latter are synonymous with stellar evolution parameters. These authors find that theoretical probability density values for some of the observed stars are very low, even at maximum-likelihood evolutionary parameters: these stars cannot be explained by the theoretical model. B21 conclude that the evolutionary model approximations should be modified. Unlike other authors mentioned so far in this section, B21 never evaluate or marginalize single-star posteriors over stellar parameter ranges to calculate the probability densities. Instead, they estimate the densities directly by binning stellar models in observable space.

Gossage et al. (2019, henceforth G19) also take a binning approach and estimate cluster parameters via comparisons of theoretical densities in color-magnitude space, a.k.a. Hess diagrams, with their observed counterparts (Dolphin, 2002). In G19's work,

the estimated parameters are the cluster's age, the Gaussian age spread, and the rotation rate distribution. The authors' evolutionary models are from `MIST`, like those in C20. Like B21, G19 do not evaluate single-star posteriors, directly comparing likelihoods of different cluster models. These authors state that their analysis does not conclusively distinguish between age and rotation in causing eMSTOs. However, they suggest that the distinction could be made via the inclusion of rotational data such as projected equatorial velocities. Furthermore, G19's detailed analysis allows them to identify the evolutionary processes that one can tune to improve the model's fit to the data and to independent knowledge of cluster structure and formation history. Specifically, the authors propose that the match to the data could improve with the tuning of the model's rotation-related processes, such as magnetic braking. Earlier work in the same vein indicates that other processes, such as rotationally induced mixing, also greatly affect the joint inference of age and rotational distributions (Gossage et al., 2018).

1.3.4 Our Analysis of NGC 1846

In Chapter 4, we follow G19's example and compare NGC 1846 data with the `MIST` rotating stellar model to jointly infer the rotational and age distributions of the cluster's MSTO stars. In line with G19's suggestion and similarly to BH15, our analysis integrates projected equatorial velocity measurements with multi-band photometry of the stars. Furthermore, much like G19, we identify evolutionary processes that one can tune to improve the fit between the model and the data. With this work, we intend to provide a

generally applicable and statistically quantifiable numerical framework for the derivation of the properties of star clusters based on known aspects of stellar evolution and the derivation of constraints on stellar evolution based on known properties of star clusters.

Chapter 2

Synthetic Spectra of Rotating Stars

In this chapter, we present the software `PARS` (Paint the Atmospheres of Rotating Stars). The main input to this computer program is specific intensity emitted by a plane-parallel atmosphere model. The model specifies intensity as a function of wavelength, viewing angle, surface gravity, and temperature. Based on this specification, `PARS` numerically integrates intensity over the centrifugally deformed surface of a rotating star, taking into account the temperature, gravity, viewing angle, and size of each visible surface patch. The result is a synthetic spectrum of the star. We demonstrate that `PARS` calculates such spectra with great speed and precision.

At the end of this chapter, we also introduce an extension of `PARS` that computes synthetic light curves of planetary transits for planets that orbit rotating stars, under arbitrary projected obliquity.

The contents of this chapter have been published in Lipatov & Brandt (2020b), under

the title "Synthetic Spectra of Rotating Stars".

2.1 Stellar model

We begin with our model for the structure of the star itself. A simple choice is a uniformly rotating Roche model, where the potential at the stellar surface is approximated by placing all of the star's mass at its center. However, two-dimensional models of material flows in rotating stars predict that the cores and equatorial regions of early-type stars have larger angular velocities than their envelopes and polar regions, respectively (Rieutord et al., 2016; Rieutord & Espinosa Lara, 2009). BD20 infer these effects from spectro-interferometry of a resolved star. In general, mass flows and differential rotation could result in profound consequences for the shapes and temperatures of stars (Kippenhahn, 1977; Zorec et al., 2011).

Nevertheless, a Roche model can account for much of the physics that underlies the spectrum of an early-type star. One such model incorporates collinearity of gravity and energy flux (Espinosa Lara & Rieutord, 2011, henceforth ER11). ER11 show that there is less than 0.01 radians of deviation from this collinearity in a two-dimensional model of material flow. Additionally, the linear dimensions of a polytrope that mimics the star's structure and those of a Roche model differ by about 1% (Orlov, 1961). Furthermore, stellar evolution calculations that form an input to our integration scheme do not model surface differential rotation due to their fundamentally one-dimensional nature. These calculations consider uniform rotation on isobars and use pressure as the radial coordinate

(again assuming collinearity of effective gravity and energy flux and uniform surface rotation) (Meynet & Maeder, 2000; Ekström et al., 2012; Georgy et al., 2014; Paxton et al., 2011, 2019). The calculations result in surface shapes and temperature profiles that agree with those of ER11's structural model. Fully two-dimensional stellar evolution models remain well beyond reach due to the enormous range of both time and length scales in the problem.

Due to the match between ER11's model and the output of stellar evolution calculations, its close agreement with fully two-dimensional structural models, and numerical convenience, we adopt ER11's model and note that it involves solid body rotation.

We can visualize energy transport through a rotating star by solving for the internal energy flux lines. Figure 2.1 shows these lines as computed numerically from ER11's equation 21. They are relatively far from each other in the equatorial regions of the surface, so that these regions are at relatively low temperatures due to the Stefan-Boltzmann law. At the star's center, where rotation is dynamically unimportant (under the assumption of solid body rotation), the flux lines are equally spaced and energy transport is independent of polar angle.

We define inclination $i \in [0, \pi/2]$ as the angle between the model's rotation axis $\hat{\mathbf{z}}$ and the line of sight $\hat{\mathbf{i}}$. The ER11 model is symmetric about its axis of rotation, though not necessarily about any line of sight. Accordingly, we primarily describe the stellar surface by a set of cylindrical coordinates z, r and ϕ defined by the stars's rotational symmetry and assign $\phi = 0$ to the azimuthal direction closest to $\hat{\mathbf{i}}$. We also use Cartesian

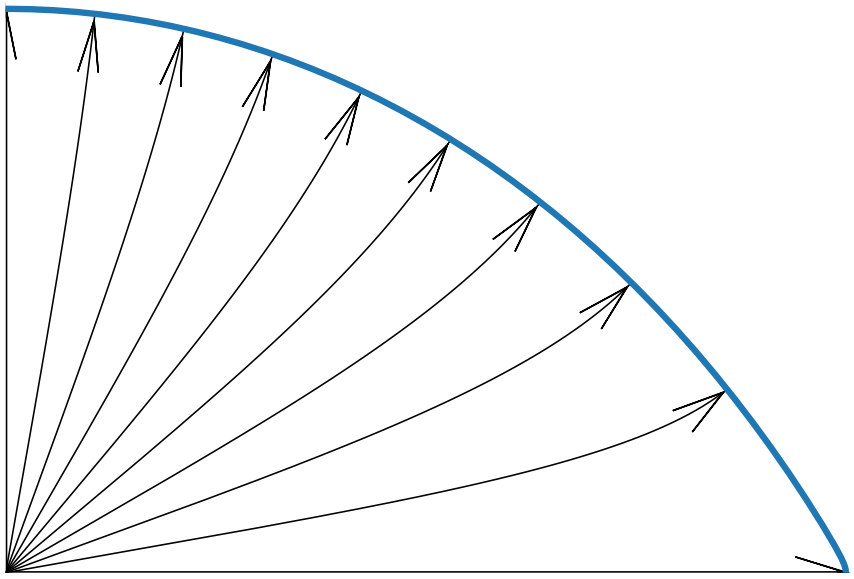

Figure 2.1 Meridional cut through the projected surface and internal energy flux lines of a star rotating at $\omega = 0.99$, from ER11's model. Only 1/4 of the star is shown, due to symmetry. At the center of the star, the flux lines are equally spaced. At the surface, however, they are farther apart near the equator than near the pole (the pole, as a result, is hotter).

coordinates that include $\hat{\mathbf{z}}$ and an x-axis coinciding with $\phi = 0$ at $z = 0$ (see Figure 2.2). We define R_p as the polar radius of the star and $\mu \in [0, 1]$ as cosine of the viewing angle, i.e. the angle between the line of sight and the normal to the surface.

Our goal is to compute the star's specific flux $\mathcal{F}_\nu$ along the line of sight. $\mathcal{F}_\nu$ is given by

$$D_\star^2 \, \mathcal{F}_\nu = 2 \int_{-z_b}^{R_p} A(z) \int_0^{\phi_b(z)} I_\nu(z, \phi) \, \mu(z, \phi) \, d\phi \, dz, \tag{2.1}$$

where $D_\star$ is the distance to the star and z_b corresponds to the lowest stellar latitude that is visible at all ϕ. For a differential element of the stellar surface, $A(z)\,\mu(z,\phi)\,d\phi\,dz$ is the element's area projected onto the view plane and $I_\nu(\phi, z)$ is its specific intensity per unit projected area. For all $z > -z_b$, at least some of the star is visible, while none of it is visible for $z < -z_b$. At a given z, the star is visible everywhere between $-\phi_b(z)$ and $\phi_b(z)$ and is not visible anywhere else. The factor of 2 arises due to the symmetries of the model, since the integral between 0 and $\phi_b(z)$ is equal to that between $-\phi_b(z)$ and 0. Another result of the symmetries is the fact that $\phi_b(z) = \pi$ for $z > z_b$.

2.2 Visible surface

2.2.1 Surface shape

We define $\tilde{r} \equiv r/R_e$, $\tilde{z} \equiv z/R_p$, and flatness $f \equiv R_e/R_p$, where R_e is the star's equatorial radius. Our definition of $\tilde{r}$ is different from that in ER11, which reserves this symbol for a normalized spherical coordinate. Note that $r'(z) = f\,\tilde{r}'(\tilde{z})$. By substituting the polar value of ER11's normalized spherical coordinate into their Equation (30), we find that

$$f = 1 + \omega^2/2, \tag{2.2}$$

where

$$\omega \equiv \Omega\sqrt{\frac{R_e^3}{GM}} = \frac{\Omega}{\Omega_k},$$

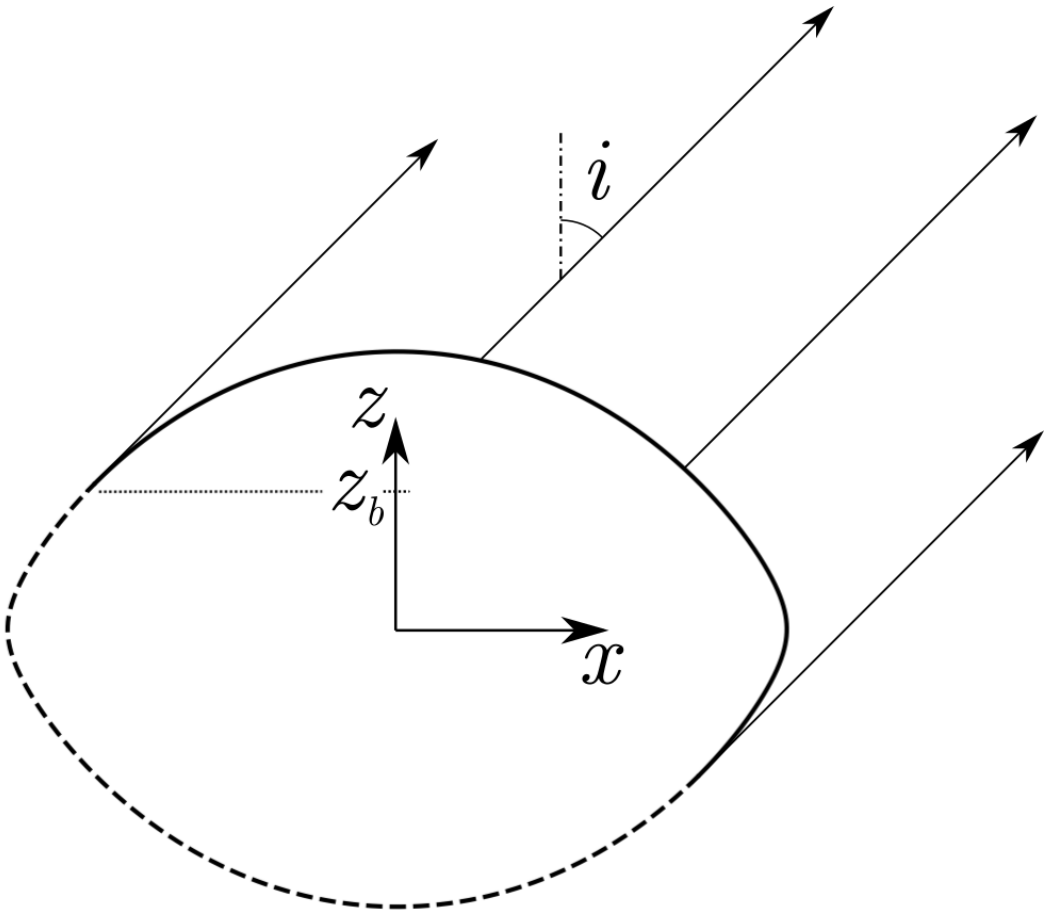

Figure 2.2 Meridional cut of the projected surface and observer sightlines for a star rotating at 90% of its Keplerian surface velocity with $i = \pi/4$ (see Section 2.1). The star is visible at all ϕ above $z = z_b$ and, by symmetry, at no ϕ below $z = -z_b$.

Ω is the star's angular velocity, Ω_k is the Keplerian velocity, M is the mass of the star, and G is the gravitational constant.

We define the following helper variables and constants:

$$w \equiv 1 + 2/\omega^2, \; u \equiv \tilde{z}/f = z/R_e \text{ and } s \equiv \tilde{r}^2. \tag{2.3}$$

In the remainder of this chapter, we will indicate point locations by either dimensional

coordinates such as z or by normalized dimensionless coordinates such as $\tilde{z}$ or u. Converting ER11's Equation (30) to normalized cylindrical coordinates and keeping in mind Equation (2.3), we obtain

$$\frac{1}{\omega^2\sqrt{\tilde{r}^2+u^2}}+\frac{\tilde{r}^2}{2}=\frac{1}{\omega^2}+\frac{1}{2}, \tag{2.4}$$

which leads to a cubic in s:

$$s^3+s^2\left(u^2-2w\right)+s\,w\left(w-2u^2\right)+\left(u^2-1\right)w^2+2w-1=0. \tag{2.5}$$

We solve this as a function of u to obtain

$$s(u)=\frac{1}{3}\left[\,-u^2+2w+2\left(u^2+w\right)v(u)\,\right]. \tag{2.6}$$

Here,

$$v(u)\equiv\cos\left[\frac{1}{3}\left(\cos^{-1}\left[\,t(u)\,\right]+2\pi\right)\right] \tag{2.7}$$

with

$$t(u)\equiv\frac{27\,(1-w)^2}{2\left(u^2+w\right)^3}-1. \tag{2.8}$$

We differentiate Equation (2.6) to obtain

$$s'(u) = \frac{2u}{3}\,\frac{1-2\,v(u)}{1+2\,v(u)}. \tag{2.9}$$

Equations (2.2)–(2.9), along with the definitions of f, $\tilde{r}$, and $\tilde{z}$, can be used to obtain $\tilde{r}(\tilde{z})$ and $\tilde{r}'(\tilde{z})$. Now consider

$$\mathbf{dl} \equiv \hat{\mathbf{r}}\,dr + \hat{\mathbf{z}}\,dz, \tag{2.10}$$

a differential element of $r(z)$ between z and $z + dz$. Its length dl can be found from the Pythagorean theorem and the definition of $r'(z)$:

$$dl = \sqrt{r'(z)^2 + 1}\,dz. \tag{2.11}$$

As we rotate **dl** around the star's symmetry axis by $d\phi$, the area of the resulting differential surface element is $r(z)\,dl\,d\phi$. We multiply this area by $\mu(z,\phi)$ to project it onto the view plane, substitute for dl according to Equation (2.11), and change variables from z and $r(z)$ to $\tilde{z}$ and $\tilde{r}(\tilde{z})$. This results in

$$A(z)\,\mu(z,\phi)\,dz\,d\phi = R_e^2\,\tilde{A}(\tilde{z})\,\mu(\tilde{z},\phi)\,d\tilde{z}\,d\phi \tag{2.12}$$

with

$$\tilde{A}(\tilde{z}) = \frac{\tilde{r}(\tilde{z})\, n(\tilde{z})}{f}, \tag{2.13}$$

where

$$n(\tilde{z}) = \sqrt{[f\, \tilde{r}'(\tilde{z})]^2 + 1}. \tag{2.14}$$

A change of variables from $\tilde{r}$ and $\tilde{z}$ to s and u implies

$$f\, \tilde{r}'(\tilde{z}) = \left. \frac{s'(u)}{2\sqrt{s(u)}} \right|_{u=\tilde{z}/f} \tag{2.15}$$

and

$$s'(u) = 2f\, \tilde{r}'(\tilde{z})\, \tilde{r}(\tilde{z})\, |_{\tilde{z}=fu}\, . \tag{2.16}$$

Equation (2.16) helps perform this change of variables in equations (2.13) and (2.14). The result is

$$\tilde{A}(\tilde{z}) = \left. \frac{1}{f} \sqrt{\frac{1}{4} s'(u)^2 + s(u)} \right|_{u=\tilde{z}/f} . \tag{2.17}$$

At the poles of the star, $\tilde{r}(\tilde{z}) \to 0$ and $\tilde{r}'(\tilde{z}) \to \mp\infty$ as $\tilde{z} \to \pm 1$. Thus, the right side of equation (2.13) multiplies zero by infinity in this limit, and we cannot use it to find

$\tilde{A}(\pm 1)$, which is finite. However, $s'(u)$ remains finite as $u \to \pm 1/f$. Accordingly, we use equation (2.17) for all computation.

We now re-write Equation (2.1) as

$$D_\star^2 \, \mathcal{F}_\nu = 2R_e^2 \int_{-\tilde{z}_b}^{1} \tilde{A}(\tilde{z}) \int_0^{\phi_b(\tilde{z})} \mu(\tilde{z}, \phi) \, I_\nu(\tilde{z}, \phi) \, d\phi \, d\tilde{z}, \tag{2.18}$$

where $\tilde{z}_b \equiv z_b / R_p$.

2.2.2 Viewing angle

Due to the star's cylindrical symmetry, a normal to its surface does not have a component in the $\hat{\phi}$ direction. Such a normal also has to be perpendicular to **dl** in Equation (2.10). The two directions that satisfy both conditions are along vectors $\mathbf{dn} = \pm(\hat{\mathbf{r}}\, dz - \hat{\mathbf{z}}\, dr)$. Here, the positive sign gives the vector with a non-negative $\hat{\mathbf{r}}$ component — the vector that points away from the star's interior. We divide it by dz to get $\hat{\mathbf{r}} - r'(z)\, \hat{\mathbf{z}}$, make the same change of variables as in Equation (2.12), and normalize the result, which yields

$$\hat{\mathbf{n}} = \frac{\hat{\mathbf{r}} - f \, \tilde{r}'(\tilde{z}) \, \hat{\mathbf{z}}}{n(\tilde{z})}. \tag{2.19}$$

To convert this expression to the Cartesian coordinates, we replace $\hat{\mathbf{r}}$ with $\cos\phi \; \hat{\mathbf{x}} + \sin\phi \; \hat{\mathbf{y}}$:

$$\hat{\mathbf{n}} = \frac{\cos\phi \; \hat{\mathbf{x}} + \sin\phi \; \hat{\mathbf{y}} - f \, \tilde{r}'(\tilde{z}) \, \hat{\mathbf{z}}}{n(\tilde{z})}. \tag{2.20}$$

The normalized line-of-sight vector is

$$\hat{\mathbf{i}} = \sin i \ \hat{\mathbf{x}} + \cos i \ \hat{\mathbf{z}}, \tag{2.21}$$

so that the cosine of the angle between the two vectors is

$$\hat{\mathbf{n}} \cdot \hat{\mathbf{i}} \equiv \mu(\tilde{z}, \phi) = \frac{\sin i \ \cos\phi - \cos i \ [f \, \tilde{r}'(\tilde{z})]}{n(\tilde{z})}. \tag{2.22}$$

2.2.3 Visibility Boundaries

Setting Equation (2.22) to zero at $\phi = \pi$, we obtain a condition for $\tilde{z} = \tilde{z}_b$ (see Section 2.1 and Figure 2.2):

$$f \, \tilde{r}'(\tilde{z}_b) = -\tan i. \tag{2.23}$$

Combining Equations (2.23) and (2.15) and squaring the result, we obtain

$$\imath \equiv (\tan i)^2 = \frac{s'(u_b)^2}{4 \, s(u_b)}, \tag{2.24}$$

where $u_b \equiv \tilde{z}_b / f$. We solve Equation (2.6) for $v(u)$ in terms of $s(u)$ and substitute the result into Equation (2.9), thus obtaining $s'(u)$ in terms of $s(u)$. This, in turn, is substituted into equation (2.24), which results in

$$9s^3\imath - s^2\left[12u^2\imath - u^2 - 6\imath w\right] + s\left[\left(2u^2 - w\right)^2\imath + 2u^2w^2\right] - u^2w^2 = 0, \tag{2.25}$$

where, for compactness, u_b is written as u and $s(u_b)$ as s. We can solve Equation (2.5) for u^2 in terms of $s(u)$ and substitute the result into Equation (2.25) to obtain a 7th-order polynomial equation in $s(u_b)$, which can be solved numerically. Equation (2.5) can then be used again to obtain u_b^2, u_b and $\tilde{z}_b$.

As discussed in Section 2.1, the surface is visible at a subset of ϕ for $\tilde{z} \in (-\tilde{z}_b, \tilde{z}_b)$. At every $\tilde{z}$ in this region, there is some ϕ_b for which $\mu = 0$. Accordingly, to find these boundary values, we substitute $\phi = \phi_b$ into Equation (2.22), obtaining

$$\phi_b(\tilde{z}) = \arccos\left[\, f\,\tilde{r}'(\tilde{z})\,\cot i\,\right]. \tag{2.26}$$

2.3 Azimuthal integral

2.3.1 Intensity functions

Castelli & Kurucz (2004), henceforth CK04, provide specific intensities I_ν on a discrete grid of microturbulent velocity ξ, metallicity [M/H], effective surface temperature T, effective surface gravity g, radiation wavelength λ, and cosine of the viewing angle μ. The unit of I_ν is $\mathrm{erg\,s^{-1}\,Hz^{-1}\,ster^{-1}\,cm^{-2}}$; fixed sets of 1221 λ values and 17 μ values constitute the grid's extent in the corresponding dimensions at all points. Hereafter,

effective surface gravity and effective surface temperature are sometimes simply gravity and temperature.

We define a set of closed intervals $\{m_j\}$ that form a partition of μ's range, with each interval boundary point among the constant μ grid values in CK04's data. With $m_j \equiv [\mu_j, \mu_{j+1}]$, $\mu_{j_1} < \mu_{j_2}$ when $j_1 < j_2$.

In the remainder of this work, we set the partition to $[0, 0.1]$, $[0.1, 0.4]$, and $[0.4, 1]$; we also set [M/H] to -0.1 and ξ to $2\,\mathrm{km\,s^{-1}}$. Let us say that CK04 provide intensity I_1 at $\mu = 1$, as well as intensity values at other discrete μ, all for a specific parameter space location (T, g, λ). We model $I_\nu(\mu)$ at this location as a piecewise polynomial

$$I_\nu(\mu) = \sum_{i=0}^{4} a_{ik}\mu^i \quad \text{with } \; k = \max_{\mu \in m_j} j. \tag{2.27}$$

For each j, we obtain the coefficients a_{ij} $\forall i$ by a least-squares fit to CK04's points on m_j, using every boundary point on each of the two intervals it belongs to. Here and elsewhere in this chapter, we use version 3 of the Python programming language and the NumPy library (van der Walt et al., 2011) for all calculations.

For every (T, g, λ), we conduct the above fitting procedure and calculate the associated error in $I_\nu(\mu)$ at every μ grid point:

$$\left|\frac{\delta I_\nu}{I_1}\right| \equiv \left|\frac{I_\nu(\mu) - I_\mu}{I_1}\right|. \tag{2.28}$$

Here, I_μ is CK04's value of I_ν at the grid point, $I_\nu(\mu)$ is given by equation (2.27), and

the error is normalized by I_1.

The global error maximum and the median of the error maxima across the (T, g, λ) space are 0.17% and 0.010%, respectively. Figure 2.3 presents both the errors and the intensity fits for the location of the global maximum and for one of the locations with maximum error closest to the median. Left to right, the three partition intervals respectively contain 5, 7 and 7 grid points. Thus, the 4th degree polynomial fit is slightly over-constrained on each of the latter two intervals, so that their errors in Figure 2.3 give us a sense of the true error associated with the procedure. On the other hand, the lowest interval's number of grid points equals the number of the polynomial's parameters, so that its error is due to round-off.

The lowest $I_\nu(\mu)$ / I_1 and $I'_\nu(\mu)$ / I_1 across all the fits are -0.95% and -2.65, respectively. Negative values for both quantities are not physical, though they are also rare. We do not expect them to affect the accuracy of our results any more significantly than the errors we estimate via the fitting procedure.

The least-squares fits over the entire parameter space take about 50 seconds on a 2.3 GHz MacBook Pro with 8 GB of RAM. In the remainder of this chapter, the distinction between i as either an integer-valued index or the inclination should be clear from context.

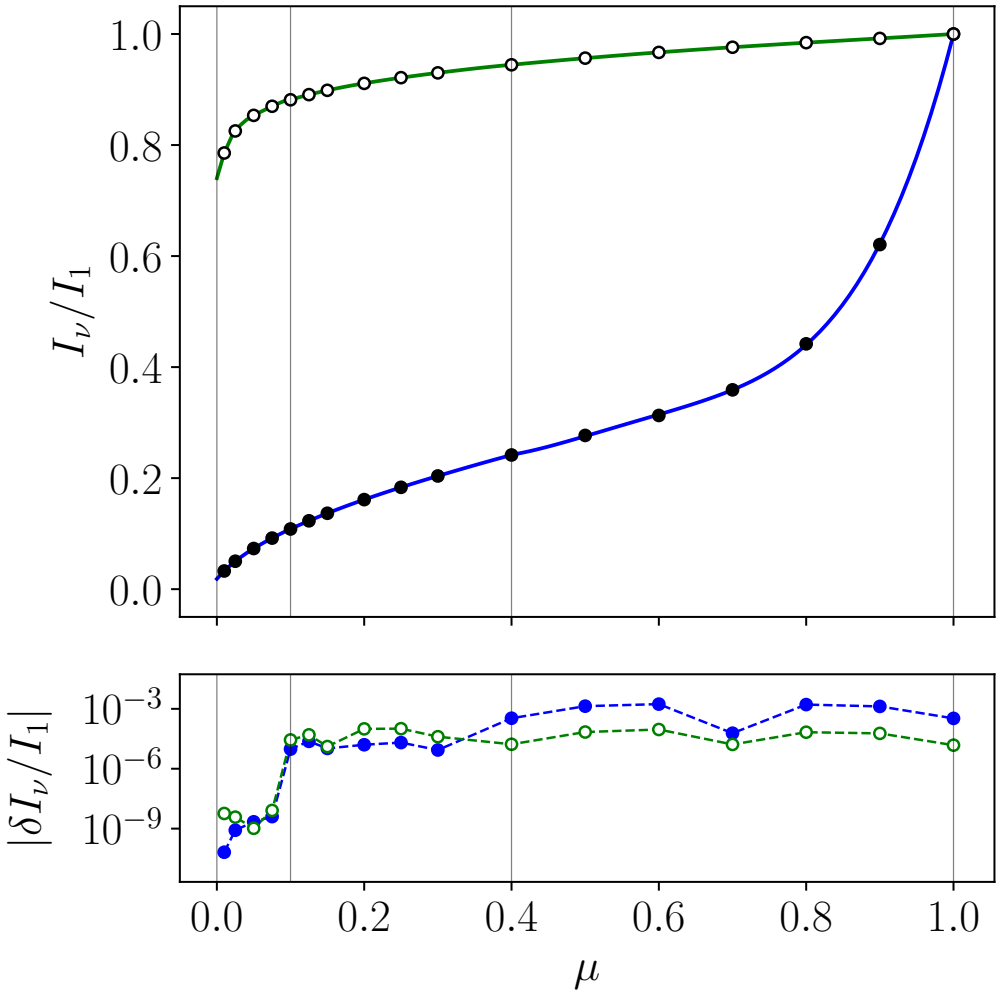

Figure 2.3 Top panel: circles indicate normalized intensity values in CK04 on a grid of μ, lines — the piecewise polynomial fits $I_\nu(\mu)$ to these points. Bottom panel: relative error in I_ν at the grid points (see Section 2.3.1). Both panels: blue lines and solid markers correspond to the location of maximum error in parameter space: $T = 9000\,\mathrm{K}$, $\log_{10} g = 3.0$, and $\lambda = 111.5\,\mathrm{nm}$; green lines and open markers — a location of an error closest to median: $T = 7750\,\mathrm{K}$, $\log_{10} g = 1.5$, and $\lambda = 5070\,\mathrm{nm}$; grey vertical lines mark the boundaries of the partition.

2.3.2 Piecewise integration

In the foregoing, $i \in \{0, \ldots, 4\}$ and $j \in \{1, 2, 3\}$. We define functions

$$p_{ij}(\tilde{z}, \phi) \equiv \begin{cases} \mu(\tilde{z}, \phi)^i & \mu(\tilde{z}, \phi) \in m_j \\ 0 & \text{otherwise} \end{cases}. \tag{2.29}$$

Here, $\mu(\tilde{z}, \phi)$ is given by Equation (2.22). We re-write Equation (2.27) as

$$I_\nu(\tilde{z}, \phi) = \sum_{i,j} a_{ij}(\tilde{z})\ p_{ij}(\tilde{z}, \phi), \tag{2.30}$$

where the a_{ij} depend on $\tilde{z}$ because T and g depend on $\tilde{z}$ (see Sections 2.3.1 and 2.3.3). We substitute Equation (2.30) into Equation (2.18) and move both the sum and the fit coefficients outside the integral in ϕ. This results in

$$D_\star^2\, \mathcal{F}_\nu = 2R_e^2 \int_{-\tilde{z}_b}^{1} \tilde{A}(\tilde{z}) \sum_{i,j} a_{ij}(\tilde{z}) \times \int_0^{\phi_b(\tilde{z})} \mu(\tilde{z}, \phi)\, p_{ij}(\tilde{z}, \phi)\, d\phi\, d\tilde{z}. \tag{2.31}$$

We define

$$P_{ij}(\tilde{z}) \equiv \int_0^{\phi_b(\tilde{z})} \mu(\tilde{z}, \phi)\, p_{ij}(\tilde{z}, \phi)\, d\phi. \tag{2.32}$$

According to equation (2.29), every p_{ij} is zero outside m_j and its dependence on ϕ is polynomial in $\cos\phi$ within m_j. Due to this choice of $\{p_{ij}\}$, we can analytically express the indefinite version of each integral in equation (2.32) in terms of cosines and sines.

Calculation of the definite integrals involves the algorithm in Appendix A, which keeps track of m_j in the course of integration and accounts for the fact that $\mu(\tilde{z}, \phi)$ in equation (2.22) decreases as ϕ increases. Expression of the indefinite integrals in terms of cosines and sines permits quick calculation of $\{P_{ij}\}$. Such calculation may not be possible for a form of I_ν that differs from equations (2.27)–(2.30). For example, a number of authors use forms with $\mu^{1/2}$ (Claret, 2000, 2018, BD20), which can be emulated with $i = 1/2$ in some of the $\{p_{ij}\}$. Expressions for the corresponding $\{P_{ij}\}$ involve incomplete elliptic integrals, which are relatively slow to evaluate.

Together, Equations (2.31) and (2.32) yield

$$D_\star^2 \mathcal{F}_\nu = 2R_e^2 \int_{-\tilde{z}_b}^{1} \tilde{A}(\tilde{z}) \sum_{i,j} a_{ij}(\tilde{z})\, P_{ij}(\tilde{z})\, d\tilde{z}. \tag{2.33}$$

2.3.3 Temperature and gravity calculation

We add spherical coordinates θ and ρ to our description of the stellar surface. These satisfy

$$\rho = \sqrt{r^2 + z^2} \;\text{ and }\; \sin\theta = r/\rho. \tag{2.34}$$

We further define $\tilde{\rho} \equiv \rho/R_e$, so that

$$\tilde{\rho} = \sqrt{\tilde{r}^2 + \tilde{z}^2/f^2} \;\text{ and }\; \sin\theta = \tilde{r}/\tilde{\rho}. \tag{2.35}$$

Combined with ER11's Equation (31), this gives us the following expression for gravity:

$$g(\tilde{z}) = \frac{GM}{R_e^2}\sqrt{\frac{1}{\tilde{\rho}^4} + \omega^2\tilde{r}^2\left(\omega^2 - \frac{2}{\tilde{\rho}^3}\right)}, \tag{2.36}$$

where $\tilde{r}(\tilde{z})$ is found in Section 2.2 and $\tilde{\rho}(\tilde{z})$ can be obtained from Equation (2.35). According to ER11's equations 31 and 26, temperature is then

$$T(\tilde{z}) = \left[\frac{L}{4\pi\sigma GM}\, F(\tilde{z})\, g(\tilde{z})\right]^{1/4}, \tag{2.37}$$

where L is the luminosity of the star, σ is Stefan's constant and

$$F = \left(\frac{\tan\vartheta}{\tan\theta}\right)^2 \tag{2.38}$$

with

$$\cos\vartheta + \ln\tan\frac{\vartheta}{2} = \frac{1}{3}\omega^2\tilde{\rho}^3\cos^3\theta + \cos\theta + \ln\tan\frac{\theta}{2}. \tag{2.39}$$

ER11 tells us that the range of F for a given ω is $[F_1, F_0]$, where

$$F_0 \equiv F(0) = \left[1 - \omega^2\,\tilde{\rho}\,(0)^3\right]^{-2/3} = \left(1 - \omega^2\right)^{-2/3} \tag{2.40}$$

and

$$F_1 \equiv F\left(1\right) = e^{\frac{2}{3}\omega^2 \tilde{\rho}(1)^3} = e^{\frac{2}{3}\omega^2 f^{-3}} \tag{2.41}$$

with F and $\tilde{\rho}$ seen as functions of $\tilde{z}$, $\tilde{\rho}\left(0\right) = 1$ and $\tilde{\rho}\left(1\right) = 1/f$. Note that $F_0 \geq F_1 \geq 1$. In order to obtain F from Equations (2.38) and (2.39), we define a new variable, $x \equiv \cos\theta \in [0, 1]$ and perform a change of variables from $\{\vartheta, \theta\}$ to $\{F, x\}$ in these equations. This results in

$$h(F; x, \omega) = 0, \tag{2.42}$$

where

$$h(F; x, \omega) \equiv \frac{x}{G} + \ln\left(\frac{(1+x)\sqrt{F}}{x+G}\right) - x - \frac{1}{3}\omega^2\tilde{\rho}^3 x^3 \tag{2.43}$$

with

$$G \equiv G(F; x) \equiv \sqrt{x^2 + F\left(1 - x^2\right)}. \tag{2.44}$$

Thus, given x, we can treat $\tilde{\rho}$ as a function of x and find F by solving Equation (2.42) with F as the independent variable. We do so using a variant of Newton's method, which

requires

$$\frac{\partial h}{\partial F} = \frac{1}{2F}\left(\frac{x}{G}\right)^3. \tag{2.45}$$

We start half-way between F_1 and F_0 and add

$$\Delta F\left(F; x, \omega\right) = -\frac{h}{\partial h/\partial F} = 2FG^2\left[g_1 + g_2 + g_3\right] \tag{2.46}$$

to our estimate of F at each iteration, until ΔF is close to zero. Here,

$$g_1 \equiv g_1(F; x) \equiv \frac{G-1}{x^2}, \tag{2.47}$$

$$g_2 \equiv g_2(F; x) \equiv -\frac{G}{x^3}\ln\frac{(1+x)\sqrt{F}}{x+G}, \tag{2.48}$$

and

$$g_3 \equiv g_3(F; x, \omega) \equiv \frac{1}{3}\omega^2\tilde{\rho}^3 G. \tag{2.49}$$

A series expansion of each additive term in Equation (2.46) in x around $x = 0$ shows that the equation's last term is $\mathcal{O}(1)$ and that its first two terms are

$$2FG^2 g_1 \approx 2\frac{F^{5/2} - F^2}{x^2} + \mathcal{O}\left(1\right) \tag{2.50}$$

and

$$2FG^2g_2 \approx -2\frac{F^{5/2} - F^2}{x^2} + \mathcal{O}(1). \tag{2.51}$$

Consider what happens for $x \to 0$. As F approaches the root of h in the course of running the algorithm, $\Delta F \to 0$, so that the increasingly large terms in Equations (2.47) and (2.48) must cancel each other. Indeed, as implied by Equations (2.46), (2.50), and (2.51), a series expansion of Equation (2.46) in x around $x = 0$ doesn't have such terms:

$$\Delta F \approx \frac{2}{3}\left[F - F^{5/2}\left(1-\omega^2\right)\right] + x^2\left[\frac{2}{5} - F^{3/2}\left(1-\omega^2\right) + F^{5/2}\frac{3-8\omega^2}{5\left(1-\omega^2\right)}\right] + \mathcal{O}(x^4). \tag{2.52}$$

The coefficient of the x^4 term in this expansion is

$$\alpha_4(F;\omega) = \frac{1}{140}\left[56 - \frac{16}{F} - 35\sqrt{F}\left(1-\omega^2\right) - 14\,F^{3/2}\,\frac{1+4\,\omega^2+10\,\omega^4}{1-\omega^2} + F^{5/2}\,\frac{9+8\,\omega^2+44\,\omega^4\,(3-\omega^2)}{\left(1-\omega^2\right)^3}\right]. \tag{2.53}$$

Under constant machine epsilon q, decreasing x increases the absolute error in ΔF (and thus in F) associated with the increasingly large additive terms in Equation (2.46). At the same time, the error associated with Equation (2.52) decreases, since the series expansion becomes a better approximation of ΔF. We seek to approximate ΔF using the better of Equations (2.46) and (2.52), setting the boundary between the methods at the point

where their respective errors are equal.

Given Equations (2.50) and (2.51), the rounding error due to Equation (2.46) is

$$\varepsilon_A = 2\frac{q}{A}\frac{F^{5/2} - F^2}{x^2}. \tag{2.54}$$

where $A \geq 1$ and q is machine epsilon, $\sim 2\times10^{-16}$ in double precision. We also approximate the error associated with using Equation (2.52) as

$$\varepsilon_B = B\alpha_4 x^4, \tag{2.55}$$

where $B \sim 1$. We then equate Equations (2.54) and (2.55), approximate F with F_0, define $k \equiv AB$, and solve for x:

$$x = \left(\frac{2q}{k}\,\frac{F_0^{5/2} - F_0^2}{\alpha_4(F_0)}\right)^{1/6}. \tag{2.56}$$

We cast the right-hand side of Equation (2.56) as a function of ω with the help of Equations (2.40) and (2.53). As ω approaches 0, the computation of this expression becomes impossible due to rounding error. Accordingly, we sum the first three terms of its series expansion around $\omega = 0$ to obtain x_b, a boundary value of x:

$$x_b(\omega) = q^{1/6}\left(\frac{2}{6885k}\right)^{1/6}\left[3\,\omega^{-2/3} - \frac{199}{255}\,\omega^{4/3} - \frac{29123}{65025}\,\omega^{10/3}\right]. \tag{2.57}$$

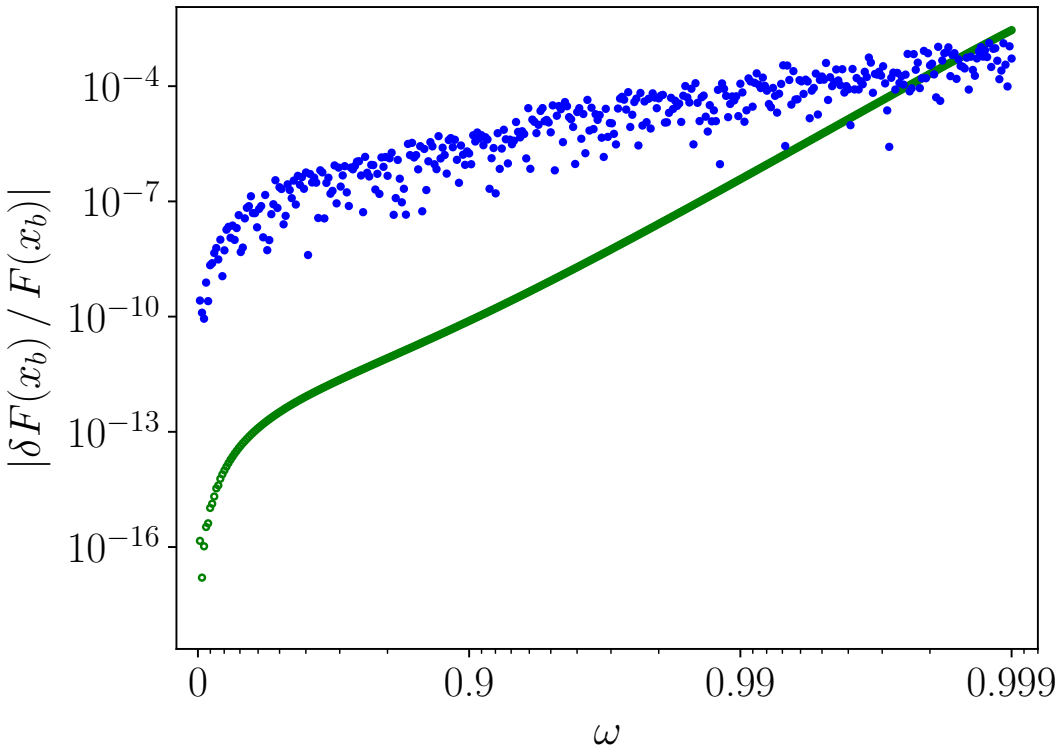

Figure 2.4 Relative error in F at x_b for floating point resolution $q = 2 \times 10^{-16}$, $\omega \in [0, 0.999]$ and parameter $k = 100$ (see Section 2.3.3). Blue filled and green open markers correspond to the use of Equation (2.46) and (2.52), respectively.

As ω decreases even further, Equation (2.57) exceeds 1, the upper bound of x's range. For these values of ω, we set x_b to 1.

To estimate the actual error in F, we use equation (2.46) to calculate its etalon values with `mpmath` (Johansson et al., 2018) and $q \sim 10^{-100}$. In the rest of our calculations, we use equation (2.52) up to the second order in x whenever $x \leq x_b$ and equation (2.46) otherwise, with $q = 2 \times 10^{-16}$ throughout. If $\omega \in [0, 0.999]$, the resulting relative error in F at x_b tends to its maximum value at $\omega = 0.999$. We set k to 100, where this maximum error is close to minimized, equal to 0.3% (see Figure 2.4). According to equation (2.37), this corresponds to a lower relative error in T.

For large enough values of ω in its range, an iteration of both an error-free Newton's method and our error-prone algorithm can result in $F < F_1$. In such cases, we set F to F_1. Additionally, we set F to F_0 if $F > F_0$ in the course of running the error-prone algorithm, which can happen at low ω.

The algorithm converges within approximately 5, 6, 8, and 10 iterations for $\omega \leq 0.9$, $\omega = 0.95$, $\omega = 0.99$, and $\omega = 0.999$, respectively. In this chapter's work, we run it with 15 iterations, which takes no more than 0.1% of the total computing time for a 1221-wavelength spectrum.

2.3.4 Coefficient interpolation

We now define the temperature-dependent Planck factor as

$$\mathcal{P}(T) \equiv \left(\exp\left[\frac{hc}{\lambda k_B T} \right] - 1 \right)^{-1}, \tag{2.58}$$

where h is Planck's constant, c is the speed of light in vacuum, and k_B is Boltzmann's constant.

In Section 2.3.1 we obtain coefficients a_{ij} on a discrete grid of g and T. However, the values of g and T we get via Equations (2.36) and (2.37) are not necessarily on that grid. To obtain the a_{ij} that enter Equation (2.33), we interpolate each coefficient linearly in either g or $\log g$ and in either T, $\log T$, or $\mathcal{P}(T)$.

In order to assess the accuracy of interpolation, we aim to compute fractional errors in intensity for three fiducial nonrotating stars with $T = 6000$, 9000, and 12000 K, all

with $g = 10^{4.5}\mathrm{cm/s^2}$. Our choices of g and T are on the grid in CK04, so that we can first compute the stars' spectra without interpolation error. We also compute the stars' spectra with intensity information missing, either at their values of T or at their values of g, interpolating between the closest neighboring values where such information is available. The neighboring temperature pairs are $\{5750, 6250\}$, $\{8750, 9250\}$, and $\{11500, 12500\}$ K for the above-listed three stars, respectively. The neighboring gravity values are $10^{4.0}$ and $10^{5.0}$ cm/s^2. Figure 2.5 demonstrates the relative error we infer from the comparison of error-free spectra and spectra that involve interpolation. For the most part, $\mathcal{P}(T)$ and $\log g$ are the best interpolants, although others can be better at some λ and T. The $\log g$ and T differences between known points in the above accuracy assessments are twice their normal values, so that our assessments over-estimate interpolation error (by a factor $\sim$4 assuming that linear and quadratic terms dominate the local series expansions).

2.4 Longitudinal integral

2.4.1 Numerical schemes

In order to approximate the integral in Equation (2.33), we first evaluate its integrand,

$$f(\tilde{z}) \equiv 2R_{eq}^2\, \tilde{A}(\tilde{z}) \sum_{j,k} a_{jk}(\tilde{z})\, P_{jk}(\tilde{z}), \tag{2.59}$$

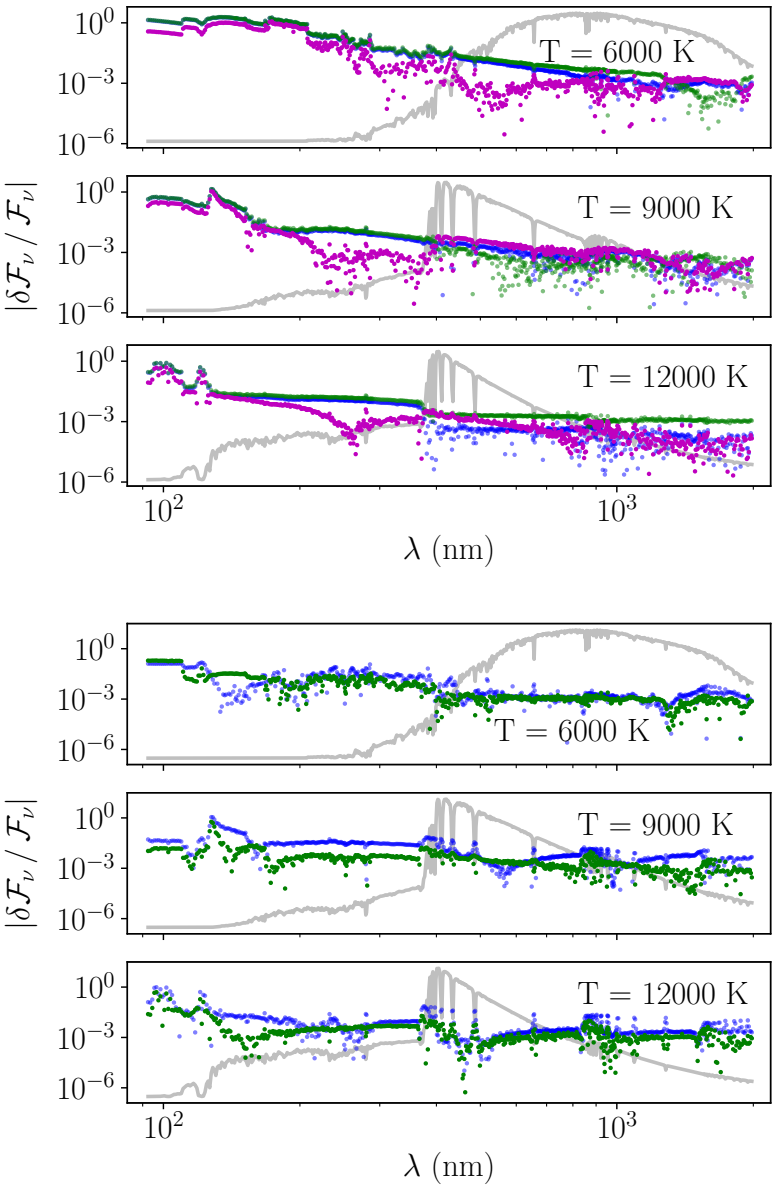

Figure 2.5 Relative flux errors due to interpolation in temperature (top three panels) and gravity (bottom three panels) for three nonrotating stars with $\log_{10} g = 4.5$ (cgs) and $T = 6000$, 9000, and 12000 K. Blue markers indicate interpolation in T and g, green — in $\log T$ and $\log g$, magenta — in $\mathcal{P}(T)$ (see Equation (2.58)). Grey lines show the stellar spectra on linear (not logarithmic) vertical scales. Errors are typically $\lesssim$1%, often much lower, in the spectral regions responsible for a significant fraction of the stellar flux. We compute these errors by omitting and interpolating over a tabulated model, artificially making them twice as far away from grid points as they would otherwise be. Real interpolation errors will be substantially lower.

at a set of $\mathcal{N} + \mathcal{N}_l - 1$ equally spaced discrete values $\{\tilde{z}_i\}$. Here, $i \in \{-\mathcal{N}_l + 1, -\mathcal{N}_l + 2, \ldots, 0, \ldots, \mathcal{N} - 2, \mathcal{N} - 1\}$, $\tilde{z}_{\mathcal{N}-1} = 1$, and $\tilde{z}_i < \tilde{z}_j$ when $i < j$. We ensure that $\tilde{z}_0 = 0$ and define $\Delta\tilde{z} \equiv \tilde{z}_1 - \tilde{z}_0$. Furthermore, we define $\delta\tilde{z} \equiv \tilde{z}_{-\mathcal{N}_l+1} - (-\tilde{z}_b)$ and note that $\mathcal{N}_l$ is a function of $\mathcal{N}$, as it satisfies $-\tilde{z}_b \leq \tilde{z}_{-\mathcal{N}_l+1} < -\tilde{z}_b + \Delta\tilde{z}$. The evaluation of $f_i \equiv f(\tilde{z}_i)$ for a given i is described in Sections 2.2 and 2.3. It is possible that $-\tilde{z}_b \neq \tilde{z}_i$ for all i, so that we do not evaluate $f(-\tilde{z}_b)$ directly. At the same time, $\mu = 0$ at $\tilde{z} = -\tilde{z}_b$, so that $P_{ij}(-\tilde{z}_b) = 0$ for all $\{i, j\}$ (see equations (2.29) and (2.32)). Thus, $f(-\tilde{z}_b) = 0$.

We wish to construct a numerical integration scheme that approximates $f(\tilde{z})$ as a piecewise polynomial of up to third order. If we had an analytic expression for the integrand, we might have been able to predict the performance of a possible scheme by evaluating the integrand's derivatives. Since we do not have such an expression, we start by examining the integrand at many discrete values of $\tilde{z}$ for a number of different stars. The integrand looks amenable to numerical integration almost everywhere. The exception is a downward cusp at $\tilde{z} = 0$ when $\omega \to 1$. This cusp is partly due to the fact that

$$\lim_{\substack{\omega \to 1 \\ \tilde{z} \to 0^{\pm}}} \tilde{r}'(\tilde{z}) = \mp \frac{1}{f\sqrt{3}}, \tag{2.60}$$

which results from equations (2.9) and (2.15), evaluated at the given limits. Here, f is a constant, defined in Section 2.2.1. This discontinuity in $\tilde{r}'$ leads to discontinuities in both $\{P_{ij}\}$ and $\tilde{A}$ (see equations (2.32), (2.29), (2.13), (2.14), and (2.22)), and thus contributes to the cusp in $f(\tilde{z})$. There is another contributing factor. When $\omega \to 1$, both

T and g approach zero at the equator and increase quickly away from zero latitude (see equations (2.36) and (2.37)). This causes $\{a_{ij}\}$ to also change rapidly with latitude in the equatorial regions under these conditions (see Section 2.3.1).

Thus, when ω approaches 1, the shape of the star and its effective gravity profile near $\tilde{z} = 0$ jointly lead to a cusp in the integrand. In view of this fact, we split the integral into two parts. We use $\{f_i\}$ with $i \in \{-\mathcal{N}_l + 1, \ldots, 0\}$ and with $i \in \{0, \ldots, \mathcal{N} - 1\}$ to approximate the integral on the lower interval $[-\tilde{z}_b, 0]$ and on the upper interval $[0, 1]$, respectively. To calculate the integral on the upper interval $\mathcal{I}_u$, we make use of an approximation based on the fitting of cubic polynomials through successive groups of four points (equation 4.1.14 in Press et al., 2007):

$$\mathcal{I}_u \equiv \int_0^1 f(\tilde{z})\, d\tilde{z} = \Delta\tilde{z} \left[\frac{3}{8} f_0 + \frac{7}{6} f_1 + \frac{23}{24} f_2 + f_3 + \right. \\ \left. \ldots + f_{\mathcal{N}-4} + \frac{23}{24} f_{\mathcal{N}-3} + \frac{7}{6} f_{\mathcal{N}-2} + \frac{3}{8} f_{\mathcal{N}-1} \right] + \varepsilon_u(\mathcal{N}), \quad (2.61)$$

where $\varepsilon_u(\mathcal{N})$ is the upper-interval error term.

When $\mathcal{N}_l \geq 2$ and $\delta\tilde{z} \neq 0$, we calculate the quadratic polynomial that goes through points $\{(-\tilde{z}_b, 0), (\tilde{z}_{-\mathcal{N}_l+1}, f_{-\mathcal{N}_l+1}), (\tilde{z}_{-\mathcal{N}_l+2}, f_{-\mathcal{N}_l+2})\}$ and shift it horizontally to go through $(0, 0)$, so that its form becomes $a\tilde{z}^2 + b\tilde{z}$.

When both the inclination and $\mathcal{N}$ are small, it is possible that $\mathcal{N}_l = 1 \vee (\mathcal{N}_l = 2 \wedge \delta\tilde{z} = 0)$. In this case, we approximate the integrand by a straight line between $(-\tilde{z}_b, 0)$ and $(0, f_0)$,

so that the integral on the lower interval $\mathcal{I}_l$ is

$$\mathcal{I}_l \equiv \int_{-\tilde{z}_b}^{0} f(\tilde{z})\, d\tilde{z} = \frac{1}{2}\,\delta\tilde{z}\, f_0 + \varepsilon_l(\mathcal{N}), \tag{2.62}$$

where $\varepsilon_l(\mathcal{N})$ is the lower-interval error term.

When $\mathcal{N}_l = 2$ and $\delta\tilde{z} \neq 0$, we approximate $\mathcal{I}_l$ by the integral of the above-mentioned quadratic on $[0, \tilde{z}_b]$:

$$\mathcal{I}_l = \frac{1}{3}\, a\, \tilde{z}_b^3 + \frac{1}{2}\, b\, \tilde{z}_b^2 + \varepsilon_l(\mathcal{N}). \tag{2.63}$$

When $\mathcal{N}_l \geq 3$, we use the quadratic to approximate the integral up to the lowest $\tilde{z}_i$:

$$\int_{-\tilde{z}_b}^{\tilde{z}_{-\mathcal{N}_l+1}} f(\tilde{z})\, d\tilde{z} \approx \delta\mathcal{I} \equiv \frac{1}{3}\, a\, (\delta\tilde{z})^3 + \frac{1}{2}\, b\, (\delta\tilde{z})^2. \tag{2.64}$$

For $\mathcal{N}_l = 3$, 4 and 5, we approximate the rest of $\mathcal{I}_l$ by Simpson's rule, Simpson's 3/8 rule and Boole's rule, respectively (see Section 4.1.1 of Press et al., 2007). For example, when $\mathcal{N}_l = 5$,

$$\mathcal{I}_l = \frac{\Delta\tilde{z}}{45}\left[14f_{-4} + 64f_{-3} + 24f_{-2} + 64f_{-1} + 14f_0\right] + \delta\mathcal{I} + \varepsilon_l(\mathcal{N}). \tag{2.65}$$

When $\mathcal{N}_l \geq 6$, we combine equation (2.64) with the approximation in equation (2.61):

$$\mathcal{I}_l = \Delta\tilde{z} \times \left[\frac{3}{8}f_{-\mathcal{N}_l+1} + \frac{7}{6}f_{-\mathcal{N}_l+2} + \frac{23}{24}f_{-\mathcal{N}_l+3} + f_{-\mathcal{N}_l+4} + \right. \\ \left. \ldots + f_{-3} + \frac{23}{24}f_{-2} + \frac{7}{6}f_{-1} + \frac{3}{8}f_0\right] + \delta\mathcal{I} + \varepsilon_l(\mathcal{N}). \quad (2.66)$$

The error terms, $\varepsilon_u(\mathcal{N})$ and $\varepsilon_l(\mathcal{N})$, can both be seen as functions of $\mathcal{N}$ for a given star. The integration scheme corresponding to equations (2.61)–(2.66) involves approximating the integrand by cubic polynomials everywhere except for the small interval in equation (2.64) and the entire lower interval when $\mathcal{N}_l \leq 3$. In the foregoing, we designate this scheme as cubic.

An alternate integration scheme is an application of the trapezoidal rule to separately calculate $\mathcal{I}_u$ and $\mathcal{I}_l$, whilst setting the integral in equation (2.64) to zero. We designate this scheme as trapezoidal. In either scheme, the flux is calculated according to

$$D_\star^2\,\mathcal{F}_\nu = \mathcal{I}_u + \mathcal{I}_l, \quad (2.67)$$

where the unknown error terms on the right-hand side are set to zero.

2.4.2 Convergence

To assess the convergence properties of the two schemes, we synthesize a star with Vega's M, L, R_e and ω from YP10. When the synthetic star is seen at $i = \pi/4$, $\lambda = 511$ nm is close to its spectral peak. We compute $\mathcal{F}_\nu(\mathcal{N})$, the flux for this combination of i and λ

at different $\mathcal{N}$ and plot

$$\left|\frac{\delta\mathcal{F}_\nu}{\mathcal{F}_\nu}\right| \equiv \frac{|\mathcal{F}_\nu(\mathcal{N}) - \mathcal{F}_\nu(10,000)|}{\mathcal{F}_\nu(10,000)} \tag{2.68}$$

in Figure 2.6. The trapezoidal approximation converges according to a power law, the cubic approximation does better, and the two approximations converge at about the same rate. The error due to either approximation is well below 0.1% when $\mathcal{N} \geq 100$. We present the error due to the cubic approximation at $\mathcal{N} = 100$ for the remaining wavelengths and inclinations in the lower left panel of Figure 2.7. The picture in Figure 2.6 is typical across wavelengths and stars, although the advantage of the cubic approximation and the performance of each scheme all tend to decrease as $\omega \to 1$. The latter behavior is not surprising, given the discussion of the associated limit earlier in this Section. To characterize a possibly worst-case scenario, we compute the error in equation (2.68) for a star that combines $\omega = 0.999$ with Vega's M, L, and R_e. The lower right panel of Figure 2.7 present the result of this calculation on a grid of inclinations, for each wavelength in CK04. The error remains no higher than 0.1% for all wavelengths above 100 nm, where the spectra are appreciably nonzero. We use $\mathcal{N} = 100$ for all models in this work, unless stated otherwise.

Figure 2.8 compares the observed spectrum of Vega from Bohlin et al. (2014) with the star's synthetic spectrum at the inclination from YP10 and distance from van Leeuwen (2007). It also shows the synthetic star's spectrum at $i = \pi/2$ (were we to view Vega edge-on), with lower intensity and a redder spectrum indicative of the cooler equatorial

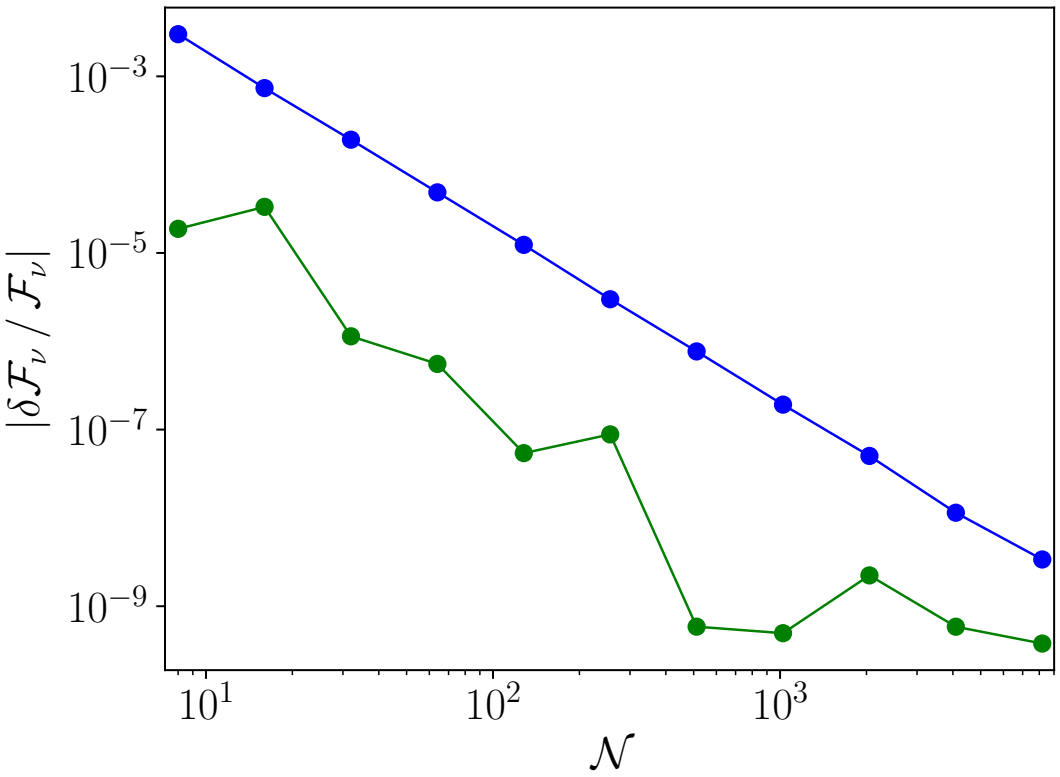

Figure 2.6 Relative flux error due to integration in $\tilde{z}$ for synthetic Vega at $i = \pi/4$ and $\lambda = 511$ nm as a function of the number of abscissae at the equator and above (see Section 2.4). Blue and green points correspond to the trapezoidal and cubic approximations, respectively.

regions. The observed spectrum and the synthetic spectrum at YP10's inclination are quite close, indicating the accuracy of the synthetic star's parameters. Figure 2.8 may be compared with Figures 8 and 9 in Aufdenberg et al. (2006), where the parameters of a stellar model are fit to Vega's observed spectrum.

Given pre-computed $\{a_{kj}\}$ on CK04's parameter grid in Section 2.3.1, we split the remaining computation for a specific star into an inclination-independent and an inclination-dependent portion. The former includes the calculation of $\tilde{r}(\tilde{z})$ and $\tilde{A}(\tilde{z})$ in Section 2.2.1, $g(\tilde{z})$ and $T(\tilde{z})$ in Section 2.3.3, and $\{a_{kj}(\tilde{z})\}$ in Section 2.3.4 (via interpolation over T

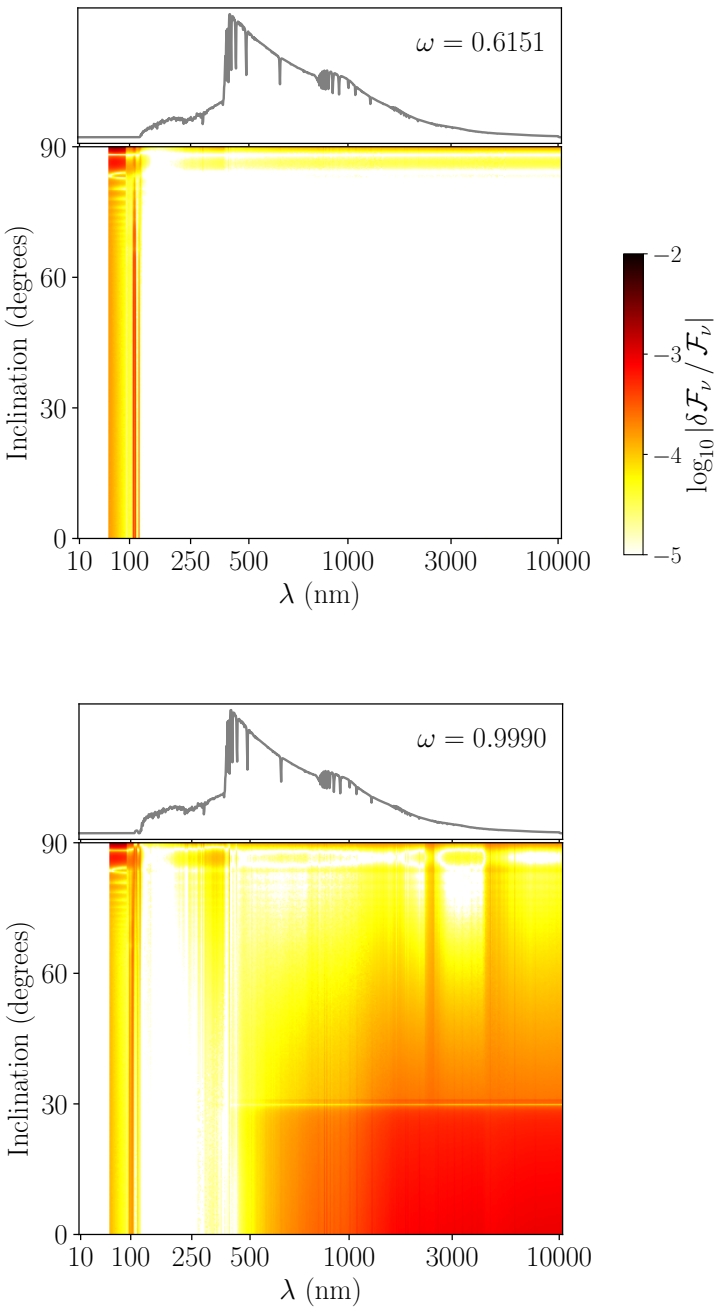

Figure 2.7 Color scheme: relative flux error due to the cubic approximation of the integral in $\tilde{z}$ with $\mathcal{N} = 100$ for two synthetic stars with Vega's M, L, and R_e. See Section 2.4 for details. Grey lines: the stars' spectra at $i = 0°$ (pole-on). The star in the top panels has Vega's ω from YP10. The star in the bottom panels has $\omega = 0.999$; below 100 nm, its spectra do not rise above 0.02% of their maxima; at 100 nm and above, the maximum error from our discretization in $\tilde{z}$ is 0.1%.

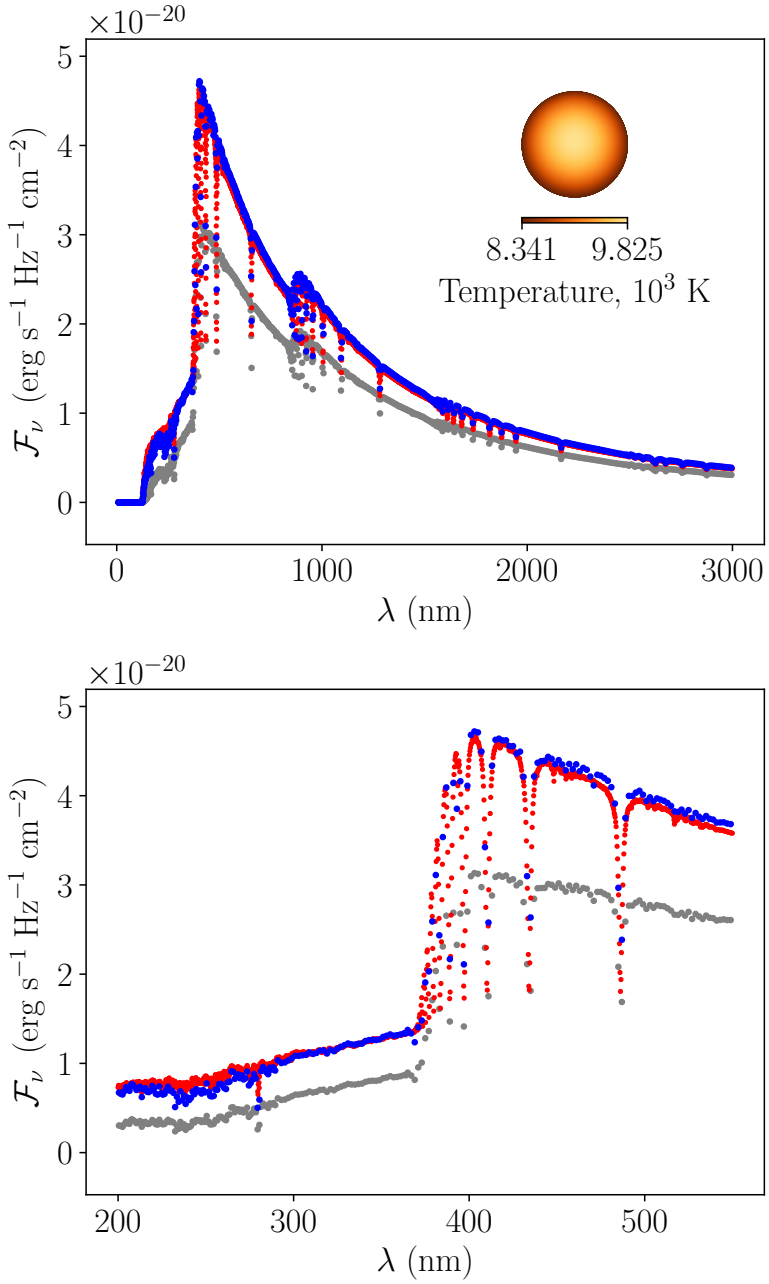

Figure 2.8 Top panel: Synthetic spectrum of Vega computed using its observed parameters (blue points) compared to the observed spectrum (red points). The two spectra agree well. The gray points correspond to a synthetic Vega viewed edge-on and show a significantly fainter and redder star. The inset shows the local effective temperature across the visible surface of the synthetic star at its observed inclination of $\sim 5^\circ$ (YP10). Bottom panel: same as the top panel, with wavelength range restricted to the Balmer jump.

and g). The inclination-dependent portion includes the calculation of $\tilde{z}_b$ in Section 2.2.3, $\{P_{kj}(\tilde{z})\}$ in Section 2.3.2, and the one-dimensional integral in this section. On a 2.3 GHz MacBook Pro with 8 GB of RAM, inclination-independent computation with $\mathcal{N} = 100$ takes about 800 ms. Thereafter, the inclination-dependent computation takes about 30 ms per inclination, so that the full synthetic spectrum at 50 inclinations takes $\sim$2 seconds.

2.5 Extensions

2.5.1 Color-magnitude diagrams

Photometry is available for many more stars, and star clusters, than spectroscopy. As a result, much of the recent work studying the observational consequences of rapid stellar rotation has used color-magnitude diagrams (e.g. Bastian & de Mink, 2009; Brandt & Huang, 2015b; D'Antona et al., 2015; Goudfrooij et al., 2017; Gossage et al., 2019). Our spectra may be easily used to compute colors and magnitudes in any photometric system.

Here, we briefly show the consequences of inclination for rapidly rotating stars in the color-magnitude diagram. For a given filter in Rodrigo et al. (2012), we approximate the transmission curve $T(\lambda)$ via third-order spline interpolation between the discrete points with available transmission values. We also convert the previously calculated $\mathcal{F}_\nu(\lambda)$ to $\mathcal{F}_\lambda(\lambda)$:

$$\mathcal{F}_\lambda(\lambda) = \frac{c}{\lambda^2}\,\mathcal{F}_\nu(\lambda). \tag{2.69}$$

Next, we estimate the star's flux through the filter,

$$\mathcal{F} = \int_0^\infty \mathcal{F}_\lambda(\lambda)\, T(\lambda)\, d\lambda, \tag{2.70}$$

via the application of the trapezoidal rule over the variable-size intervals between nearest-neighbor λ values in CK04. Finally, we calculate the magnitude:

$$m = -2.5 \log_{10} \frac{\mathcal{F}}{\mathcal{F}_0 \int_0^\infty T(\lambda)\, d\lambda}, \tag{2.71}$$

where $\mathcal{F}_0$ is the flux zero point in the Vega calibration system and the integral is approximated the same way as the one in equation (2.70).

We calculate the magnitudes corresponding to the Generic Bessel B and V filters in Rodrigo et al. (2012) for a single star with Vega's physical parameters, but observed at inclinations from 0 to $\pi/2$. Figure 2.9 shows the resulting range of $(B-V, V)$. The black arrow indicates Vega's actual inclination. A similar calculation with a range of stellar models would produce a smooth distribution suitable for comparison with observed color-magnitude diagrams.

2.5.2 Planetary transits

Introduction

Rapid stellar rotation can have an observable effect on the light curve of a planetary transit: the transit will be deeper or shallower as the planet transits hotter or cooler parts

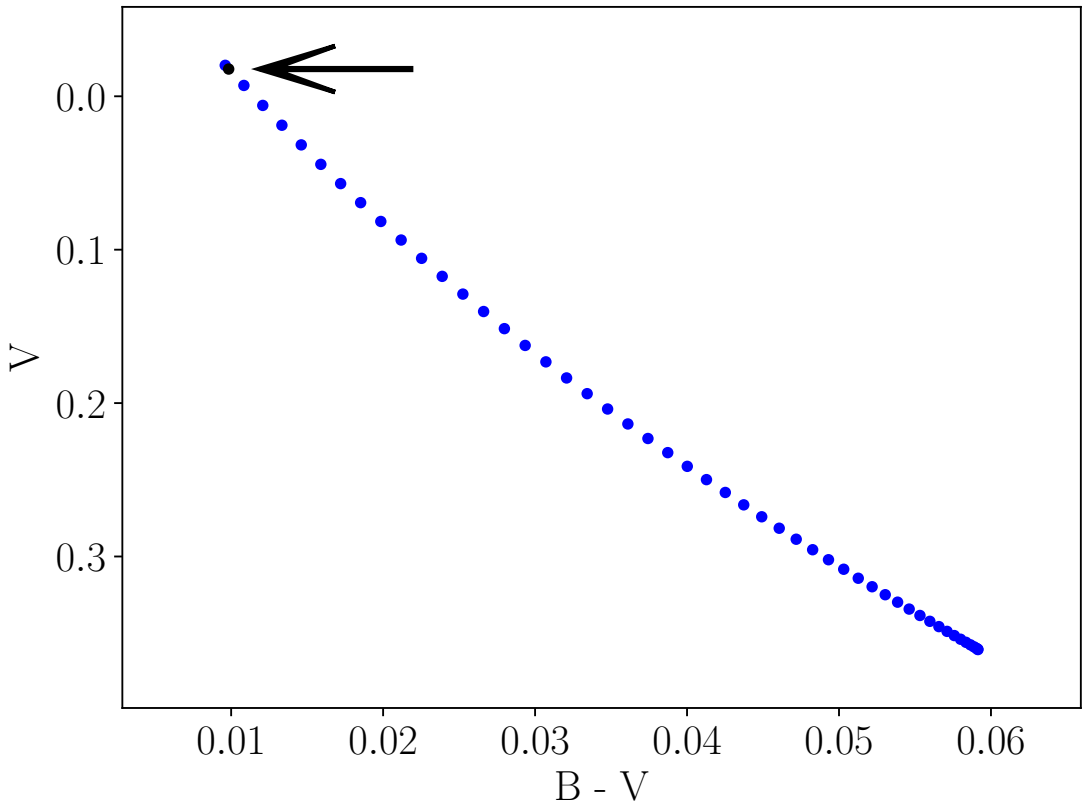

Figure 2.9 Visual magnitude versus the difference between blue and visual magnitudes of synthetic Vega. From left to right, inclination increases from 0 to $\pi/2$. Markers are spaced evenly in $\cos i$, corresponding to isotropically distributed i (e.g., Corsaro et al., 2017). The black marker and arrow indicate the star's observed inclination.

of the stellar surface (Barnes, 2009). This effect can constrain the projected obliquity, the angle between the star's angular momentum, and the planet's orbital angular momentum (Barnes, 2009; Barnes et al., 2011; Masuda, 2015). In this section we extend our tool to rigorously compute the light curve of a planet obliquely transiting a rapidly rotating star.

Consider a planet of radius R_1 that transits its host star. In our coordinate system, $\hat{\mathbf{y}} \perp \hat{\mathbf{i}}$. We let $\hat{\mathbf{z}}' \equiv \hat{\mathbf{i}} \times \hat{\mathbf{y}}$ and refer to the plane spanned by $\hat{\mathbf{y}}$ and $\hat{\mathbf{z}}'$ as the view plane. Over the course of the transit and in projection onto the view plane, the planet's center

traces a straight line with projected impact parameter b with respect to the star's center and projected obliquity $\alpha \in [-\pi/2, \pi/2]$ with respect to the star's rotational axis.

Intensity at a sight line

Slices of the stellar surface perpendicular to the z-axis are circles with centers $(0, 0, z)$ and radii r, with $z \in [-R_p, R_p]$. Their projections onto the view plane are ellipses that satisfy

$$\left(\frac{z' - z\sin i}{r\cos i}\right)^2 + \left(\frac{y}{r}\right)^2 = 1. \tag{2.72}$$

With $u' \equiv z'/R_e$ and $\tilde{y} \equiv y/R_e$, Equation (2.72) can be re-written as

$$\tilde{r}^2 = (u'\,\sec i - u\,\tan i)^2 + \tilde{y}^2. \tag{2.73}$$

Given a sight line through point $(\tilde{y}, u')$ in the view plane, we wish to find the point $(\tilde{r}, \phi, u)$ on the stellar surface where the sight line's light originates. Pairs of $u \in [-z_b/R_e, z_b/R_e]$ and $\tilde{r} \in [0, 1]$ that satisfy both Equation (2.4) and Equation (2.73) correspond to the surface points that the sight line pierces. To find these points, we substitute the right-hand side of Equation (2.73) for $\tilde{r}^2$ in Equation (2.4) and perform algebraic manipulation that produces a 6th degree polynomial equation in u. We then substitute this equation's real roots for u in Equation (2.73) and pick out the ones that correspond to both u and $\tilde{r}^2$ in their respective ranges. There are two roots in the latter category when the sight

line pierces the star and zero such roots when it doesn't. In the former case, the greater root gives the u and, via Equation (2.73), the corresponding $\tilde{r}$ coordinates for the sight line.

Only one additive term,

$$\frac{(u' \sec i)^6 \, \omega^4}{4}, \tag{2.74}$$

contains the highest power of $\sec i$ in the 6th degree polynomial. By a heuristic analogue of the argument in Section 2.3.3, computation of u becomes impossible due to rounding error as i becomes close enough to $\pi/2$ that the ratio of u and expression (2.74) equals Bq, with B's order of magnitude close to 1. This gives the following approximation of the angle at which the procedure stops working:

$$i_b = \arccos\left[\left(\frac{Bq}{4}\right)^{1/6}\right], \tag{2.75}$$

where we set ω and u' to 1 to obtain the worst-case scenario, since Equation (2.74) is then largest. When $i > i_b$, we set $i = \pi/2$, so that $u = u'$ and the sight line pierces the star if and only if $\tilde{y} \leq \tilde{r}$. $B = 16$ and $q = 2 \times 10^{-16}$ yield $i_b = \pi/2 - 0.0031$.

Once we have $\tilde{y}$, u', u, and $\tilde{r}$ for a given sight line, we can compute $\tilde{z} = f \, u$ and

$$\cos\phi = \pm\sqrt{1 - \left(\frac{\tilde{y}}{\tilde{r}}\right)^2}, \tag{2.76}$$

where the negative sign corresponds to the case when the line goes through the upper half of the elliptical projection of its surface slice, i.e. when $u' > u \sin i$. Then, equations (2.36) and (2.37) produce gravity and temperature, which in turn allow us to compute a_{ij} in Equation (2.30) via the interpolation of Section 2.3.4. At that point, equations (2.27), (2.22), and (2.14) give us I_ν at the sight line.

Blocked flux

We wish to estimate $\mathcal{F}_{\nu,1}$, the flux that the planet blocks at a given time point. Multiplied by $D_\star^2$, it is equal to the integral of I_ν over the planet's circular projection, which is similar to the integral in equation (2.1), except that the two-dimensional integration domain is different. The first thought is to use a two-dimensional analogue of a numerical integration method similar to those in Section 2.4.1. For example, we could partition the integration domain into rectangles and employ a midpoint Riemann sum. However, since the integration domain is circular, we modify the latter method by attempting to partition the domain into circles instead. Specifically, let us say we can calculate I_ν at $\mathcal{N}_s$ sight lines within the domain. When $\mathcal{N}_s = 7$, we consider the problem of maximizing the total area of seven congruent, non-overlapping circles that fit within a circle of radius R_1; we call this the packing problem at $\mathcal{N}_s = 7$. Its solution, unique up to circular symmetry, is to place small circles of radius $R_1 \,/\, 3$ at the following locations in the $\hat{\mathbf{y}}\,\hat{\mathbf{z}}'$ coordinate system, with the system's origin shifted to match the center of the planet's projection

(Graham et al., 1998):

$$\frac{R_1}{3}\{(0,0),(\pm 2,0),(\pm 1,\sqrt{3}),(\pm 1,-\sqrt{3})\}. \tag{2.77}$$

One of the small circles covers 1/9 of the integration domain. We approximate its average intensity by I_ν at the circle's center. We then approximate the average intensity over the remaining 2/9 of the domain by the average of all seven I_ν values. This latter average, multiplied by πR_1^2, is thus our estimate of $D_\star^2 \mathcal{F}_{\nu,1}$. Given the known best solutions to the packing problem for $1 < \mathcal{N}_s < 19$, the proportion of the integration domain jointly covered by individual circles is highest for $\mathcal{N}_s = 7$, which thus gives the best estimate of the integral, by this measure. With $\mathcal{N}_s = 19$, we can use the packing in Fodor (1999), which covers more than 7/9 of the domain. An alternative, with any $\mathcal{N}_s$, is picking points from a 2-dimensional distribution that is uniform over the projection. Each method averages I_ν over the representative sight lines and multiplies the result by the planet's projected area to obtain $D_\star^2 \mathcal{F}_{\nu,1}$.

We calculate the star's transit-free flux through the Generic Bessel V filter via the right-hand side of equation (2.70) and call it $\mathcal{F}_{\max}$. At every time point, we use equations (2.69) and (2.70) to calculate blocked flux $\mathcal{F}_1$ through the same filter, with $\mathcal{F}_{\nu,1}$ instead of $\mathcal{F}_\nu$. Figure 2.10 presents plots of

$$-\frac{\mathcal{F}_1}{\mathcal{F}_{\max}} = \frac{\mathcal{F} - \mathcal{F}_{\max}}{\mathcal{F}_{\max}}$$

versus time, for two different systems. The plots resemble the curves predicted for similar

systems in Barnes (2009). Here, $\mathcal{F}$ is the star's flux during transit.

Computation of the transit curves in Figure 2.10 starts with the star's inclination-independent calculation at $\mathcal{N} = 100$, which takes about 800 ms on a 2.3 GHz MacBook Pro with 8 GB of RAM (see the end of Section 2.4.2). Thereafter, calculation of blocked flux takes about 1.1 ms per sight line. The resulting total time for two transit curves with 200 time points each and 7 sight lines per time point is $\sim$4 seconds.

In the software implementation of the integration scheme that we reference here (Lipatov & Brandt, 2020a), we speed up the calculation of broadband photometry by moving the filtering step from the very end to the very beginning of such calculation. In this implementation, we replace $\mathcal{F}_\nu$ with I_ν and $\mathcal{F}$ with I in equations (2.69) and (2.70), use them to calculate I for every (T, g, μ) grid point, obtain $I(\mu)$ fits for every (T, g), perform the two-dimensional integration as before, and finally calibrate to the standard magnitude system via equation (2.71). This change leads to a speed-up by a factor of about 5 when each star is treated at ten inclinations. For Generic Bessel B/V and HST ACS WFC F435W/F555W/F814W filters (Rodrigo et al., 2012), the associated errors in $I(\mu)$ fits do not exceed the equivalent $I_\nu(\mu)$ errors in Section 2.3.1.

2.6 Conclusion

We have presented PARS (Paint the Atmospheres of Rotating Stars) – a scheme for the integration of specific intensities over the surface of a rotating star to obtain the star's spectrum. Inputs to the scheme include the star's mass, luminosity, equatorial radius,

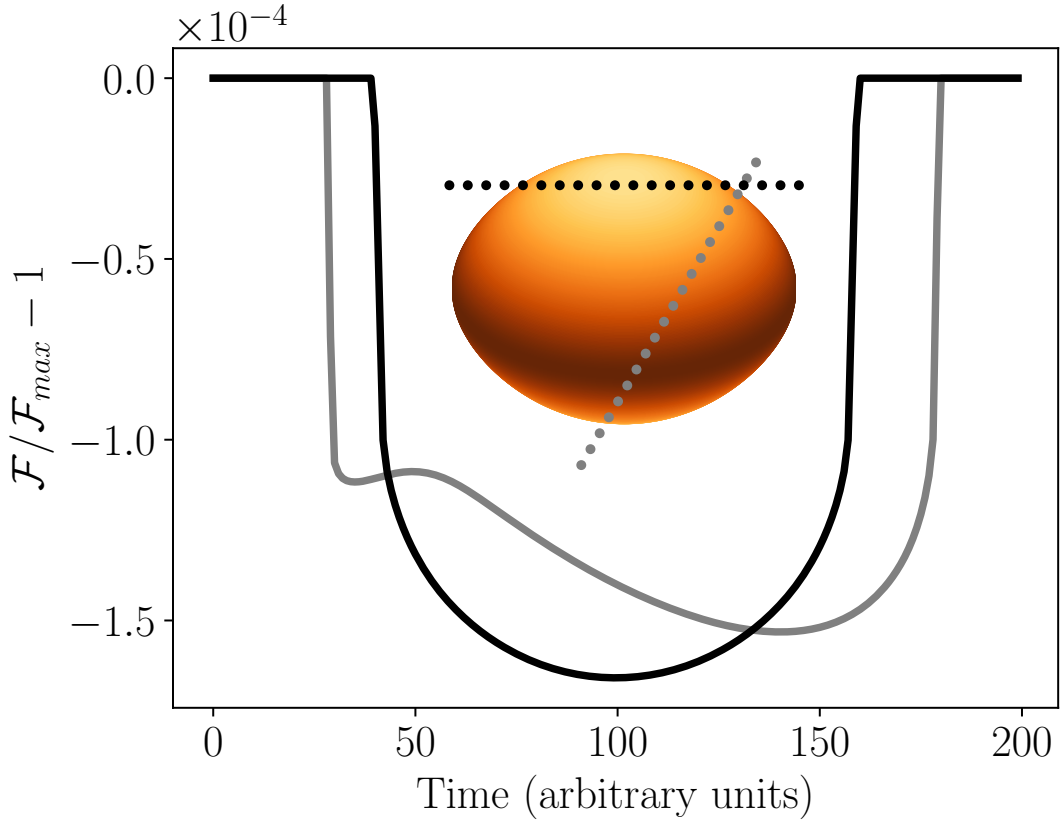

Figure 2.10 Synthetic light curves in the Generic Bessel V filter (Rodrigo et al., 2012) of two separate transits by fictitious Jupiter-sized ($R_1 = 0.01 R_e$) planets orbiting Achernar. Inset: markers show the planets' progress from left to right, the orange color scheme traces local effective temperature on the stellar surface; each planet is enlarged for clarity. The black markers and line indicate a transit at $b = 0.6$ and $\alpha = 0$; grey symbols correspond to a transit at $b = -0.3$ and $\alpha = \pi/3$ (see Section 2.5.2). The blocked flux at each time point was computed from 7 packed-circle sight lines; the resulting light curves are indistinguishable from those based on about 100 random sight lines at each point.

rotational speed, and inclination.

We forgo differential rotation and volume-wide mass distribution in favor of solid-body rotation and a Roche model, respectively. This allows us to compute a closed-form expression for surface shape in cylindrical coordinates, based on Espinosa Lara & Rieutord (2011), a.k.a. ER11. We then obtain closed-form expressions for the differential

area element, cosine of the viewing angle μ, and effective surface gravity g. We also adopt ER11's assumption that energy flux and gravity are collinear, which allows us to compute surface effective temperature T with high precision up to 99.9% of maximum rotation rate.

An important input to our scheme is a set of stellar atmosphere models (such as in Castelli & Kurucz, 2004, a.k.a. CK04), with intensity I_ν on a grid of μ, T, and g. We model $I_\nu(\mu)$ as a piecewise 4th degree polynomial on a partition of μ's range and interpolate the polynomial coefficients in $\log g$ and the Planck function factor that involves T.

The polynomial form of $I_\nu(\mu)$, in combination with the closed-form expression for μ, gives a closed-form expression for the indefinite integral in the azimuthal direction. The definite integral results from an algorithm that keeps track of the μ interval entered by the integration. We separately apply two cubic-fit numerical approximations to the longitudinal integrals below and above the equator, in view of abrupt intensity changes across this latitude at high rotational velocities.

Our scheme enables rapid calculation of synthetic spectra, taking just $\sim$2 seconds on a laptop computer to compute 1221-wavelength spectra at 50 inclinations. This, coupled with libraries of stellar models, will enable rigorous comparisons with data wherever the effects of stellar rotation are important. We highlight two examples: observed color-magnitude diagrams of star clusters and transit light curves. In future work we will further develop these applications.

Individual spectral lines are not resolved with the atmosphere models we use in this chapter, though higher-resolution models can constitute input to PARS. On a related note, PARS does not generally account for the rotational Doppler effect. However, we do plan to utilize the scheme's framework to calculate the expected broadening of individual spectral lines in the future.

PARS Python source code is available for download and installation (Lipatov & Brandt, 2020a). We have tested and run the software on a Unix operating system included with macOS 10. There is potential for porting PARS to other operating systems, as its core doesn't require the import of rare or highly specialized modules.

Chapter 3

Effects of Rotation on the Spectra of Brown Dwarfs

In this chapter, we adapt the software `PARS`, which we introduced in Chapter 2, to predict and explore the effects of rotation on the spectra of brown dwarfs. In constructing synthetic spectra of stars, we fed `PARS` plane-parallel model atmospheres by Castelli & Kurucz (2004, a.k.a. CK04). CK04's models, however, are not appropriate for brown dwarfs, whose atmosphere temperatures are below the lower limit of the models' temperature range. Accordingly, the atmosphere models that serve as input to `PARS` in this chapter are the Sonora brown dwarf 1D climate and chemistry models (Marley et al., 2021), with specific intensities computed using open-source code `PICASO` (Batalha et al., 2019; Batalha et al., 2022).

`PARS` approximates the mass distribution via the Roche model, wherein all mass is

concentrated at the gaseous object's center. Brown dwarfs deviate significantly from the Roche model, so that the latter predicts higher rotational speeds from these objects' oblatenesses than the objects' observed speeds. Accordingly, in adapting `PARS` to the study of an observed brown dwarf, we feed the software the rotational speed that corresponds to the object's observed oblateness under the Roche model, so that the centrifugal deformation that is assumed by `PARS` is close to the object's observed deformation.

The contents of this chapter have been submitted for publication in Monthly Notices of the Royal Astronomical Society (MNRAS), under the title "Effects of Rotation on the Spectra of Brown Dwarfs" (Lipatov, Brandt, and Batalha, 2022).

3.1 Rotation and Mass Distribution Models

In this section, we introduce our rotation model and two mass distribution models for brown dwarfs. Of these, the rotation model and the Roche model of mass distribution were previously shown to accurately predict spectra of A-type rotating stars (Lipatov & Brandt, 2020b, henceforth LB20).

We assume that a given brown dwarf rotates at some uniform angular speed Ω. The resulting centrifugal forces cause the object's equatorial radius to be greater than its polar radius. In other words, rotation leads to non-zero oblateness f, a quantity that we define as

$$f \equiv \frac{R_{\rm e} - R_{\rm p}}{R_{\rm e}}, \tag{3.1}$$

where $R_{\rm e}$ is the dwarf's equatorial radius and $R_{\rm p}$ is its polar radius. Re-arrangement of Equation (3.1) yields the polar radius as a function of equatorial radius and oblateness:

$$R_{\rm p} = R_{\rm e}(1 - f). \tag{3.2}$$

Another useful quantity to consider is the dimensionless rotational velocity, $\omega \equiv \Omega/\Omega_{\rm K} \in [0, 1)$. Here, $\Omega_{\rm K}$ is the Keplerian rotational limit – the maximum angular velocity that the rotator can have without breaking up.

In general, there are no simple expressions for either ω or $\Omega_{\rm K}$ in terms of the dwarf's fundamental parameters such as mass, radius, or oblateness. On the other hand, useful and relatively simple expressions for ω and $\Omega_{\rm K}$ exist under the assumption of the Roche mass distribution, which places all mass at the brown dwarf's center. Given the Roche distribution, the Keplerian limit is

$$\Omega_{\rm K} = \frac{GM}{R_{\rm e}^3}. \tag{3.3}$$

The Roche distribution further implies Equation (2) in LB20,

$$\frac{R_{\rm e}}{R_{\rm p}} = 1 + \frac{\omega_{\rm R}^2}{2}, \tag{3.4}$$

where $\omega_{\rm R}$ is the theoretical value of ω that yields the observed ratio of equatorial and polar radii under the assumption of the Roche distribution. Relatedly, $\omega_{\rm R}$ yields the

observed oblateness, as well. To see this, we combine Equation (3.4) with Equation (3.1) to get oblateness in terms of ω_{R},

$$f(\omega_{\mathrm{R}}) = \frac{1}{1 + 2/\omega_{\mathrm{R}}^2}. \tag{3.5}$$

We then invert Equation (3.5) to obtain

$$\omega_{\mathrm{R}}(f) = \sqrt{\frac{2f}{1-f}}. \tag{3.6}$$

Relaxation of the Roche distribution assumption allows for a more realistic internal mass distribution. Under these conditions and a certain set of approximations, the Darwin-Radau relation connects the moment of inertia of a brown dwarf to its oblateness and rotational speed (Barnes & Fortney, 2003):

$$\mathbb{C} = \frac{C}{MR_{\mathrm{e}}^2} = \frac{2}{3}\left[1 - \frac{2}{5}\left(\frac{5}{2}\frac{\omega^2}{f} - 1\right)^{1/2}\right]. \tag{3.7}$$

Here, C is the moment of inertia about the rotational axis and $\mathbb{C}$ is the corresponding dimensionless quantity. Spacecraft gravity field observations estimate that $\mathbb{C} = 0.276$ for Jupiter (Ni, 2018). The Darwin-Radau relation, in combination with the observed oblateness and rotational velocity, yields $\mathbb{C} = 0.22$ for Saturn (Fortney et al., 2018). For a uniform-density sphere, $\mathbb{C} = 0.4$. We can re-write Equation (3.7) to obtain f in terms

of ω and $\mathbb{C}$:

$$f(\omega, \mathbb{C}) = \frac{40\,\omega^2}{116 - 300\,\mathbb{C} + 225\,\mathbb{C}^2}. \tag{3.8}$$

When $\mathbb{C} = 0$, Equation (3.8) reduces to $f = \omega^2/2.9$. For $\omega \in [0, 1)$ and $\omega \equiv \omega_{\rm R}$, this equation is numerically similar, although not identical, to Equation (3.5). Although the latter assumes a mass distribution with $\mathbb{C} = 0$, it does so under a different set of approximations. Thus, when the moment of inertia approaches zero, the Darwin-Radau expression for oblateness becomes similar but not quite identical to the Roche distribution expression.

Finally, we can re-write Equation (3.7) to express dimensionless rotational speed in terms of oblateness and the moment of inertia:

$$\omega(f, \mathbb{C}) = \sqrt{\frac{1}{40}\, f\,(116 - 300\,\mathbb{C} + 225\,\mathbb{C}^2)}. \tag{3.9}$$

In the rest of this chapter, we denote the observed rotational speed of brown dwarfs by ω and assume that it relates to observed oblateness via the Darwin-Radau relation. On the other hand, at times we will also calculate $\omega_{\rm R}$ – the rotational speed that yields the observed oblateness under the assumption of the Roche model.

3.2 Computation of Spectra

3.2.1 Spectral Intensity as a Function of Surface Parameters

We compute plane-parallel-derived spectra using the pressure-temperature, and abundance profiles from the Sonora cloud-free solar metallicity grid (Marley et al., 2021), which is available on Zenodo (Marley et al., 2018). The cloud-free atmospheres exist on a grid of gravity and effective temperature in the range of: $3.25 \leq \log g \leq 5.5$ and $200 \leq T_{\rm eff} \leq 2400$ K. Therefore, they are particularly relevant for relatively low temperatures, such as those associated with Model 880, since we do not expect clouds at these temperatures. Even though higher brown dwarf temperatures are associated with clouds, we use the cloud-free atmospheres for higher-temperature models as well, since our main goal is to show the qualitative effect of rotation on brown dwarf spectra.

Using the Sonora pressure-temperature, and abundance profiles, we compute the specific intensity in $\mathrm{erg\,s^{-1}\,Hz^{-1}\,sr^{-1}\,cm^{-2}}$ on a grid of the cosine of the viewing angle $\mu = \cos\phi$, wavelength λ, surface effective temperature, and surface gravitational acceleration using version 2.3 of the open source code `PICASO` (Batalha et al., 2019; Batalha et al., 2022), which has previously been used to compute the thermal emission spectra of brown dwarfs (e.g. Mang et al., 2022) and exoplanets (e.g. Robbins-Blanch et al., 2022).

`PICASO` uses the same radiative transfer methodology (Marley & McKay, 1999) and opacities (Freedman et al., 2014; Lupu et al., 2022) as those used to compute the final pressure-temperature profiles, described in (Marley et al., 2021). Specifically, it uses the

(Toon et al., 1989) source function technique and includes the molecular and atomic opacities for C_2H_2, C_2H_4, C_2H_6, CH_4, CO, CO_2, CrH, Cs, FeH, H_2O, H_2S, HCN, K, Li, LiCl, MgH, N_2, NH_3, Na, OCS, PH_3, Rb, SiO, TiO, and VO. They also include continuum opacities for the following interactions: $H_2 - H_2$, $H_2 - He$, $H_2 - H$, $H-$, H_2-.

For each gravity-effective temperature pair available in the Sonora grid, we compute spectra for viewing angles, μ, of: [0.09, 0.18, 0.28, 0.37, 0.45, 0.54, 0.61, 0.68, 0.75, 0.81, 0.86, 0.9, 0.94, 0.97, 0.98, 0.99]. The λ grid consists of 9831 wavelengths between 0.7 and 5 μm, with spectral resolution $R = 5000$. This wavelength grid becomes the grid of our brown dwarf spectra. The temperature range, which is equivalent to that of the Sonora grid, is between 200 and 2400 K, with temperature resolution equal to 25 K below 600 K, 50 K between 600 and 1000 K, and 100 K above 1000 K. The gravity grid is [17, 31, 56, 100, 178, 316, 562, 1000, 1780, 3160] $\mathrm{m\,s^{-2}}$.

We use μ equal to 0.1 and 0.4 as the boundaries of the viewing angle intervals for the piecewise interpolation of intensity as a function of μ by `PARS` (LB20). These viewing angle intervals proved to be optimal in the application of `PARS` to stars.

3.2.2 Disk-Integrated Spectra

To compute disk integrated spectra of rotating brown dwarfs, we pass the plane-parallel-derived spectra to Paint the Atmospheres of Rotating Stars (`PARS`) – software that quickly and accurately computes spectra of self-gravitating rotating gaseous objects such as stars and brown dwarfs (LB20). `PARS` computes the surface shape and the local effective tem-

perature everywhere on the surface under the assumption of the Roche mass distribution, then integrates specific intensities over the surface to get a spectrum. To achieve this, `PARS` needs specific intensities as a function of effective temperature, effective surface gravity, and surface viewing angle — which are generally provided in the form of a library of plane-parallel atmosphere models.

One of the inputs to `PARS` is the dimensionless rotational velocity we discuss in Section 3.1. The gravity darkening effects we wish to compute are largely a function of geometric distortion, epitomized by oblateness. Thus, given a model with oblateness f, we calculate velocity ω_{R} using Equation (3.6) and provide `PARS` with this velocity value. This ensures that the `PARS` model has the correct oblateness. Other brown dwarf parameters that serve as part of the input to `PARS` are mass M, equatorial radius R_{e}, luminosity L and distance. For all our models, we adopt a fiducial distance of 10 parsecs. Table 3.1 and Section 3.3 describe the process that yields the remaining parameters.

3.3 Brown Dwarf and Exoplanet Case Studies

We construct model brown dwarfs that span a range of rotation rates and effective temperatures; we ultimately compute their synthetic spectra as described in Section 3.2. Our models are inspired, in particular, by two very fast-rotating brown dwarfs in the literature, J0348-6022 and J0407+1546 (Tannock et al., 2021, hereafter T21). We also construct a model inspired by β Pictoris b, one of the first imaged exoplanets (Lagrange et al., 2009, 2010) and an object near the deuterium-burning boundary (Chilcote et al.,

2017; Brandt et al., 2021). The upper half of Table 3.1, above the mid-table horizontal line, lists the literature-based parameters of the three above-mentioned substellar objects. The lower half lists the parameters we assume or derive. Bold text indicates the parameters that serve as input to the synthetic spectrum software, `PARS`. In this section, we examine the process that yields all the parameters in Table 3.1.

3.3.1 J0348-6022

Object 2MASS J03480772-6022270, a.k.a. J0348-6022, is a rapidly rotating brown dwarf with spectral type T7. Table 3.1 presents T21's estimates of this dwarf's mass M, equatorial radius $R_{\rm e}$, rotational period $P_{\rm rot}$, oblateness f, and surface temperature $\bar{T}_{\rm eff}$. We assume the surface temperature estimate to be some average over the gravity-darkened dwarf surface. Our work does not aim to draw specific conclusions about this or other astrophysical objects. Instead, our goal is to demonstrate the effects of rotation on the spectra of such objects in general. Thus, our conclusions do not require object parameter values that are more exact than the ones we present. All our brown dwarf models inspired by J0348-6022 have the same mass, $M = 0.041\,M_{\odot}$.

Equation (3.2) yields the polar radius $R_{\rm p}$ of our J0348-6022 model. With $R_{\rm avg} = (R_{\rm e} + R_{\rm p})/2$, we set the dwarf's luminosity L to

$$L = 4\pi R_{\rm avg}^2 \sigma_{\rm SB} \bar{T}_{\rm eff}^4, \tag{3.10}$$

where $\sigma_{\rm SB}$ is the Stefan-Boltzmann constant. In Equation (3.10), $4\pi R_{\rm avg}^2$ is close to,

Table 3.1. Parameters of our three main substellar models.

Name	J0348-6022 (Model 880)[a]	J0407+1546[a]	β Pictoris b[b]
Spectral Type	T7	L3.5	L2
$\mathbf{M}\,(\mathbf{M_{Jup}})$	**42.9**	**67.0**	**12.9**
$\mathbf{R_e}\,(\mathbf{R_{Jup}})$	**0.905**	**0.973**	**1.46**
$\bar{T}_{\rm eff}$ (K)	880	1840	1724
$P_{\rm rot}$ (h)	1.08	1.23	
$v \equiv v_{\rm e} \sin i$ (km/s)			25
i			$\pi/2$[c]
$f \equiv \frac{R_{\rm e}-R_{\rm p}}{R_{\rm e}}$	0.08	0.05	0.029[d]
$R_{\rm avg} \equiv \frac{R_{\rm e}+R_{\rm p}}{2}$ $(R_{\rm Jup})$	0.869	0.949	1.44
$\mathbf{L} = 4\pi R_{\rm avg}^2 \sigma_{\rm SB} \bar{T}_{\rm eff}^4$ $(\mathbf{L}_\odot)$	$\mathbf{4.3 \times 10^{-6}}$	$\mathbf{9.8 \times 10^{-5}}$	$\mathbf{1.7 \times 10^{-4}}$
$\Omega = 2\pi/P_{\rm rot}$ $(\mathrm{rad\,s^{-1}})$	0.0016	0.0014	
$\Omega = v/(R_{\rm e} \sin i)$ $(\mathrm{rad\,s^{-1}})$			0.00024
$\Omega_{\rm K} = \sqrt{GM/R_{\rm e}^3}$ $(\mathrm{rad\,s^{-1}})$	0.0045	0.0050	0.0012
$\omega = \Omega/\Omega_{\rm K}$	0.36	0.28	0.20
$\mathbb{C} = C/(MR_{\rm e}^2)$	0.20[e]		0.25[f]
$\boldsymbol{\omega}_{\rm R} = \mathbf{2f/(1-f)}$[g]	**0.42**	**0.32**	**0.24**

[a]Parameters Reference: Tannock et al. (2021)

[b]Parameters Reference: Chilcote et al. (2017)

[c]Assuming that the direction of the brown dwarf's spin angular momentum is the same as those of its star's spin, orbital, and circumstellar disk angular momenta (e.g., Kraus et al., 2020).

[d]From ω and the Darwin-Radau relation, assuming $\mathbb{C} = 0.25$.

[e]Computed from f and ω according to Equation (3.7).

[f]Similar to estimates for Jupiter (Ni, 2018) and Saturn (Fortney et al., 2018).

[g]Dimensionless rotational velocity ω corresponding to oblateness f under the Roche model.

but not equal to, the surface area of the star; $\bar{T}_{\rm eff}$ represents a characteristic effective temperature.

We also compute the rotation speed as $\Omega = 2\,\pi/P_{\rm rot}$, the Keplerian limit $\Omega_{\rm K}$ via Equation (3.3), the dimensionless rotational speed as $\omega = \Omega/\Omega_{\rm K}$, and the dimensionless moment of inertia from oblateness f and ω according to Equation (3.7). Furthermore, we use Equation (3.6) to compute the rotational speed $\omega_{\rm R}$ that would produce the observed oblateness f under the assumption of the Roche distribution.

Model Variants

In order to explore the effects of rotation on the inference of brown dwarf parameters from nonrotating models, we create a set of models based on J0348-6022 with a variety of luminosities and rotational speeds.

We first consider the J0348-6022 model from Table 3.1, with its oblateness $f = 0.08$, dimensionless rotational speed $\omega = 0.36$, dimensionless moment of inertia $\mathbb{C} = 0.20$, Roche model equivalent speed $\omega_{\rm R} = 0.42$, average effective temperature $\bar{T}_{\rm eff} = 880\,{\rm K}$, luminosity $L = 4.3 \times 10^{-6}\,L_\odot$, and equatorial radius $R_{\rm e} = 0.905\,R_{\rm Jup}$. We call this Model 880 and use `PARS` software (LB20) to determine the effective temperatures $T_{\rm eff}$ of its equator and poles; Section 3.2 describes the function of `PARS` in more detail. We then determine the luminosities of nonrotating dwarfs that correspond to the equatorial and

polar effective temperatures via

$$L = 4\pi R_{\rm avg}^2 \sigma_{\rm SB} T_{\rm eff}^4, \tag{3.11}$$

where $R_{\rm avg}$ remains constant, corresponding to constant oblateness and equatorial radius. Finally, we create a set of nonrotating models with effective temperatures (and hence luminosities) that are intermediate between the equatorial and polar values of Model 880. In Section 3.4 we will compare the properties of these nonrotating models to the inclination-dependent observables of the rotating version of Model 880.

We also create a set of models by reducing the rotation rate $\omega_{\rm R}$ of Model 880 more gradually. As $\omega_{\rm R}$ decreases, oblateness decreases according to Equation (3.5) and so does the difference between the equatorial and polar radii. We keep luminosity and $\bar{T}_{\rm eff}$ constant in Equation (3.10) by holding $R_{\rm avg} = (R_{\rm e} + R_{\rm p})/2$ constant as oblateness varies. To achieve this, we substitute for the polar radius according to Equation (3.4) in the definition of $R_{\rm avg}$ and obtain

$$R_{\rm avg} = \frac{R_{\rm e} + R_{\rm p}}{2} = \frac{R_{\rm e}}{2}\,\frac{2 + \omega_{\rm R}^2/2}{1 + \omega_{\rm R}^2/2}, \tag{3.12}$$

so that

$$R_{\rm e} = 2\,R_{\rm avg}\,\frac{2 + \omega_{\rm R}^2}{4 + \omega_{\rm R}^2}. \tag{3.13}$$

Thus, as we reduce ω_R in discrete steps, we keep $R_{\rm avg}$ constant at the values of Model 880 by setting the equatorial radius according to Equation (3.13). This allows us to keep both $\bar{T}_{\rm eff}$ and L constant in Equation (3.10). We keep $\mathbb{C}$ constant, as well. The new models have oblatenesses given by Equation (3.5) and actual dimensionless rotational speeds ω given by Equation (3.9). These rotating models span a range of rotational velocities, all with characteristic effective temperature $\bar{T}_{\rm eff} = 880\,{\rm K}$.

We next create Model 600, which has $\bar{T}_{\rm eff} = 600\,{\rm K}$, while retaining the geometry, mass distribution, and rotational speed properties of Model 880. Given that Model 600 has $R_{\rm avg} = 0.0893\,R_\odot$, Equation (3.10) tells us that this model's luminosity is $9.3 \times 10^{-7}\,L_\odot$. We then create nonrotating models at different effective temperatures and rotating models at different rotational speeds that correspond to Model 600 and its average effective temperature, the same way we created such variations for Model 880.

Similarly, we create Models 400 and 1500, which have the effective temperatures implied by their names and respective luminosities equal to $1.8 \times 10^{-7}\,L_\odot$ and $3.6 \times 10^{-5}\,L_\odot$, with other parameters the same as in Models 880 and 600. We make nonrotating and rotating model sets that correspond to each new luminosity, as well.

3.3.2 Additional Case Studies

Object 2MASS J04070752+1546457, a.k.a. J0407+1546, is a rapidly rotating brown dwarf with spectral type L3.5 (T21). It serves as a template for a brown dwarf model with parameters that we obtain in the same way we obtain the parameters for Model 880.

Object β Pictoris (β Pic) b, which is at the giant planet / brown dwarf mass boundary, serves as another model template. We obtain its mass M, equatorial radius $R_{\rm e}$, and average temperature $\bar{T}_{\rm eff}$ from Chilcote et al. (2017). Snellen et al. (2014) measure this object's projected rotational velocity $v \equiv v_{\rm e} \sin i$. Kraus et al. (2020) find that the angular momentum vector of the β Pic stellar photosphere, the angular momentum of the β Pic b orbital movement, and the angular momentum of the system's outer debris disk are well-aligned with mutual inclinations $\leq 3 \pm 5^{\circ}$, which indicates that β Pic b formed in a system without significant primordial misalignments. Given these findings and the orbit's near edge-on orientation, we adopt an inclination of $i = \pi/2$ for the planet's spin. Here and in the rest of this chapter, we define i so that $i = \pi/2$ corresponds to an equator-on view and $i = 0$ – to a pole-on view.

We then obtain the object's angular velocity as $\Omega = v/(R_{\rm e} \sin i)$. At this point, we compute the average radius $R_{\rm avg}$, luminosity L, Keplerian limit $\Omega_{\rm K}$, and dimensionless rotational velocity ω the same way we calculate these parameters for Model 880. We adopt a dimensionless moment of inertia equal to $\mathbb{C} = 0.25$, which is similar to the estimates of this quantity for the giant planets of the Solar system (Ni, 2018; Fortney et al., 2018). Given ω and $\mathbb{C}$, we use Equation (3.8) to calculate an estimate for oblateness f. This, in turn, yields the Roche model equivalent velocity $\omega_{\rm R}$ via Equation (3.6).

We list all the parameters for the models based on J0407+1546 and β Pictoris b in Table 3.1.

3.4 Effects of Rotation

3.4.1 Comparisons to Spectra of Nonrotating Objects

In this section, we address the detectability of gravity darkening from spectra alone. The spectrum of a rotating brown dwarf will contain contributions from different effective temperatures; it will differ from the spectrum of a spherical brown dwarf no matter the temperature of the latter. We aim to quantify the difference between the spectrum of a rotating brown dwarf and the best-matching nonrotating spectrum. This serves as a metric of rotation's spectral detectability that is independent of projected rotational speed $v \sin i$ as measured from line broadening.

In the comparison of a rotating dwarf's flux $x(\lambda)$ to the flux of a nonrotating model $y(\lambda)$, we think of the former as the independent variable and of the latter as the dependent variable. We model $y(x)$ via linear regression. If $\tilde{x} = x - \bar{x}$ and $\tilde{y} = y - \bar{y}$ are the mean-subtracted versions of the two spectra, then the slope of the best-fitting linear model is $b = \sum \tilde{x}\tilde{y} / \sum \tilde{x}^2$. The root mean squared deviation (RMSD) of this best-fitting line from the rotating model spectrum is $\mathrm{RMSD}(\hat{\mathcal{F}}) = \sqrt{\sum (\tilde{y} - b\tilde{x})^2 / n}$, where n is the number of wavelengths at which each spectrum is sampled. The units of this deviation are the same as the units of flux.

`PARS` produces flux density $\mathcal{F}(\lambda)$ in $\mathrm{erg\,s^{-1}\,Hz^{-1}\,cm^{-2}}$ on a grid of wavelengths λ. We calculate a grid of $\tilde{\nu} = 1/\lambda$, which is proportional to frequency in Hz. We then integrate $\mathcal{F}(\tilde{\nu})$ on the grid of $\tilde{\nu}$ using the variable-interval trapezoidal rule. This yields

the integrated flux $\mathcal{F}$ in units that are proportional to $\mathrm{erg\,s^{-1}\,cm^{-2}}$. We divide $\mathcal{F}$ by the range of $\tilde{\nu}$ to obtain the average flux $\bar{\mathcal{F}}$ in $\mathrm{erg\,s^{-1}\,Hz^{-1}\,cm^{-2}}$.

We divide the root-mean-squared deviation, as calculated above, by the average flux density of the rotator within the $1\,\mu$m–$5\,\mu$m interval and minimize the resulting quantity over all nonrotating models. This provides a dimensionless measure of the observable impact of rotation – the smallest difference between a non-rotator's spectrum and a linear transformation of the rotator's spectrum. This minimum normalized RMSD is a function of both rotation rate and orientation.

If there is a nonrotating model that exactly matches the spectral shape and features of a rotating model, then minimum RMSD for that model is zero. If there is no nonrotating model that can match the spectral shape of the rotating model, then the minimum RMSD can be significantly nonzero. The rotating model's spectrum in this case does not look like the spectrum of any nonrotating brown dwarf.

3.4.2 Flux Anisotropy Factor

Rotation breaks the spherical symmetry of a brown dwarf, making the object's bolometric flux depend on the direction from which it is seen. As a result, if one assumes that a rotating dwarf is not rotating and thus spherically symmetric, one tends to over-estimate its luminosity from its flux, if one sees the object pole-on. On the other hand, an equator-on view leads to an under-estimate of the luminosity. In this section, we quantify this effect for a range of rotational speeds and rotational axis inclinations.

Consider brown dwarf A with luminosity L that we wish to know and a spectrum that we observe, with a certain bolometric flux. We allow for the possibility of rotation, anywhere between zero and critical. The true luminosity L will not equal $4\pi r^2$ times the bolometric flux (where r is the distance) because the observed flux varies with viewing angle. Standard practice, however, is to infer the luminosity of a brown dwarf in exactly this way, by assuming isotropic radiation. The flux density is measured at some wavelengths and extrapolated to wavelengths that are not measured and then integrated using a model of a nonrotating brown dwarf.

We reproduce a realistic luminosity inference by assuming that we have a nonrotating model B that matches the observed spectrum of brown dwarf A up to a scaling factor. Model B has luminosity L_0, integrated flux $\mathcal{F}_0$, effective temperature T_0, radius R_0 and distance r. Let p be the ratio of $\mathcal{F}_0$ and the model's total bolometric flux, i.e., the fraction of the bolometric flux within the wavelength range covered by the model spectrum. Given these definitions, the model's luminosity can be written as

$$L_0 = 4\pi\sigma_{\rm SB} R_0^2 T_0^4, \tag{3.14}$$

and its integrated flux – as

$$\mathcal{F}_0 = \frac{1}{r^2}\, p\, \sigma_{\rm SB} R_0^2 T_0^4. \tag{3.15}$$

We are interested in the ratio of the dwarf's true luminosity L and the nonrotating

model's luminosity L_0. Specifically, we wish to know what causes this ratio to deviate from one. We can write L/L_0 as

$$\frac{L}{L_0} = \frac{L}{L_0}\frac{\mathcal{F}_0}{\mathcal{F}}\frac{\mathcal{F}}{\mathcal{F}_0} = \frac{L}{4\pi\sigma_{\rm SB}R_0^2T_0^4}\frac{\frac{1}{r^2}\,p\,\sigma_{\rm SB}R_0^2T_0^4}{\mathcal{F}}\frac{\mathcal{F}}{\mathcal{F}_0} = \frac{L\,p}{4\pi r^2\mathcal{F}} \times \frac{\mathcal{F}}{\mathcal{F}_0}, \tag{3.16}$$

where we have made two substitutions according to Equations (3.14) and (3.15). Let us assume that r and p are the same for the dwarf and the model. In other words, the latter are both at the same distance and require the same bolometric correction for flux that falls outside the observed wavelength range. The last expression of Equation (3.16) consists of two multiplicative terms. The first term is the ratio of $L/(4\pi r^2)$, the bolometric flux we expect if the dwarf is nonrotating and spherically symmetric, to $\mathcal{F}/p$, an approximation of the dwarf's bolometric flux from the observed integrated flux and the fraction of the flux that is in the available wavelength range. The second term is the ratio of the dwarf's integrated flux to the model's integrated flux.

If A does not rotate, then it has a well-defined radius R and effective temperature T. In this case, its luminosity is

$$L = 4\pi\sigma_{\rm SB}R^2T^4 \tag{3.17}$$

and its integrated flux is

$$\mathcal{F} = \frac{1}{r^2}\,p\,\sigma_{\rm SB}R^2T^4. \tag{3.18}$$

Substituting for the first occurrences of L and $\mathcal{F}$ on the right hand side of Equation (3.16) according to Equations (3.17) and (3.18), we obtain $L/L_0 = \mathcal{F}/\mathcal{F}_0$. In other words, if the dwarf does not rotate, then it is sufficient to multiply L_0 by the ratio of integrated fluxes $\mathcal{F}/\mathcal{F}_0$ to obtain L.

On the other hand, if the dwarf rotates with non-zero velocity, multiplication of L_0 by the flux ratio $\mathcal{F}/\mathcal{F}_0$ does not, in general, give us L. We need to additionally multiply our estimate by $L\,p/(4\pi r^2\mathcal{F})$, which we call the anisotropy ratio, since it deviates from one due to the anisotropy of flux because of rotation-induced centrifugal deformation and gravity darkening.

It turns out that the anisotropy ratio is mainly a function of the rotational speed and inclination and that it is otherwise almost independent of other brown dwarf parameters (like mass and temperature). To see this, consider Equation (31) in Espinosa Lara & Rieutord (2011), which tells us that the surface flux at every location on the deformed dwarf's surface is proportional to L/R_e^2, where R_e is the object's equatorial radius. If, additionally, the spatial flux distribution at each location is independent of temperature – the way it is for a black body, this equation implies that multiplication of L/R_e^2 by some factor multiplies the observed flux by the same factor and that the anisotropy ratio $L\,p/(4\pi r^2\mathcal{F})$ doesn't change with luminosity L, object size R_e, or the effective temperature scale, which is proportional to L/R_e^2. The object's mass M does not enter Equation (31) in Espinosa Lara & Rieutord (2011) at all. Thus, we expect that the anisotropy ratio is almost entirely a function of rotational speed ω_R and inclination i.

The anisotropy ratio changes little with mass M and, since the local dependence of intensity on viewing angle broadly matches that of a black body, we do not expect the anisotropy ratio to change significantly with luminosity L or object size $R_{\rm e}$, either. In Section 3.5.3 we will demonstrate this fact quantitatively for our models.

3.5 Results

In this section, we present our findings – the effects of rotation on brown dwarf spectra and the implications of these effects for the inference of brown dwarf parameters from nonrotating models.

3.5.1 Spectral Intensity and Inferred Temperature

Since the polar regions of a brown dwarf are more luminous than the equatorial regions, the entire object's observed specific intensity significantly depends on the inclination of its rotational axis. Since the polar regions are also relatively hot, the temperature that one infers for the dwarf from nonrotating models depends on the inclination, as well. In this section, we quantify these effects for a model inspired by one of the fastest-rotating known dwarfs.

Let us suppose that one of the Model 880 spectra in the upper panel of Figure 3.1 is an observed spectrum of a rotating dwarf. The magnitude of the spectral flux depends greatly on this dwarf's rotational axis inclination. Specifically, there are portions of the spectrum with appreciable intensity where the flux differs by as much as a factor

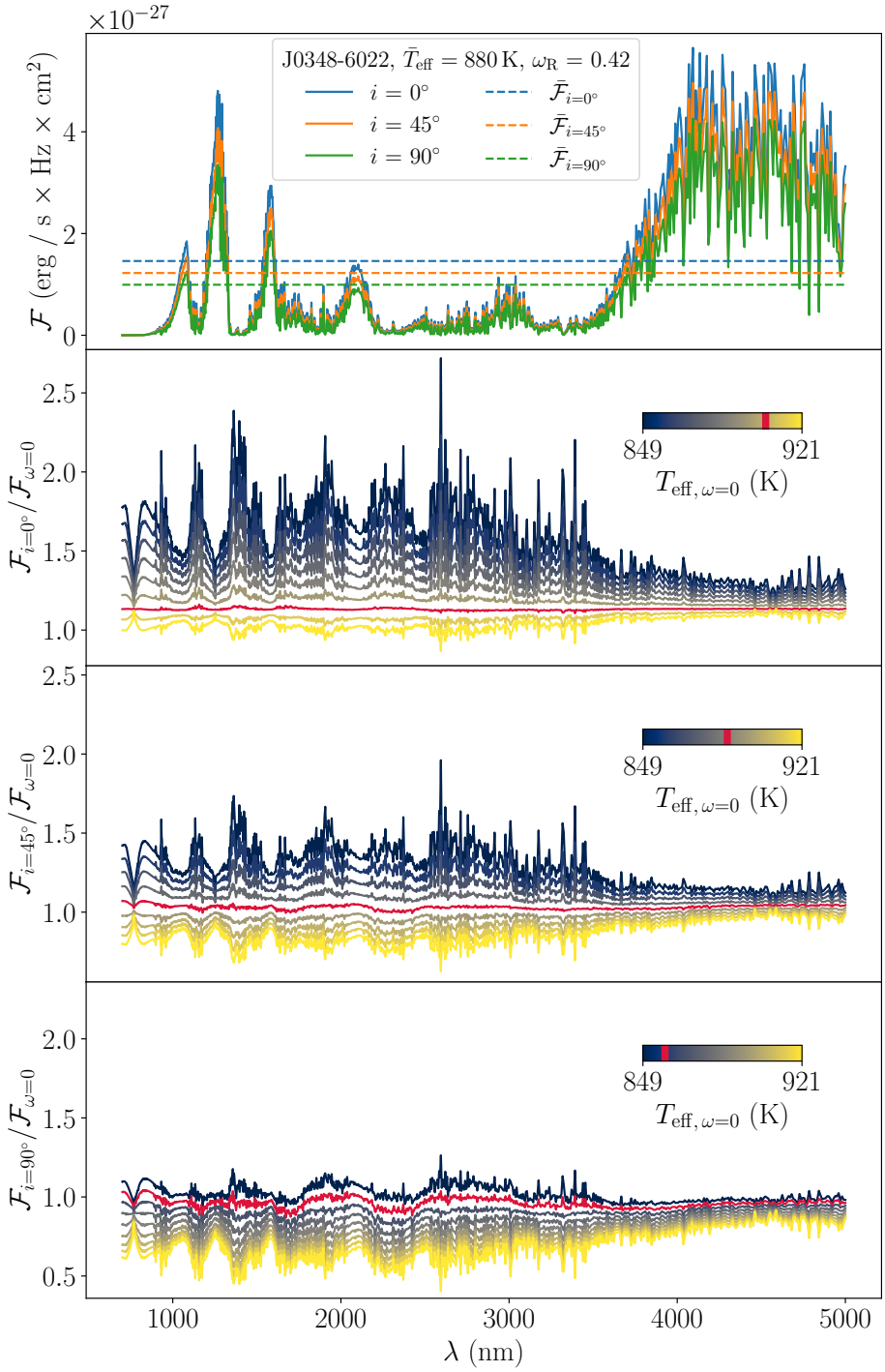

Figure 3.1 Top panel: synthetic spectra of a fast-rotating brown dwarf model. Lower panels: ratios of the rotating model's pole-on spectrum to spectra of nonrotating models with effective temperatures between the equatorial (top line) and the polar (bottom line) temperatures of the rotator. Crimson marks the nonrotating dwarf with the smallest relative deviation of spectrum shape from the spectrum shape of the rotator.

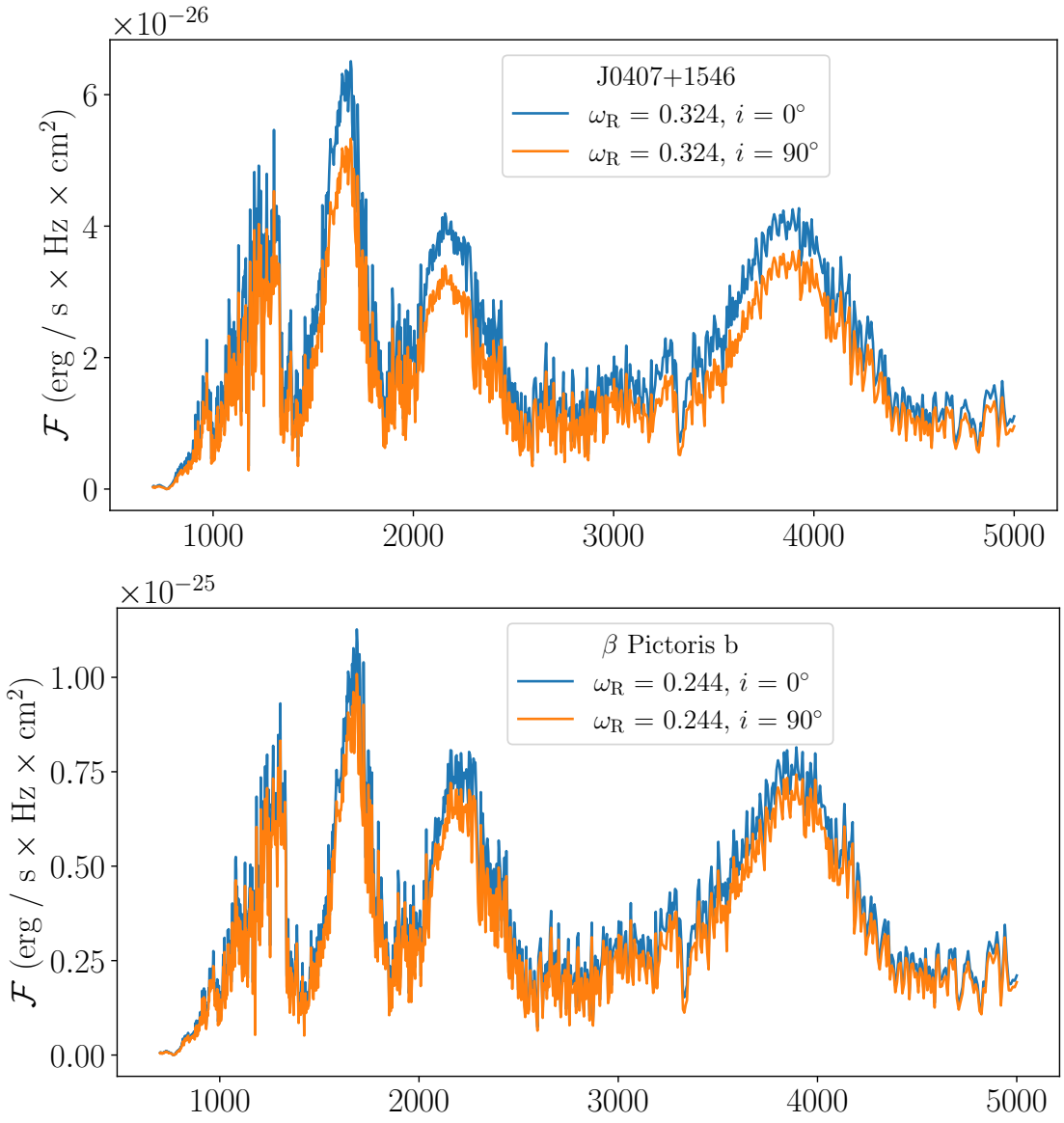

Figure 3.2 Upper panel: synthetic spectra of the L3.5-type fast-rotating brown dwarf from T21. Lower panel: synthetic spectra of β Pictoris b. Both panels present spectra at the two extreme inclinations.

of 1.5 between zero degree inclination (pole-on view, maximum flux) and ninety degree inclination (equator-on view, minimum flux). Figure 3.2 shows that the variation of spectral flux with inclination is less extreme for objects with lower rotational speed.

Next, we compare the synthetic observed rotator (Model 880) spectrum at every inclination to the library of associated nonrotating models (Section 3.3.1). We search the library for the best-matching spectrum by minimizing the root-mean-square deviation (RMSD) between the nonrotating model spectrum and a linear transformation of the observed spectrum that brings it closest to the non-rotator (Section 3.4.1).

It is apparent from Figure 3.1 that such a procedure leads to cooler inferred temperatures when the view of the rotator is closer to equator-on and hotter temperatures when it is towards pole-on. The inferred temperature is always in the range between the maximum, polar temperature of the dwarf and its minimum, equatorial temperature.

3.5.2 Rotation Detectability

In addition to spectral intensity and inferred temperature, inclination affects the detectability of rotation from spectral shape. The minimum RMSD from the previous section can serve as a quantitative measure of detectability, where higher minimum RMSD corresponds to higher detectability of rotation. At pole-on inclination, there is a nonrotating model with a spectrum that is very similar to the rotator's spectrum, both according to the minimum RMSD criterion (Figure 3.3) and according qualitative examination (see Figure 3.1). At the same time, Figures 3.1 and 3.3 show that the more equator-on inclinations produce spectra that are increasingly distinguishable from all non-rotator spectra. This effect is not intuitive in light of pure temperature range considerations, since both pole-on and equator-on objects display full pole-to-equator ranges. In order

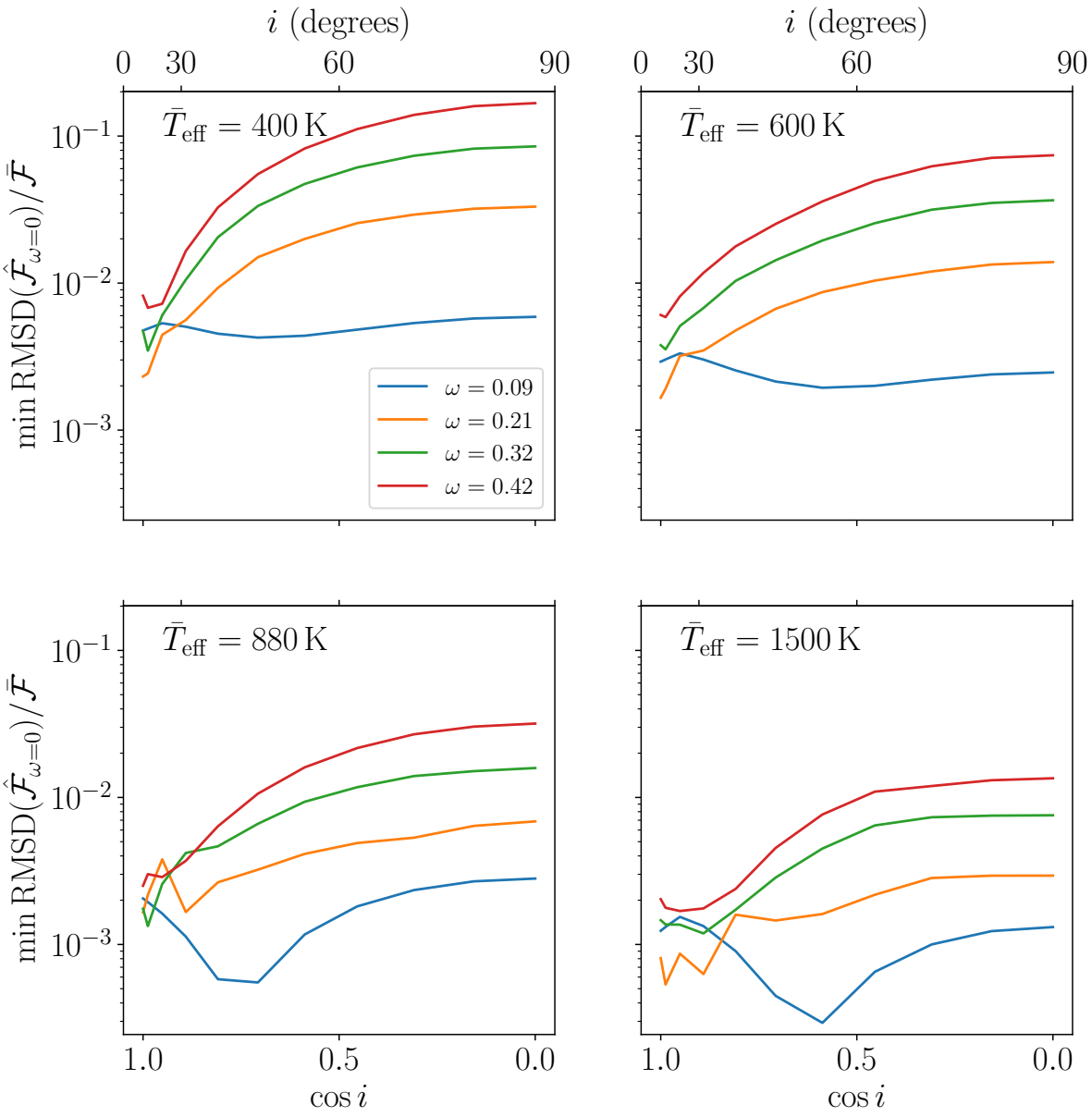

Figure 3.3 Normalized minimum root mean squared difference (RMSD) between a non-rotating dwarf's spectrum and the closest linear transformation of a rotator's spectrum, minimized across nonrotating models for a given rotator. This is a measure of the difference between the rotator's spectrum shape and the spectral shape of the best-matching non-rotator. The horizontal axis is the cosine of the rotational axis inclination. The different panels correspond to different average surface temperatures of the rotating dwarf. Comparison of the panels indicates that lower temperatures correspond to higher relative differences between the rotating and the nonrotating dwarf spectra, and thus, potentially, easier detectability of the rotational effects. Additionally, the panels suggest easier detectability at higher inclinations, in agreement with Figure 3.1.

to understand the effect, we have to additionally consider the geometry of rotational axis inclination. We suggest that increasing inclination might increase the detectability of rotation from spectrum shape due to the fact that the observed temperature profile of a pole-on dwarf has circular symmetry, much like the profile of a nonrotating object. This contrasts with non-polar inclinations, which are associated with solely axial symmetry (Espinosa Lara & Rieutord, 2011; Lipatov & Brandt, 2020b).

Figure 3.3 shows that the detectability of rotation from spectral shape grows not only with increasing inclination, but also with decreasing temperature. Specifically, this figure demonstrates that the minimum RMSD measure, normalized by the average integrated flux, decreases as one proceeds from cooler to hotter models. This may be related to the fact that cooler models show stronger departures from blackbody spectra, with corresponding increases in the sharpness of temperature-dependent spectral peaks and troughs.

The horizontal axis of Figure 3.3 is linear in the cosine of inclination, $\cos i$. This way, equal-space horizontal axis intervals correspond to equal probabilities of brown dwarfs under a spatially isotropic distribution of rotational axis directions, which corresponds to observed inclination probability density that is proportional to $\sin i$.

Figure 3.3 shows that the normalized RMSD reaches 2% for Model 880, suggesting that, if spectral precision and modeling fidelity reach this level, rotation may be detectable from spectra alone. The detectability is greatest for edge-on orientations, so that a substantial $v_{\mathrm{e}} \sin i$ would further establish the spectrum as that of a rapidly rotating

brown dwarf.

3.5.3 An Empirical Luminosity Correction

In this section we quantify the dependence of the inferred luminosity on inclination and rotation rate. To do this, we first create nine rotating models associated with Model 880, as described in Section 3.3.1. Their rotation rates $\omega_{\rm R}$ are equally spaced between 0.1 and 0.5 and their luminosities are all equal to that of Model 880. We calculate spectra at several inclinations for each model, and in each case produce the integrated flux $\mathcal{F}$. For every such spectrum, we find the nonrotating Model 880 variant with the maximally similar spectrum, according to the RMSD criterion. Let us say that this nonrotating model has integrated flux $\mathcal{F}_0$ and luminosity L_0. We then compute a product of luminosity and flux ratios on the left hand side of the following equation, which is a re-arrangement of Equation (3.16):

$$\frac{L}{L_0} \times \frac{\mathcal{F}_0}{\mathcal{F}} = \frac{L\,p}{4\pi r^2 \mathcal{F}}. \tag{3.19}$$

Figure 3.4 presents the anisotropy ratio in Equation (3.19) for four of the rotational speeds and all the inclinations that we use.

The lines in Figure 3.4 are cubic polynomials in the cosine of inclination $u = \cos i$, whose coefficients are given by quadratic fits to all nine rotational speeds $\omega_{\rm R}$. The

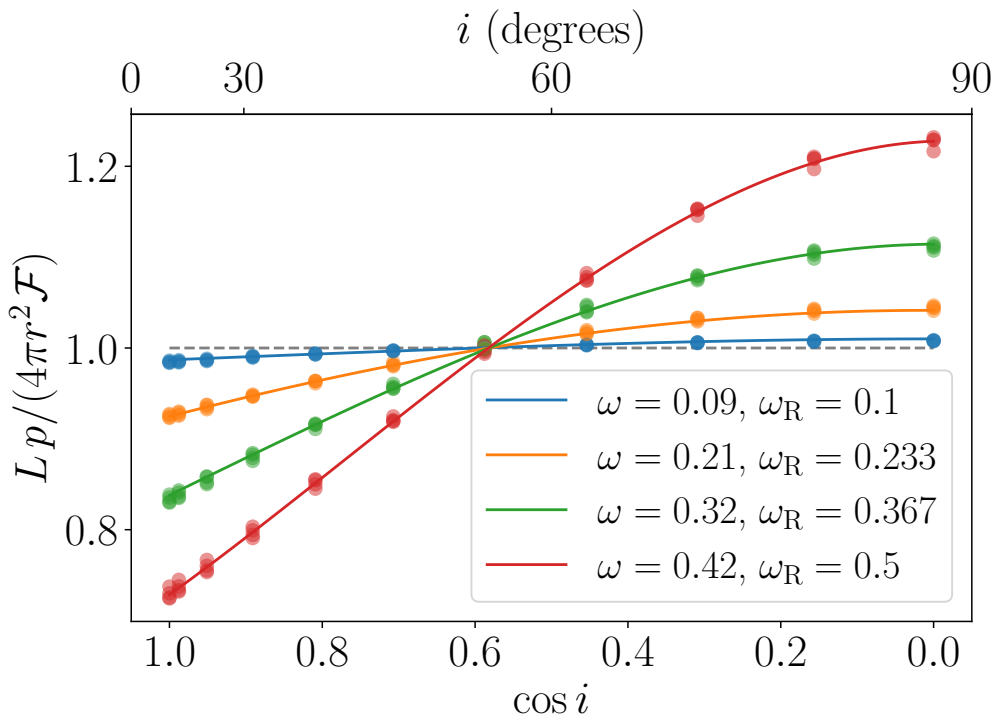

Figure 3.4 Luminosity correction factor due to the rotational anisotropy of bolometric flux. This factor is a ratio. The numerator of the ratio is $L/(4\pi r^2)$, the flux we would expect from the the dwarf's luminosity L and distance r if the flux were isotropic – the way it is for a nonrotating, spherically symmetric object. The denominator of the ratio is the observed bolometric flux $\mathcal{F}/p$ of the rotating dwarf. Here, $\mathcal{F}$ is the dwaf's flux between the wavelengths of 0.7 and 5.0 μm, whereas p is the proportion of a non-rotator's flux that is between these wavelengths. When $i = 55°$, the effect is non-existent. At this inclination, the bolometric flux is equal to the direction-averaged flux, no matter what the rotational speed is. The discrete markers are due to our synthetic spectra at $\bar{T}_{\rm eff} \in \{400, 600, 880, 1500\}$ K. The lines are cubic fits in $\cos i$ for $\bar{T}_{\rm eff} = 880$ K, with coefficients' quadratic dependence on $\omega_{\rm R}$ given in Section 3.5.3. The effect mainly depends on the rotational speed $\omega_{\rm R}$ and inclination i.

corresponding full coefficient matrix is

$$\mathbf{A} = \begin{bmatrix} 3.0791 & -0.9858 & 0.0807 \\ -4.5216 & 0.7383 & -0.0644 \\ -0.3774 & 0.1489 & -0.0113 \\ 1.1536 & -0.1482 & 1.0133 \end{bmatrix}. \tag{3.20}$$

Thus, the anisotropy ratio in Figure 3.4 at ω_{R} and $u = \cos i$ is given by

$$\begin{bmatrix} u^3 & u^2 & u & 1 \end{bmatrix} \mathbf{A} \begin{bmatrix} \omega_{\mathrm{R}}^2 \\ \omega_{\mathrm{R}} \\ 1 \end{bmatrix}. \tag{3.21}$$

The maximum difference between the fits and the discrete anisotropy ratios in Figure 3.4 is 0.01, i.e., the fitting formula can correct the luminosity with a maximum error of 1%. This maximal difference is found at $\omega_{\mathrm{R}} = 0.5$, $i = 90°$, and $\bar{T}_{\mathrm{eff}} = 1500\,\mathrm{K}$: a hot, very rapid rotator seen equator-on. The root-mean-square difference between the fit lines and all the discrete points in this figure is 1.2×10^{-5}, much less than 1%. The fact that these differences are small in comparison with the range of the anisotropy ratio confirms the proposition in Section 3.4.2 that the ratio is largely independent of object temperature and that it is mostly a function of ω_{R} and i.

Section 3.4.2 interprets the anisotropy ratio as a correction factor one must use in addition to the ratio of integrated fluxes in order to obtain a rotator's true luminosity

from the luminosity of a best-matching model. Figure 3.4 shows that this correction factor changes the luminosity by as much as 20% at extreme inclinations and rotational velocities that are typical of fastest-rotating dwarfs.

3.6 Discussion and Conclusions

Rotational period and projected equatorial velocity measurements for substellar objects frequently translate to significant fractions of critical rotation rates (Tannock et al., 2021; Chilcote et al., 2017; Snellen et al., 2014; Helled et al., 2009; Eislöffel & Scholz, 2007; Crossfield, 2014). The centrifugal expansion of a rotating object's equatorial regions will produce a significant variation in its surface temperature – relatively high values at the object's poles and relatively low values at its equator. As a result, we expect both the shape of a rotator's observed spectrum and its total observed flux to depend on the object's orientation, since a more equator-on view tends to show the cooler, dimmer equatorial regions as opposed to the hotter, brighter polar regions. Furthermore, we expect this effect to increase with greater rotational speed, since the latter leads to a greater temperature contrast between the equator and the poles.

In this work, we explore the dependence of a substellar object's observables on its rotational speed and rotational axis inclination. We also place this dependence in the context of a comparison with the expected observables of nonrotating models. In order to accomplish these tasks, we use `PICASO` (a Planetary Intensity Code for Atmospheric Spectroscopy Observations) to generate synthetic spectra and process them with `PARS`

(Paint the Atmospheres of Rotating Stars), which produces spectra of rotating, self-gravitating, gaseous masses at different rotational speeds and inclinations (LB20).

An initial analysis shows that the specific flux of a typical fast-rotating brown dwarf can differ by as much as a factor of 1.5 between the two extreme inclinations in spectral regions with appreciable intensity (see the upper panel of Figure 3.1, for example).

Next, we ask whether the shape of a rotationally deformed substellar object's spectrum differs significantly from the spectra of similar objects that are nonrotating and therefore spherically symmetric. In other words, we wish to know whether one can infer rotation from the shape of an object's spectrum alone. To this end, we use `PARS` to calculate synthetic spectra of a typical quickly rotating brown dwarf at different rotational axis inclinations, as well as spectra of nonrotating objects that are otherwise similar to the rotator. We find that, when we observe the rotator pole-on, its spectrum is virtually indistinguishable from that of another, nonrotating object at a certain temperature between the rotator's equatorial and polar values. On the other hand, as the rotator approaches an equator-on view, its spectrum becomes increasingly different from that of any nonrotating object. We demonstrate this effect in Figure 3.1 and hypothesize that it results from the fact that a pole-on view has circular symmetry, much like the view of a nonrotating object and unlike the rotator's equator-on view.

To quantify the difference between the spectral shapes of a rotator and a non-rotator, we compute the root-mean-square difference between the non-rotator's specific flux at different wavelengths and the closest linear transformation of the rotator's flux. We

minimize this quantity across non-rotators and divide it by the rotator's mean flux, to obtain a dimensionless measure of rotation's detectability from spectral shape. We compute this minimized RMSD measure across different average rotator temperatures, rotational velocities, and inclinations. Figure 3.3 shows that, in accordance with the qualitative results of Figure 3.1, detectability of rotation from spectral shape increases when the rotational speed is greater and the view is closer to equator-on. In addition, Figure 3.3 indicates that detectability increases when the temperature of the rotating dwarf decreases.

A nonrotating model is spherically symmetric. Thus, its observed flux does not depend on the spatial direction to the observer. On the other hand, a rotator's flux is anisotropic – it depends on the observer's direction or, equivalently, on the inclination of the rotational axis with respect to the observer's view. Thus, although the luminosity of a nonrotating object can be inferred from its observed flux, a rotator's luminosity estimate requires an additional correction due to the anisotropy effect. Without this correction, the luminosity of an equator-on object is under-estimated, while that of a pole-on object is over-estimated. We calculate this correction for a variety of rotating models and plot it in Figure 3.4. We find that it is relatively insensitive to average object temperature. On the other hand, the correction depends strongly on rotational speed and inclination. It reaches its extreme values at the two extreme inclinations, where it adjusts luminosity estimates by as much as $\sim$20% near the rotational speeds of fastest-rotating observed dwarfs. Section 3.5.3 provides an approximation of the luminosity correction as

a function of rotational speed and inclination.

Data Availability

The brown dwarf atmosphere intensity grid in this chapter, produced by the `PICASO` radiative transfer code and based on Sonora model atmospheres, is available on Zenodo, at https://doi.org/10.5281/zenodo.6842801. The version of `PARS` that took this intensity grid as input and produced all the figures in the chapter is also on Zenodo, at https://doi.org/10.5281/zenodo.6842745.

Chapter 4

Rotational Variation and Age Spread in a Globular Cluster

In this chapter, we develop a methodology that connects the evolution of individual rotating stars with the distributions of stellar ages and rotational speeds in clusters. Both the evolution of stars and their distributions in clusters are associated with considerable uncertainty. Our method aims to establish the relationship between the two, so that aspects of evolutionary theory that are known with certainty can provide information about cluster parameters and so that known cluster parameters can tell us something about the evolutionary theory.

Our case study is globular cluster NGC 1846 in the Large Magellanic Cloud with magnitude and rotational velocity data on more than a thousand stars in the extended main sequence turn-off (eMSTO). We analyse these data in the light of `MIST` stellar

evolution models that include rotation. One of our main conclusions is that rotational variation allows for an age spread in NGC 1846 that is significantly narrower than the spread in the absence of stellar rotation. Furthermore, our detailed analysis allows us to suggest specific modifications to the `MIST` models that would likely improve the fit between the models, the cluster data, and independent estimates of cluster parameters. The modifications that we suggest include a reduction in rotational braking and greater increases in longevity with rotation.

The `PARS` software that we introduce in the previous chapters plays a key role in the present analysis, since it provides a precise mapping between the present-day parameters of stellar models and the models' observable magnitudes and rotational speeds.

The contents of this chapter have been published in Lipatov et al. (2022), under the title "Rotational Variation Allows for Narrow Age Spread in the Extended Main Sequence Turnoff of Massive Cluster NGC 1846".

4.1 Data

We base our analysis on recent spectroscopic $v_{\rm e} \sin i$ measurements of individual stars in the central 1 arcmin $\times$ 1 arcmin of NGC 1846, collected by Kamann et al. (2020, henceforth K20) with the Multi Unit Spectroscopic Explorer (`MUSE`, Bacon et al., 2010) on the Very Large Telescope. Here, $v_{\rm e}$ is the equatorial velocity of a star and i is the inclination of its rotational axis with respect to the plane of the sky, so that $v \equiv v_{\rm e} \sin i$ is the projected equatorial velocity. K20 estimate $v_{\rm e} \sin i$ from transition line broadening via

full-spectrum fitting and augment these measurements with previously collected multi-band HST (Hubble Space Telescope) photometry of the same stars (Martocchia et al., 2018). The photometric magnitudes correspond to three filters on the Wide Field Channel of HST's Advanced Camera for Surveys: $m_{435} \equiv m_{\mathrm{F435W}}$, $m_{555} \equiv m_{\mathrm{F555W}}$, and $m_{814} \equiv m_{\mathrm{F814W}}$. The MUSE data show significant variation in $v_{\mathrm{e}} \sin i$ across the MSTO, indicating that the stars in this area of the CMD have significantly variable rotation speeds and/or inclinations.

Inference of rotational and age distributions in clusters is sensitive to the modeling of processes relevant to the evolution of stars, in ways that potentially differ between the stages of a star's life and between stars of different masses. Thus, in order to better understand the meaning of our results, we restrict ourselves to a particular portion of the NGC 1846 data set and a particular range of stellar evolution models. Specifically, we work only with the stars observed in the MSTO area of the CMD (see Figure 4 in K20) and interpret them solely in terms of 1 to 2 $M_{\odot}$ main-sequence stellar models. Even when the inference is subject to these restrictions, the data set remains large, while the evolutionary models produce predictions that are sufficiently intricate to warrant taking into account the exact uncertainty on each measurement. To accomplish the latter for the entire data set, we find it advantageous to establish minimum possible errors on measurements, compute corresponding minimum-error theoretical probability distributions, then broaden these distributions as necessary for each individual measurement. Our data selection and error assignment, further described in the rest of this section, are designed

in view of the above-mentioned considerations.

We make use of the $n = 2353$ stars in K20's data set that fall in our region of interest (ROI), which satisfies $m \equiv m_{555} \in [19.5, 22.0]$, $c \equiv m_{435} - m_{814} \in [0.4, 1.0]$, and $v \in [0, \infty]$. We refer to a point in the 3-dimensional observable space as $\boldsymbol{x} \equiv (m, c, v)$. Since neither of the two filters that produce c is the filter that produces m, we assume zero correlation between the errors in these two observables for a given star. We also assume that errors in broadband filter magnitudes do not correlate with errors in the broadening of individual spectral lines, so that the errors in m and c do not correlate with the error in v. The rotational measurement v is positive, zero and missing for $n_{\rm p} = 1237$, $n_{\rm z} = 74$ and $n_{\rm m} = 1042$ of these stars, respectively. Every m and c measurement in the data set is associated with its own error value, which we interpret as the standard deviation of the corresponding error distribution. Furthermore, every positive v measurement in the data set is associated with an upper and a lower error value. The average of these latter two values becomes the standard deviation of the corresponding v measurement error distribution. This averaging procedure does not affect inference at $v > 100\,\mathrm{km/s}$, where the upper and lower errors are equal. We choose to retain the averaging procedure at lower v, for the sake of computational speed and simplicity. We further assume that the error distributions are Gaussian and impose a lower limit of $\sigma_m = 0.01$ on the standard deviations of these distributions for magnitudes. This makes the error distributions for color measurements Gaussian as well, with a lower limit on standard deviations $\sigma_c = \sigma_m\sqrt{2} = 0.014$. Our approximation of non-Gaussian error distributions

for low v measurements as Gaussian may introduce offsets to our cluster parameter estimates. On the other hand, we expect these offsets to be significantly lower than the offsets due to uncertainties in evolutionary models. The true error distributions are, in any case, likely to be far more complicated than two half-Gaussians with a discontinuity where they meet.

Our lower limit on the uncertainty of v measurements is $\sigma_v = 10\,\mathrm{km\,s^{-1}}$, which is on the order of the uncertainty in $v_\mathrm{e} \sin i$ at a given line broadening σ_LOS in Figure A1 of K20. Although we are not explicitly given an error on the $v = 0$ measurements, we set it equal to $50\,\mathrm{km\,s^{-1}}$, based on an approximate extrapolation of the v measurement standard deviations down to $v = 0$. We collectively refer to the minimum errors on the observables as $\boldsymbol{\sigma_x} \equiv (\sigma_m, \sigma_c, \sigma_v)$. Each data point is composed of an observed star's $\boldsymbol{x}$ and $\boldsymbol{\sigma_x}$: $\boldsymbol{x_p} \equiv (m_p, c_p, v_p)$ and $\boldsymbol{\sigma_{xp}} \equiv (\sigma_{mp}, \sigma_{cp}, \sigma_{vp})$, where subscript $p \in [1, n]$ is data point index. A missing rotational measurement corresponds to $\sigma_{vp} = \infty$.

4.2 Stellar model

In this section, we describe the procedure that yields magnitude, color and $v_\mathrm{e} \sin i$ for a stellar model, given its independent parameters – initial mass, initial rotation rate, inclination of the rotational axis, age, and initial mass of a binary companion (if present).

4.2.1 Evolution

We model the evolution of stars according to version 1.0 of the `MIST` library , which is based on version r7503 of the `MESA` computer code (Modules for Experiments in Stellar Astrophysics: Paxton et al., 2011, 2013, 2015, 2019). `MESA` models rotation by using pressure as the radial coordinate. It does not assume spherical symmetry, but rather that certain physical quantities are constant along isobars and that energy transport is perpendicular to the local effective gravity.

At a given age, `MIST` provides Equivalent Evolutionary Phase (EEP), mass M, surface angular speed Ω, dimensionless angular speed $\omega_{\rm M}$, luminosity L, Eddington ratio $L/L_{\rm Edd}$, and radius $R_{\rm M}$. Here, $R_{\rm M}$ is the radius of a sphere that encloses the star's volume V (Endal & Sofia, 1976; Paxton et al., 2019), so that

$$V = \frac{4\pi}{3} R_{\rm M}^3. \tag{4.1}$$

Furthermore, $\omega_{\rm M} \equiv \Omega/\Omega_{\rm crit}$, where $\Omega_{\rm crit}$ is defined soon after Equation (26) in Paxton et al. (2013):

$$\Omega_{\rm crit} \equiv \sqrt{\left(1 - \frac{L}{L_{\rm Edd}}\right) \frac{GM}{R_{\rm M}^3}}. \tag{4.2}$$

We only consider main sequence `MIST` models, with EEP $\in [202, 454]$. We model stars at other EEPs as part of a background distribution, while choosing our region of the CMD to exclude most of these post-main sequence stars. We estimate that only

about 1% of the stars that remain in our ROI on the CMD (i.e., about 20 stars) are post-main sequence stars, given the amount of time that `MIST` models spend on the subgiant branch before crossing the red edge of our ROI at $m_{435} - m_{814} = 1$. Our background distribution also subsumes other types of stars, such as blue stragglers, that are not modeled by the `MIST` library. Upon visual inspection of the turn-off, we estimate that $\lesssim 1\%$ of our observed stars are likely to be blue stragglers. These would have to be modeled via binary evolution, which is beyond the scope of this paper.

Along with age t, the models' independent parameters are initial mass, initial angular speed $\omega_{\rm Mi}$, and metallicity $[{\rm M/H}]_{\rm M}$. Initial mass is designated by $M_{\rm i}$ for a primary in a star system and by $M_{\rm Ci}$ for a secondary companion. Here and elsewhere in the chapter, subscripts M and i stand for "`MIST`" and "initial", respectively. Furthermore,

$$[{\rm M/H}]_{\rm M} = \log \frac{Z}{X} - \log \frac{Z_{\odot,{\rm M}}}{X_\odot}, \tag{4.3}$$

where Z and X are the respective metal and hydrogen mass fractions of the star, $X_\odot$ is the protosolar hydrogen mass fraction, and $Z_{\odot,{\rm M}} = 0.0142$ is an estimate of the protosolar metal mass fraction (pp. 2-3 in Choi et al., 2016; Asplund et al., 2009). In Equation (4.3) and the rest of this work, log designates logarithm with base ten.

`MIST` has solar-scaled abundance ratios, so that its metallicity is equivalent to relative iron abundance, i.e., $[{\rm M/H}]_{\rm M} \equiv [{\rm Fe/H}]_{\rm M}$. There is some evidence that the LMC and Milky Way (i.e., solar) abundance patterns differ. In particular, the LMC may have relatively low Mg to Fe and O to Fe ratios (Pompéia et al., 2008; Van der Swaelmen

et al., 2013; Rolleston et al., 2002). Future work may provide model libraries with LMC-scaled abundances. We keep metallicity $[\mathrm{M/H}]_\mathrm{M}$ constant at -0.45, a value that is based on isochrone fits in K20, so that the models start off parametrized by $\{M_\mathrm{i}, \omega_\mathrm{Mi}, t\}$.

Traditionally, an isochrone is a line on the CMD that corresponds to a set of models at constant chemical composition and age, parameterized by initial mass. Here, we define a generalized isochrone as the cloud of points in observable space that corresponds to the full range of our independent model parameters—mass, rotation, and orientation—restricted to a particular age t and composition $[\mathrm{M/H}]_\mathrm{M}$. In this context, equivalent evolutionary phase (EEP) can parametrize isochrones instead of initial mass (Dotter, 2016). For a point on an isochrone with some initial mass M_i and initial rotation rate ω_Mi that translate to some EEP, the point closest in observable space on a neighboring isochrone is approximately the one with the same EEP, not the one with the same mass. Accordingly, when we intepolate between isochrones, i.e., in age t, we fix EEP and ω_Mi instead of M_i and ω_Mi. This recipe could have been complicated by the fact that several values of M_i can correspond to the same EEP at a given combination of ω_Mi and t. However, none of the models we utilize exhibit this behavior.

Here and elsewhere in this chapter, interpolation is linear unless stated otherwise. Furthermore, all interpolation and integration that involves t, luminosity L, and Eddington ratio L/L_Edd uses the logarithms of these variables.

4.2.2 Rotational Speed Conversion

The radius used to compute the dimensionless rotation speed $\omega_{\rm M}$ in `MIST` is a volume-averaged quantity. Because a rapidly rotating star expands in its equatorial regions, $\omega_{\rm M}$ of unity does not correspond to the critical angular speed where the stellar equator becomes unbound.

Accordingly, in addition to $\omega_{\rm M}$ and average radius $R_{\rm M}$, we consider dimensionless rotational speed $\omega \equiv \Omega/\Omega_{\rm K} \in [0, 1]$ and equatorial radius $R_{\rm e}$. Here, $\Omega_{\rm K}$ is the Keplerian limit on Ω, i.e., the rotational speed at which a star with mass M and equatorial radius $R_{\rm e}$ would start to break up due to the centrifugal effect. Under the assumption that all mass is at the star's center – i.e., the Roche model of mass distribution,

$$\Omega_{\rm K} = \sqrt{\frac{GM}{R_{\rm e}^3}}. \tag{4.4}$$

The Roche model admits an analytic expression for a normalized radial cylindrical coordinate of the stellar surface $\tilde{r}$ in terms of a normalized vertical cylindrical coordinate $\tilde{z}$ (Lipatov & Brandt, 2020b, henceforth LB20). We now use that expression to derive a conversion between $\omega_{\rm M}$ and ω under this model of mass distribution. To start, we define a star's dimensionless volume as

$$\tilde{V} \equiv \frac{3}{4\pi}\frac{V}{R_{\rm e}^3} \tag{4.5}$$

and express it in terms of an integral in dimensionless cylindrical coordinates:

$$\tilde{V}(\omega) = \frac{3}{4\pi}\frac{2}{f}\int_0^1 \pi\, \tilde{r}(\tilde{z})^2\, d\tilde{z}, \tag{4.6}$$

where $\tilde{r} \equiv r/R_{\rm e}$, $\tilde{z} \equiv z/R_{\rm p}$, $R_{\rm p}$ is the polar radius, and $f \equiv R_{\rm e}/R_{\rm p}$, as defined in LB20. Here, f and $\tilde{r}(\tilde{z})$, and therefore $\tilde{V}$, are functions of ω. We compute $\tilde{V}$ on a fine grid of ω values using Equation (4.6), the expression for $\tilde{r}(\tilde{z})$ in LB20, and the composite trapezoidal rule. We then perform cubic interpolation to obtain $\tilde{V}(\omega)$. Dividing Equation (4.1) by $R_{\rm e}^3$, we also have

$$\tilde{V} = \left(\frac{R_{\rm M}}{R_{\rm e}}\right)^3, \tag{4.7}$$

so that

$$R_{\rm e} = \frac{R_{\rm M}}{\sqrt[3]{\tilde{V}}}. \tag{4.8}$$

The definitions of ω and $\omega_{\rm M}$, in addition to Equations (4.2), (4.4), and (4.7), yield

$$\tilde{V}(\omega) \times \omega^2 = \omega_{\rm M}^2\left(1 - \frac{L}{L_{\rm Edd}}\right) \equiv \omega_{\rm M}'^2. \tag{4.9}$$

At $\omega = 0$, rotation doesn't deform the star, so that $R_{\rm M}$, defined in Equation (4.1), is equal to the equatorial radius $R_{\rm e}$. As ω increases, rotational deformation causes $R_{\rm M}/R_{\rm e}$ to decrease. Thus, according to Equations (4.7) and (4.9), $\omega_{\rm M}' = 0$ when $\omega = 0$ and

$\omega'_{\rm M}/\omega$ decreases from one as ω increases from zero. When ω reaches one, so that Ω is at the Keplerian limit, $\omega'_{\rm M} = 0.7356$, which implies a shape so non-spherical that $R_{\rm M}/R_{\rm e} = (0.7356)^{2/3} = 0.8149$. We solve Equation (4.9) numerically to obtain $\omega(\omega'_{\rm M})$. Figure 4.1 presents the result, a monotonically increasing function. We use it to calculate ω from $\omega_{\rm M}$ and $L/L_{\rm Edd}$.

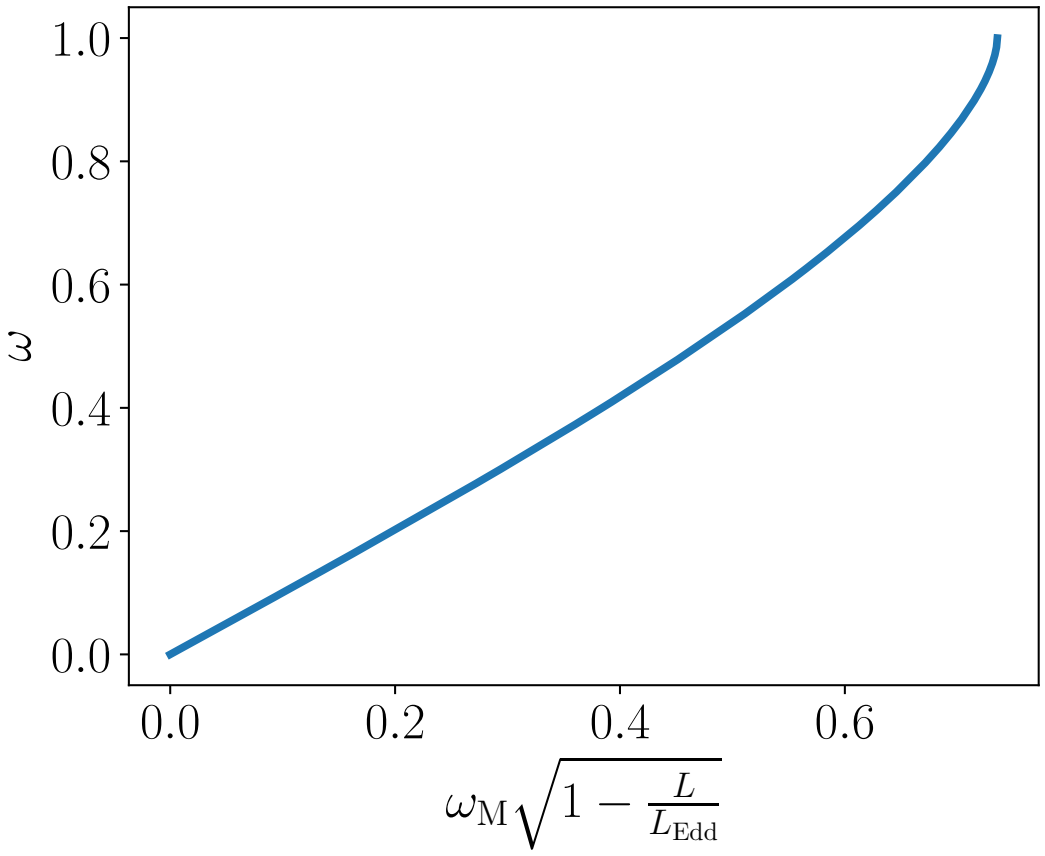

Figure 4.1 Relationship between the proportion of Keplerian rotational limit ω and a quantity related to the `MIST` dimensionless rotational velocity $\omega_{\rm M}$.

`MIST` does not provide the initial value of Eddington ratio $L/L_{\rm Edd}$ for all of its models. However, it does inform that a non-rotating model with initial mass $M_{\rm i} = 2M_{\odot}$ has $L/L_{\rm Edd} = 0.017$ at zero age main sequence (ZAMS). All `MIST` models we use are less

massive and most have significantly smaller $L/L_{\rm Edd}$. Therefore, in the case of initial rotational speeds, we set $L/L_{\rm Edd} = 0$ and solve

$$\tilde{V}(\omega_{\rm i}) \times \omega_{\rm i}^2 = \omega_{\rm Mi}^2 \tag{4.10}$$

to find $\omega_{\rm i}$, the initial value of ω. This corresponds to the dependence in Figure 4.1, with $\omega_{\rm Mi}$ and $\omega_{\rm i}$ re-labelling the horizontal and vertical axes, respectively. The largest $\omega_{\rm Mi}$ below the above-mentioned Keplerian limit of 0.7356 is 0.7 in the `MIST` models. Setting $\omega_{\rm Mi}$ to 0.7 in Equation (4.10) yields $\omega_{\rm i} = 0.8590$. This is the maximum $\omega_{\rm i}$ in the present analysis, since we do not extrapolate to higher values of this parameter. Some of the stars in our data set may possess $\omega_{\rm i} > 0.8590$. In Section 4.6, we discuss the implications of the rotational speed limit in our analysis on the quantitative results and suggest the limit's increase as an important future modification to the `MIST` library.

4.2.3 Synthetic Magnitudes

In Sections 4.2.1 and 4.2.2, we mention present-day parameters that determine a star's magnitude – its mass M, luminosity L, average radius $R_{\rm M}$, and `MIST`'s dimensionless rotational velocity $\omega_{\rm M}$. We also describe a procedure that converts $R_{\rm M}$ and $\omega_{\rm M}$ to equatorial radius $R_{\rm e}$ and another kind of dimensionless rotational velocity ω. In this section, we describe a procedure that yields stellar magnitudes from M, L, $R_{\rm e}$, ω, and rotational axis inclination i.

Model Parameters for Magnitude Calculation

LB20 introduced `PARS` - Paint the Atmospheres of Rotating Stars, a program that computes theoretical magnitudes of a rotating star in a given telescope filter. The program is based on a model of internal energy flux due to Espinosa Lara & Rieutord (2011) and `ATLAS9`, a library of stellar atmosphere models due to Castelli & Kurucz (2004). Our present work necessitates the computation of magnitudes for many stellar models, so that separately employing `PARS` to compute the magnitude of each would be too slow. Accordingly we aim to interpolate magnitude on a grid of `PARS` models instead.

`PARS`'s input stellar parameters are L, M, $R_{\rm e}$, ω, i, and metallicity $[\mathrm{M/H}]_{\rm P}$. Here,

$$[\mathrm{M/H}]_{\rm P} = \log \frac{Z}{X} - \log \frac{Z_{\odot,\rm P}}{X_\odot}, \tag{4.11}$$

where Z, X and $X_\odot$ are defined as in Equation (4.3), $Z_{\odot,\rm P} = 0.01886$ is an estimate of the protosolar metal mass fraction (Anders & Grevesse, 1989), and the available $[\mathrm{M/H}]_{\rm P}$ values are the same as in `ATLAS9` (Castelli & Kurucz, 2004). Subtracting Equation (4.3) from Equation (4.11), we get

$$\begin{aligned} [\mathrm{M/H}]_{\rm P} - [\mathrm{M/H}]_{\rm M} &= \log Z_{\odot,\rm M} - \log Z_{\odot,\rm P} \\ &= -0.1233. \end{aligned} \tag{4.12}$$

Mapping between `MIST` and `PARS` models according to Equation (4.12) ensures that metal mass fraction Z remains the same, despite the differences in the protosolar mass fraction

between the two model libraries.

In order to speed up interpolation on the PARS grid, we wish to decrease its dimensionality. Towards this end, we derive parameters γ and τ, which are similar to surface gravity and effective temperature, respectively. We will show that one can interpolate in γ and τ at fixed equatorial radius $R_{\rm e} = R_\odot$ instead of interpolating in M, L, and $R_{\rm e}$, then add a function of $R_{\rm e}/R_\odot$ to the resulting magnitudes. Parameter γ is the logarithm of the gravitational acceleration at the equator in cgs units,

$$\gamma \equiv \log\left(\frac{GM}{R_{\rm e}^2}\Big/\,{\rm cm\,s^{-2}}\right). \tag{4.13}$$

Parameter τ is the effective temperature of a spherically symmetric star with luminosity L and radius $R_{\rm e}$,

$$\tau \equiv \left(\frac{L}{4\pi\sigma_{\rm SB}R_{\rm e}^2}\right)^{1/4}. \tag{4.14}$$

Quantities G and $\sigma_{\rm SB}$ are the gravitational and Stefan-Boltzmann constants, respectively. Here and in the rest of this work, logarithms of physical quantities are base-ten, while those of likelihood and probability functions are natural, unless stated otherwise.

PARS adds up luminous power over the set of infinitesimal patches that make up the visible stellar surface, taking into account the viewing angle of each patch. Stars of different size but constant ω and orientation look the same apart from an overall scale–their angular extent on the sky. This allows us to define a normalized ω-surface, which

has unit equatorial radius and depends solely on dimensionless rotational velocity ω. Consequently, we can write down the power emanating from a star at a given wavelength as a product of $R_{\rm e}^2$ and an integral of the star's intensity over the patches on such a normalized surface (see Equation 18 in LB20).

In addition to ω and i, γ and τ determine the above-mentioned flux from a normalized surface, as follows. The intensity of each surface patch depends on its viewing angle, its temperature T, and its value of g – the combined gravitational and centrifugal acceleration. Equation (36) in LB20 writes g as a product of 10^{γ} and a function of the patch's location on the ω-surface. On the other hand, Equation (31) in Espinosa Lara & Rieutord (2011) expresses T as a product of τ and another function of the ω-surface location. Thus, luminous power can be computed from γ, τ, ω and i, up to a factor of $R_{\rm e}^2$.

Consequently, to compute the magnitude of a stellar model from `PARS`'s input parameters, we calculate γ and τ from Equations (4.13) and (4.14), interpolate magnitude on the `PARS` grid, and subtract $5 \times \log R_{\rm e}/R_{\odot}$, which is equivalent to multiplying luminous power by $(R_{\rm e}/R_{\odot})^2$.

Model Grid for Magnitude Calculation

We compute the `PARS` grid—multi-band synthetic photometry on a grid of τ, ω, i and γ—for $[{\rm M/H}]_{\rm M} = -0.45$, extinction parameter $A_{\rm V} = 0.263$, distance modulus $\mu = 18.45$, and $R_{\rm e} = R_{\odot}$. Our value for μ is the same as in K20 and the value for $A_{\rm V}$ is based on isochrone fits in K20. We do not include the uncertainties for $[{\rm M/H}]_{\rm M}$, $A_{\rm V}$, or μ in our

analysis, since the influence of these uncertainties on our results should be significantly less than that of the uncertainties in the stellar evolution model (see Section 4.6). The extinction curve is from Fitzpatrick (1999), with $R_V = 3.1$. The magnitudes we calculate are m_{435}, m_{555}, and m_{814}. Here, we first convert $[\mathrm{M/H}]_\mathrm{M}$ to $[\mathrm{M/H}]_\mathrm{P}$ via Equation (4.12), then interpolate between the available values of $[\mathrm{M/H}]_\mathrm{P}$.

The range of the τ and γ portion of the grid is the same as that of temperature and gravity in `ATLAS9` plane-parallel atmosphere models (Table 1 of Castelli & Kurucz, 2004): $3{,}500\,\mathrm{K} \leq \tau \leq 50{,}000\,\mathrm{K}$ and $0.0 \leq \gamma \leq 5.0$. The two grids have similar model coverage since, for example, the surface of a star with parameter τ has temperatures in the neighborhood of τ. The spacing between adjacent τ values is 16 K below 4500 K, 31 K between 4500 K and 6200 K, and 63 K above 6200 K. The spacing between adjacent γ values is 0.5. The ω grid extends from 0 to 0.95, with a spacing of 0.05. The i grid has 20 values, equally spaced between 0 and $\pi/2$. Overall, there are close to 1 million models on the τ, ω, i and γ grid.

To assess the accuracy of interpolations within our model grid, we take each `PARS` grid parameter and calculate the magnitude differences between any two adjacent values of that parameter, with all other parameters fixed. Most of these differences are only a few minimum magnitude errors σ_m, or a few hundredths of a magnitude, as demonstrated in Figure 4.2. Assuming that the magnitude function does not deviate significantly from linearity on the scale of a few σ_m, interpolation on the `PARS` grid should be very accurate.

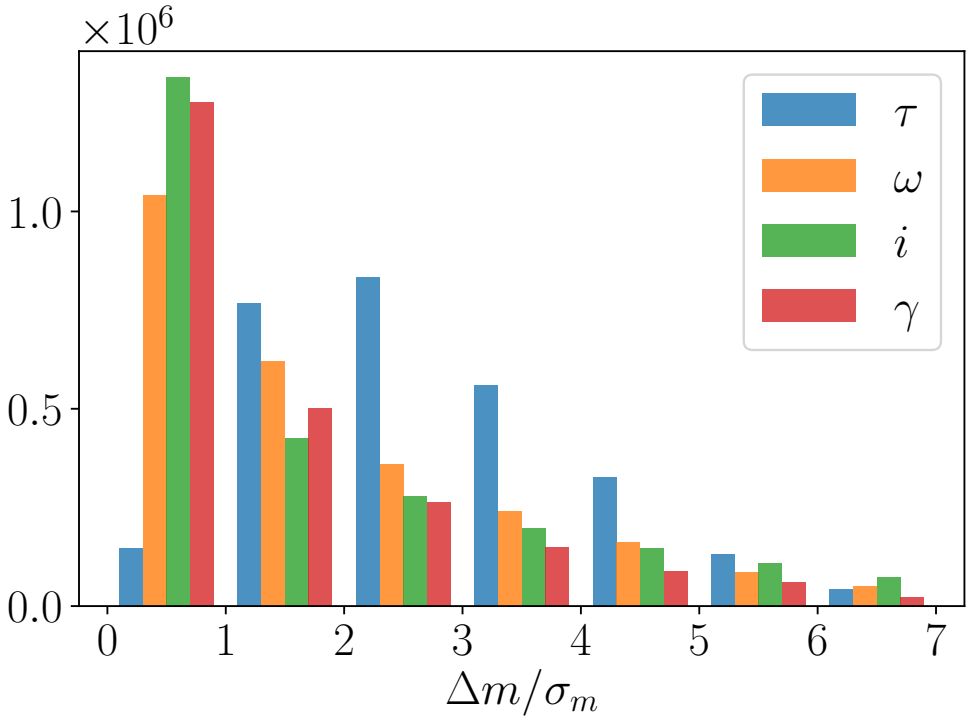

Figure 4.2 Histograms of the magnitude differences in units of minimum error (σ_m = 0.01 mag) between adjacent models on the entire `PARS` grid in Section 4.2.3. Differences are taken along each of the four grid dimensions, indicated in the legend. Most differences are only a few σ_m. Assuming that the magnitude function does not deviate significantly from linearity on this scale, interpolation on the `PARS` grid should be very accurate.

4.2.4 Calculation of Observables

The previous section describes the calculation of magnitudes for individual stars. We also allow for the possibility that a star in our data set is actually an unresolved, non-interacting binary system, consisting of a rotating primary and a non-rotating companion that do not eclipse each other. Allowing for the rotation of the secondary would increase the dimensionality of model space from 5 to 7. At the same time, this change would only have an effect for stars whose companions lie above the Kraft break, around 20%

of binaries, assuming a turnoff mass of $\approx 1.6 M_\odot$ and a flat companion mass function. The effects of rotation would further be subdominant to those of binarity even for these stars. The binary fraction of the cluster is estimated to be $\approx 6\%$ from independent measurements. With $\sim$1000 stars on the turnoff above the Kraft break, we therefore expect to be neglecting a subdominant effect for $\sim$10 stars (comparable to the effect of our neglect of the subgiant branch).

We assume that the companion's initial mass $M_{\rm Ci}$ does not exceed the primary's initial mass $M_{\rm i}$, so that the binary mass ratio $r \equiv M_{\rm Ci}/M_{\rm i} \in [0, 1]$. We combine the magnitude of a primary $m_{\rm p}$ with that of its companion $m_{\rm c}$ as follows:

$$m = -2.5 \log \left(10^{-m_{\rm p}/2.5} + 10^{-m_{\rm c}/2.5} \right). \tag{4.15}$$

We now define the initial stellar parameters $\boldsymbol{\theta'} \equiv (M_{\rm i}, r, \omega_{\rm i}, i)$, as well as the full set of parameters $\boldsymbol{\theta} \equiv (M_{\rm i}, r, \omega_{\rm i}, i, t)$, where $\omega_{\rm i}$ is the initial dimensionless rotation rate of the primary and i is the primary's inclination. We wish to obtain the observables on grids of $\boldsymbol{\theta}$. Towards this end, we first interpolate dependent model parameters between original `MIST` ages at constant initial rotation rate $\omega_{\rm Mi}$ and constant equivalent evolutionary phase, EEP (see the latter portions of Section 4.2.1). The rest of the procedure, outlined in Figure 4.3, happens at constant age. It starts with the conversion of $\omega_{\rm Mi}$ to $\omega_{\rm i}$ (see Section 4.2.2), proceeds to the interpolation of model parameters in $M_{\rm i}$ and $\omega_{\rm i}$, includes the interpolation of magnitudes in the `PARS` grid, and concludes with the combination of the primary's and the companion's magnitudes. Figure 4.4 presents the observables

that result from the procedure outlined in this subsection for a subset of unary (single, non-binary) stars on the original `MIST` grid. Here, $v_{\rm e} \sin i$ is calculated from a model's current parameters ω, M, $R_{\rm e}$, and i as

$$v_{\rm e} \sin i = \Omega R_{\rm e} \sin i = \omega \sqrt{\frac{GM}{R_{\rm e}}} \sin i, \tag{4.16}$$

where we have made use of the expression for Keplerian velocity $\Omega_{\rm K}$ in Equation (4.4) and the definition $\omega \equiv \Omega / \Omega_{\rm K}$.

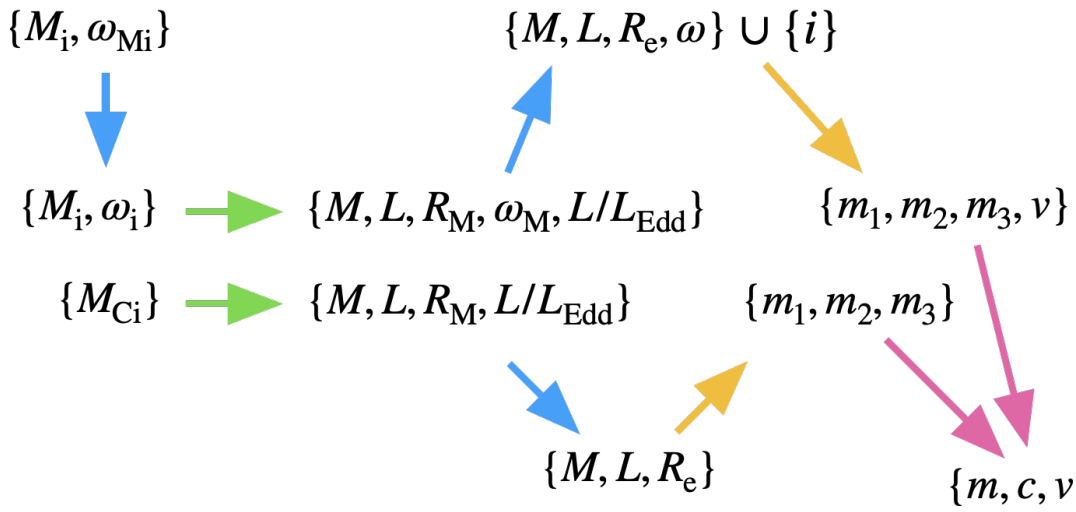

Figure 4.3 Schematic of our procedure for the calculation of the observables $\{m, c, v\}$ at constant age t. The top branch of the schematic pertains to the rotating primary, the bottom – to the non-rotating companion. The combined models are parametrized by initial mass $M_{\rm i}$, binary mass ratio $r \equiv M_{\rm Ci}/M_{\rm i}$, initial rotational speed $\omega_{\rm i}$, and rotational axis inclination i. Blue arrows indicate conversion of rotational speeds and radii (Section 4.2.2), green – interpolation in the `MIST` grid (Section 4.2.1), yellow – interpolation in the `PARS` grid (Section 4.2.3), and pink – combination of the primary's and its companion's magnitudes.

4.3 Probabilities of Observables

Section 4.2 describes the procedures that map stellar model parameters to observable space. The `MIST` model grid is discrete, with substantial separations in mass and rotation rate between neighboring models. Figure 4.4 shows the discrete colors and magnitudes corresponding to the `MIST` grid at two fixed inclinations. Naïvely, such discrete distributions suggest zero probability of stars existing between the discrete locations. To use these observables for statistical inference, we must instead construct *continuous* distributions in color-magnitude space. Colors and magnitudes can change steeply with the initial mass of a stellar model, especially as a star approaches the end of its main sequence life. For combined accuracy and computational efficiency, we seek a grid of model parameters $\boldsymbol{\theta}$ that maps onto a nearly uniform grid in observable space $\boldsymbol{x}$. This grid will be coarse in $\boldsymbol{\theta}$ near parameters for which observables change slowly, and fine where observables change sharply. In this section, we state our priors on model parameters $\boldsymbol{\theta}$, describe the calculation of a suitable $\boldsymbol{\theta}$ grid, our subsequent calculation of continuous distributions in color-magnitude-$v \sin i$ space, and finally the integrations over these distributions that allow us to interpret them as probability densities.

4.3.1 Cluster Model

In this section, we state our prior distributions on stellar parameters $\boldsymbol{\theta}$. The star-by-star posterior distributions that we obtain are the product of these priors and the likelihood, integrated to unit probability. Some of the priors are themselves parametrized by what

are more properly called hyperparameters, i.e., parameters associated with the cluster as a whole. We adopt parametrized descriptions of the rotation rate distribution and the age distribution and fit for those hyperparameters in later sections. Here, we begin by describing our model for the distribution of initial rotation rates before discussing our models and priors on binarity, mass, and age.

We wish to construct a model of the rotational distribution that has reasonable and sufficient degrees of freedom. K20 find evidence for a bimodal $v \equiv v_{\rm e} \sin i$ distribution in NGC 1846, with about 55% of the observed stars clustered near $v = 140\,{\rm km\,s^{-1}}$ and the rest – near $v = 60\,{\rm km\,s^{-1}}$. There is additional evidence of bimodal rotational distributions in clusters (D'Antona et al., 2017; Gossage et al., 2019). We add an extra degree of freedom and assume three rotational populations: one with a maximum probability density at zero rotation, one with maximum density at critical rotation, and one with an intermediate maximum-probability rotation. We assume that each population has a Gaussian distribution of initial rotation rates, truncated at $\omega = 0$ and $\omega = 1$.

We choose parameters for the three Gaussians so that their best-fit amplitudes result in all three distributions contributing a nonzero fraction of the cluster's stars. Many sets of parameters result in all, or nearly all, stars being attributed to only two of these rotational populations. Future work will explore the robustness of our results to different parametrizations of the rotation rates and to changes in the stellar models. For the present work, we use standard deviations of 0.6 and 0.15 in ω for the slow (mean $\omega = 0$) and fast (mean $\omega = 1$) rotating populations. We then find the intermediate rotation rate

where the slow and fast rotating populations contribute equally. We adopt this rotation rate, $\omega = 0.696$, for our intermediate rotators, with a narrow standard deviation of 0.05. The `MIST` model library only extends to $\omega = 0.86$; we use these models for all stars with $0.86 < \omega < 1$.

Our choice of rotational distribution allows for distinct populations of rotators that concentrate at critical, zero, and intermediate rotation, in accordance with the qualitative evidence of such concentrations (Kamann et al., 2020; D'Antona et al., 2017; Gossage et al., 2019).

Multiplicity of stellar systems significantly affects the CMD of a cluster. Similarly to rotation, it can alter both the evolutionary trajectory of a star system (through binary evolution) and its present-day spectrum (by combining the light of the two stars). In the present analysis we include unresolved binarity (a single point source comprising the light of two stars) but neglect the effects of binary evolution. A radial velocity variation technique in Section 4.4 of K20 (see also Giesers et al., 2019) estimates that the unresolved binary fraction of NGC 1846 is $\sim 6\%$. This is similar to estimates of unresolved binary fractions in Galactic globular clusters (Milone et al., 2012). Although K20's binary fraction for NGC 1846 is lower than the estimate of this parameter for the LMC by Moe & Di Stefano (2013), at least part of this difference may be due to the fact that the latter authors work with field stars as opposed to globular cluster stars. K20 argue that the small binary fraction that they find cannot lead to the much larger fraction of slowly rotating stars in NGC 1846, supporting the idea that binary interactions are

generally unlikely to play a significant role in the evolution of stellar rotation rates in this cluster.

We therefore treat each star as either single or as an unresolved binary, with b denoting the hyperparameter for the binary fraction.

For the present analysis, we adopt a uniform prior on the binary fraction b and the simple uniform prior $r \sim U(0,1)$ for the binary mass ratio, although there is some evidence of relative dearth in the middle of r's range. Specifically, Raghavan et al. (2010) say that the mass ratio distribution is approximately uniform for Solar type stars, with a bit of an excess towards equal masses. Other recent papers suggest that the binary mass ratio prefers lower-mass companions, with a bit of an excess towards equal mass companions (Moe & Di Stefano, 2013; Chulkov, 2021).

We assume that the cluster stars have a lognormal distribution in age, with logarithmic mean age μ_t and logarithmic standard deviation σ_t. A coeval cluster would have $\sigma_t = 0$, while a cluster with an age dispersion, as has been suggested for LMC clusters (e.g., Goudfrooij et al., 2011a), would have a significantly nonzero σ_t. We adopt uniform priors on the hyperparameters μ_t and σ_t. This favors younger ages, but given the few percent precision of the age that we derive for NGC 1846, it has a negligible effect on our results.

We adopt the Salpeter IMF, $\pi(M_\mathrm{i}) = M_\mathrm{i}^{-2.35}$, as the prior on the initial mass of the primaries, as well as a prior on inclination that corresponds to an isotropic distribution, $\pi(i) = \sin i$.

Finally, we introduce q, the fraction of stars in the CMD that are described by our cluster model. We assume that the rest of the stars, a fraction $1-q$, come from a population of stars that we haven't modeled. This population could contain stars that are not in the cluster or stars that are in the cluster but aren't described by our stellar model—they exist in regions of the CMD that should be empty. For this background population, we utilize a probability distribution that is uniform over observable space. Our overall cluster model, then, is parametrized by the hyperparameters $\boldsymbol{\phi} \equiv \{w_0, w_2, \mu_t, \sigma_t, b, q\}$.

4.3.2 Probability Density for a Given Population

We next aim to calculate the probability density of a star at each point $\boldsymbol{x}$ in observable space. This is the convolution of the probability density of stars given by the stellar model with that particular star's error kernel. The probability density without observational error would be the same for all stars, but non-uniform uncertainties in color, magnitude, and v break this symmetry.

We define the error kernel with width $\boldsymbol{\sigma_{xp}}$ for a set of observable deviations $\boldsymbol{\Delta}x$ as

$$G(\boldsymbol{\Delta}x; \boldsymbol{\sigma_{xp}}) \equiv G(\Delta m; \sigma_{mp})\, G(\Delta c; \sigma_{cp})\, G(\Delta v; \sigma_{vp}), \tag{4.17}$$

where $G(\Delta y; \sigma)$ is the Gaussian distribution in Δy with mean 0 and standard deviation σ, p is the data point index, and the other subscript on the components of $\boldsymbol{\sigma_{xp}} \equiv (\sigma_{mp}, \sigma_{cp}, \sigma_{vp})$ specifies observable type. This subscript is either m for magnitude, c for color, or v for $v_{\rm e} \sin i$. Thus, the probability of a data point with observables $\boldsymbol{x_p} \equiv$

(m_p, c_p, v_p), given stellar parameters $\boldsymbol{\theta}$, can be written as $G(\boldsymbol{x_p} - \boldsymbol{x}(\boldsymbol{\theta}); \boldsymbol{\sigma_{xp}})$. Here, $\boldsymbol{x}(\boldsymbol{\theta}) \equiv (m(\boldsymbol{\theta}), c(\boldsymbol{\theta}), v(\boldsymbol{\theta}))$, and $m(\boldsymbol{\theta})$, for example, is the magnitude of a star with parameters $\boldsymbol{\theta}$ according to the stellar model.

For each combination of rotational population j, multiplicity k, data point p, and age distribution parameters μ_t and σ_t, we wish to compute $\rho_{jkp}(\boldsymbol{x_p}; \mu_t, \sigma_t)$, the theoretical probability density evaluated at $\boldsymbol{x_p}$, where

$$\rho_{jkp}(\boldsymbol{x}; \mu_t, \sigma_t) = \frac{1}{Z} \int \mathrm{d}\boldsymbol{\theta}\, \pi_{jk}(\boldsymbol{\theta}; \mu_t, \sigma_t)\; G(\boldsymbol{x} - \boldsymbol{x}(\boldsymbol{\theta}); \boldsymbol{\sigma_{xp}}), \tag{4.18}$$

$$\mathrm{d}\boldsymbol{\theta'} = \mathrm{d}M_\mathrm{i}\, \mathrm{d}r\, \mathrm{d}\omega_\mathrm{i}\, \mathrm{d}i, \quad \mathrm{d}\boldsymbol{\theta} = \mathrm{d}\boldsymbol{\theta'}\, \mathrm{d}t, \tag{4.19}$$

$$\pi_{jk}\left(\boldsymbol{\theta'}\right) = \pi_j\left(\omega_\mathrm{i}\right)\; \pi_k\left(r\right)\; \pi(M_\mathrm{i})\, \pi(i), \tag{4.20}$$

$$\pi_{jk}(\boldsymbol{\theta}; \mu_t, \sigma_t) = \bar{\pi}\left(t; \mu_t, \sigma_t\right)\; \pi_{jk}\left(\boldsymbol{\theta'}\right), \tag{4.21}$$

the Gaussian $G(\cdot)$ and the priors $\pi(\cdot)$ on the different components of $\boldsymbol{\theta}$ are given in Section 4.3.1, and $k = 0$ and 1 correspond to unary and binary populations, respectively. The integral is over all $\boldsymbol{\theta}$, though it is finite for a given set of observables $\boldsymbol{x}$, since $\pi(\boldsymbol{\theta})$ is finite and the error kernel at $\boldsymbol{x}$ is non-zero on a finite volume of $\boldsymbol{\theta}$-space. Furthermore, the normalization constant Z is chosen so that probability density $\rho_{jkp}(\boldsymbol{x}; \mu_t, \sigma_t)$ integrates

to one on our region of interest in $\boldsymbol{x}$. Equation (4.18) represents a five-dimensional integral for each star. In the following sections, we describe our approach for evaluating this integral to an acceptable accuracy using as computationally efficient a method as possible.

4.3.3 Stellar Model Grid Refinement

The original `MIST` model grid in Section 4.2.1 is too coarse in mass, age, and rotation rate to accurately integrate in Equation (4.18). Figure 4.4 shows the `MIST` models at a particular age and composition. These models should produce a continuous probability density in mass/color/$v_e \sin i$ space, but the discrete nature of the grid remains obvious. In Appendix B, we motivate and describe our interpolation within the `MIST` models, which generates a grid that is sufficiently fine to produce continuous probability densities. Our approach balances the need to remove discretization artifacts with the need to keep the entire procedure computationally feasible.

The above-mentioned grid refinement procedure requires interpolating within the `MIST` model grid. We perform these interpolations—in mass, rotation, and age—by first converting mass to EEP as described in Section 4.2.1, then treating EEP, age, and rotation as the independent stellar parameters. This allows us to infer mass, equatorial radius, luminosity, and rotation from the `MIST` grid, and to use these to interpolate within the `PARS` grid via the equations of Section 4.2.3. We numerically integrate according to Equation (4.18) on the resulting model grid. Figures 4.5 and 4.6 show that the result-

ing probability densities are free from artifacts of model discretization. In the following section, we describe our integration approach in detail.

4.3.4 Integration Procedure

In Sections 4.3.2 and 4.3.3, we state the integral that we wish to compute in model space, in order to obtain probability densities in observable space. We also outline the production of model grids that allow for accurate integration with minimum computational cost. In this section, we detail our integration procedure, which utilizes a number of additional techniques that ensure accuracy and speed.

Minimum-Error Densities

Equation (4.18) integrates over the 5-dimensional stellar parameter vector $\boldsymbol{\theta}$ to produce theoretical probability densities in observable space. Performing this integral successively on a grid of 3 rotational populations, 2 multiplicities, 2353 data points and a number of age prior parameter combinations is computationally prohibitive. To render the calculation tractable, we assume Gaussian errors and take advantage of the commutativity and associativity of the convolution. We first compute synthetic probability densities of observables (color, magnitude, projected rotational velocity) by integrating Equation (4.18) over five stellar parameters assuming a single set of uncertainties that we term the *minimum errors*. We may then obtain the integrals for a star with larger uncertainties from these integrals by a convolution in three observable dimensions. By decreasing the dimensionality from five to three, and because a Gaussian falls so quickly to zero, this

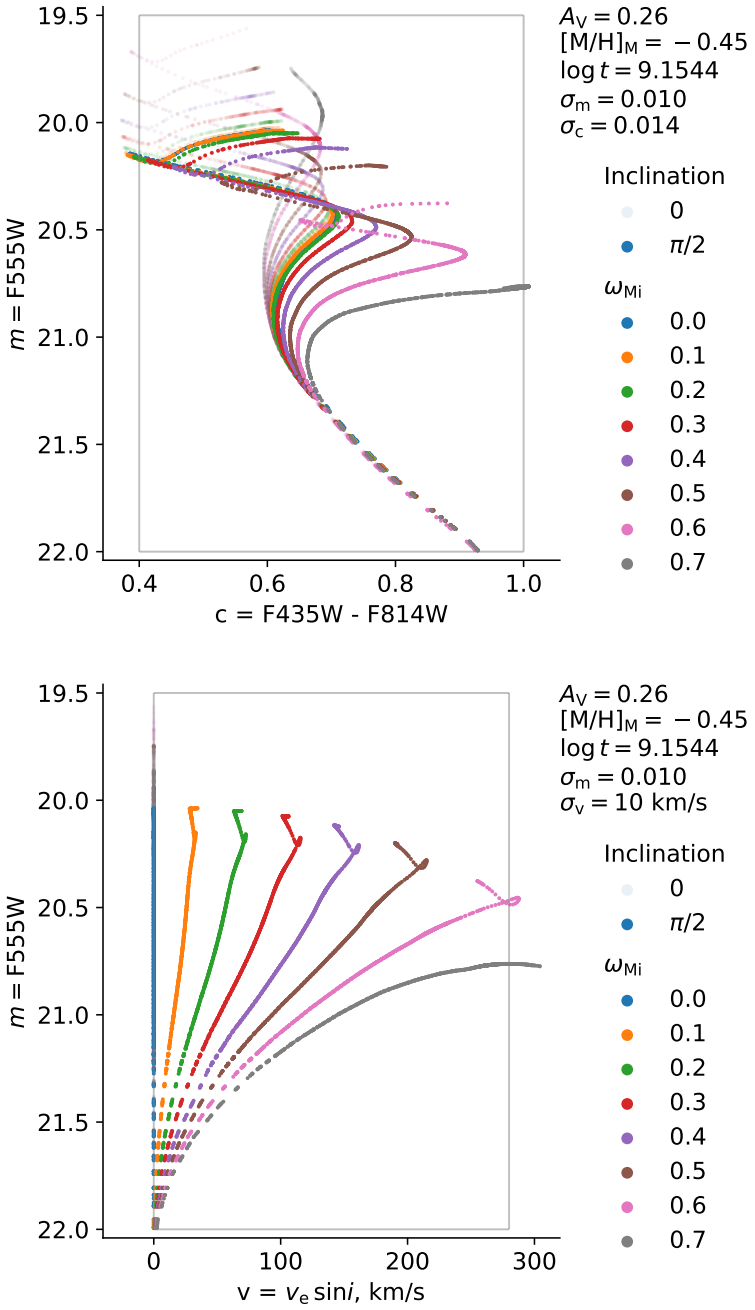

Figure 4.4 `PARS` observables of the original `MIST` models at $\log t = 9.1544$ and two inclinations. At a given $\omega_{\rm Mi}$, decreasing m generally corresponds to increasing $M_{\rm i}$. Marker size is approximately equal to σ_m. Spaces between models in the m dimension are frequently larger than σ_m. The same can be said for the c and v dimensions, though the effect is most pronounced for m. Thus, these discrete models predict no stars in much of the empty space between the markers. This is in contrast with the underlying theory, which is continuous in $M_{\rm i}$ and $\omega_{\rm Mi}$, and thus does predict stars everywhere between the markers.

approach speeds the computation by orders of magnitude without sacrificing accuracy.

Our formal approach begins by writing the convolution of two Gaussians with parameters $\{\mu_1, \sigma_1\}$ and $\{\mu_2, \sigma_2\}$ as another Gaussian with parameters $\{\mu_1 + \mu_2, \sqrt{\sigma_1^2 + \sigma_2^2}\}$. We compute Equation (4.18) for a fixed set of minimum observational uncertainties, which we take to be 0.01 mag in magnitude, 0.014 mag in color, and $10\,\mathrm{km\,s^{-1}}$ in projected rotational velocity. We represent these minimum uncertainties by $\boldsymbol{\sigma_x}$. We then introduce

$$\rho(\boldsymbol{x}; t) \equiv \rho_{jk}(\boldsymbol{x}; t) = \int \mathrm{d}\boldsymbol{\theta}'\, \pi_{jk}(\boldsymbol{\theta}')\, G\left(\boldsymbol{x} - \boldsymbol{x}[\boldsymbol{\theta}'; t]; \boldsymbol{\sigma_x}\right), \tag{4.22}$$

which is the minimum-error version of the probability density in Equation (B.4). Figure 4.5 shows these densities for a single age and composition, for the three different rotational populations and for both single and binary stars. In the following, we describe our approach to compute these probability densities. We again suppress some of the arguments and subscripts in order to describe the computation of the integral in Equation (4.22).

We begin by constructing a fine grid in observable space $\boldsymbol{x}$ to store the probability density given by Equation (4.18). We ensure that this grid extends well outside the ROI on the CMD and well outside the rectangular volume circumscribed by the data points. This allows us to convolve the probability density with error kernels for each star without introducing artifacts from the finite extent of the ROI. Our grid of $\boldsymbol{x}$ is regular and relatively fine, with spacing between neighboring $\boldsymbol{x}$ values $\approx \boldsymbol{\sigma_x}/3$, where $\boldsymbol{\sigma_x}$ is the

vector of minimum error standard deviations.

We then weight $\pi(\boldsymbol{\theta}')$, the prior on initial stellar parameters $\boldsymbol{\theta}'$, according to the composite multi-dimensional trapezoidal rule with variable steps. For example, let us say that we have obtained discrete values of the prior π_h at inclinations i_h with $h \in [1, H]$, $i_0 = 0$, and $i_H = \pi/2$, where π without subscripts indicates the mathematical constant. We designate the differences between neighboring values of inclination by $\Delta i_h = i_{h+1} - i_h$, with $h \in [1, H-1]$. Then, the weighted priors are $\frac{1}{2}(\Delta i_1)\,\pi_1$, $\frac{1}{2}(\Delta i_1 + \Delta i_2)\,\pi_2$, ... $\frac{1}{2}(\Delta i_{H-1} + \Delta i_{H-2})\,\pi_{H-1}$, $\frac{1}{2}(\Delta i_{H-1})\,\pi_H$. We extend this weighting to all parameters in $\boldsymbol{\theta}'$ and place the resulting weighted prior on the $\boldsymbol{x}$-grid according to $\boldsymbol{x}(\boldsymbol{\theta}')$. Calculation of $\boldsymbol{x}(\boldsymbol{\theta}')$ is detailed in Section 4.2.

The density computation described above is not convolved with the error kernel, and shows artifacts of discretization. Convolving with the minimum error kernel completes the calculation of Equation (4.22) and removes these discretization artifacts.

We first perform this task only in the m dimension, i.e., magnitude, simultaneously down-sampling to a coarser grid, with spacing between neighboring m values equal to σ_m. Repeating the procedure in the c and v dimensions, i.e., color and $v_{\mathrm{e}} \sin i$, takes successively less time, since in each case all previous dimensions have been down-sampled. Afterwards, we normalize each resulting probability density $\rho_{jk}(\boldsymbol{x}; t)$ as a function of $\boldsymbol{x}$ on the ROI. We marginalize the density in v to obtain the two-dimensional version $\rho_{jk}(m, c; t)$ and in c to obtain $\rho_{jk}(m, v; t)$, then re-normalize both. Figures 4.5 and 4.6 show the respective marginalized probability densities at $\log t = 9.1594$. Figure 4.6 is an

example of a $v_{\rm e} \sin i$-magnitude diagram (VMD), by analogy with the CMD.

The above procedure, which starts by placing the prior onto $\boldsymbol{x}$-space, is faster than the direct integration in initial model parameter $\boldsymbol{\theta}'$-space implied by Equation (4.22). The computational cost would be similar if we evaluated the likelihood for only one star, with a single location in $\boldsymbol{x}$-space. However, Equation (4.22) represents a five-dimensional integral for every point in the three-dimensional $\boldsymbol{x}$-space. Having performed this integral once, we need only integrate the product of the result and a three-dimensional error kernel for each star. Furthermore, a Gaussian has appreciable support over a limited range of $\boldsymbol{x}$, which also reduces the evaluation cost.

Our ensuing main integration procedure multiplies minimum-error densities $\rho_{jk}(\boldsymbol{x}; t)$ by the residual error kernel, integrates, then multiplies by the log-normal age prior.On the other hand, for diagnostic purposes, we can immediately multiply the minimum-error densities by the age prior $\bar{\pi}(t; \mu_t, \sigma_t)$, then integrate the result. This procedure yields $\rho_{jk}(\boldsymbol{x}; \mu_t, \sigma_t)$, the minimum-error probability density that incorporates the age prior:

$$\rho_{jk}(\boldsymbol{x}; \mu_t, \sigma_t) = \int \mathrm{d}t \, \bar{\pi}(t; \mu_t, \sigma_t) \, \rho_{jk}(\boldsymbol{x}; t). \tag{4.23}$$

Figure 4.7 shows densities $\rho_{jk}(\boldsymbol{x}; \mu_t, \sigma_t)$ for one combination of age mean μ_t and age dispersion σ_t, marginalized over v. This figure shows no artifacts of discretization in age, which supports the idea that the spacing requirement on the age grid in Appendix B.2 has been met. The densities also do not show any age discretization artifacts when marginalized in color c.

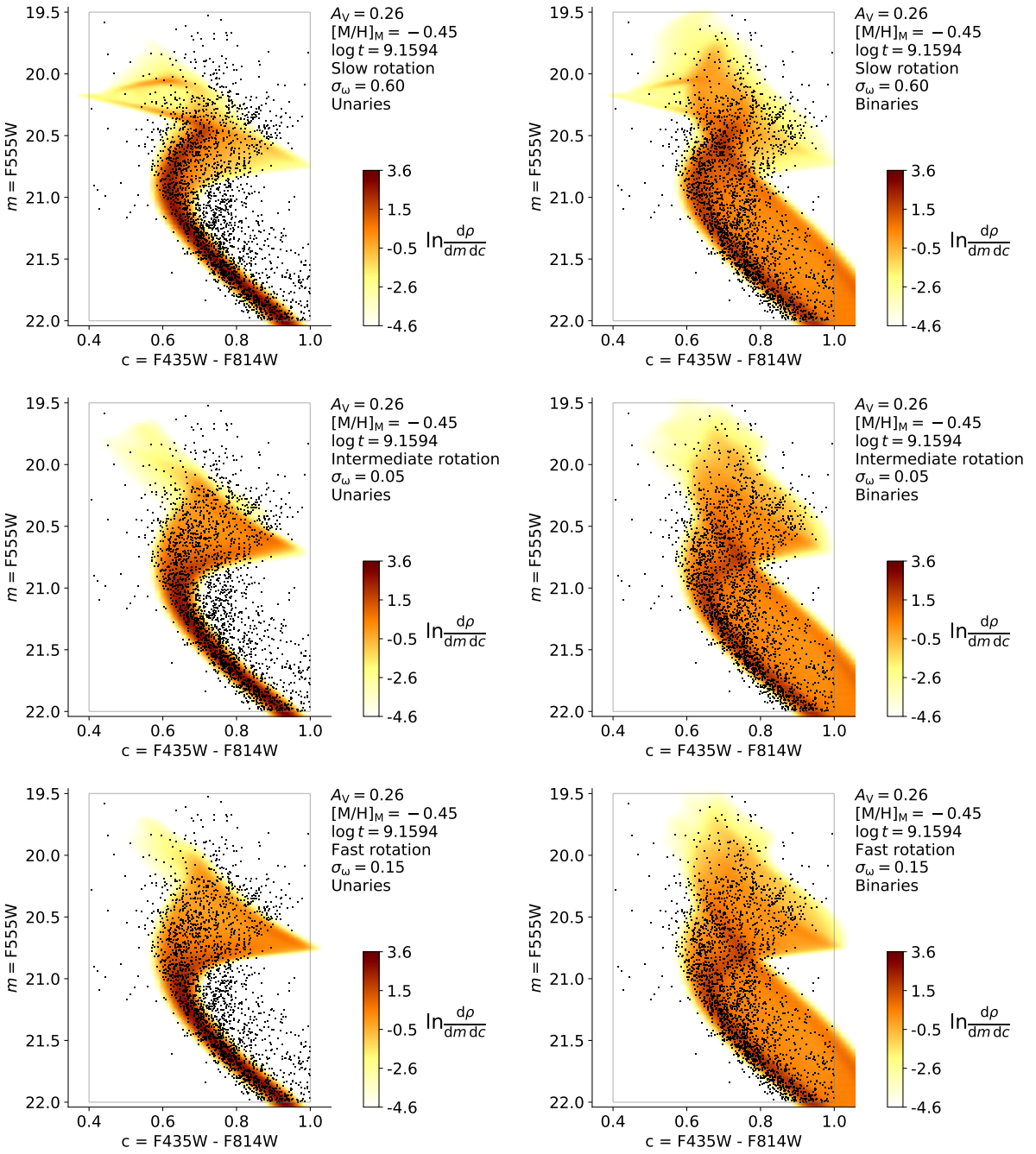

Figure 4.5 Theoretical probability densities at minimum error ($\sigma_m = 0.01$, $\sigma_c = 0.014$) and a specific age, marginalized over projected rotational speed v. These densities are introduced in Section 4.3.4 as $\rho_{jk}(m, c; t)$. Grey lines delimit the region of interest (ROI). Black dots denote our subset of the data from K20. Probability densities for single stars (unaries) are shown on the left and densities for unresolved, non-interacting binaries on the right, for three rotational populations: slow rotators (top), intermediate rotators (middle) and nearly critical rotators (bottom).

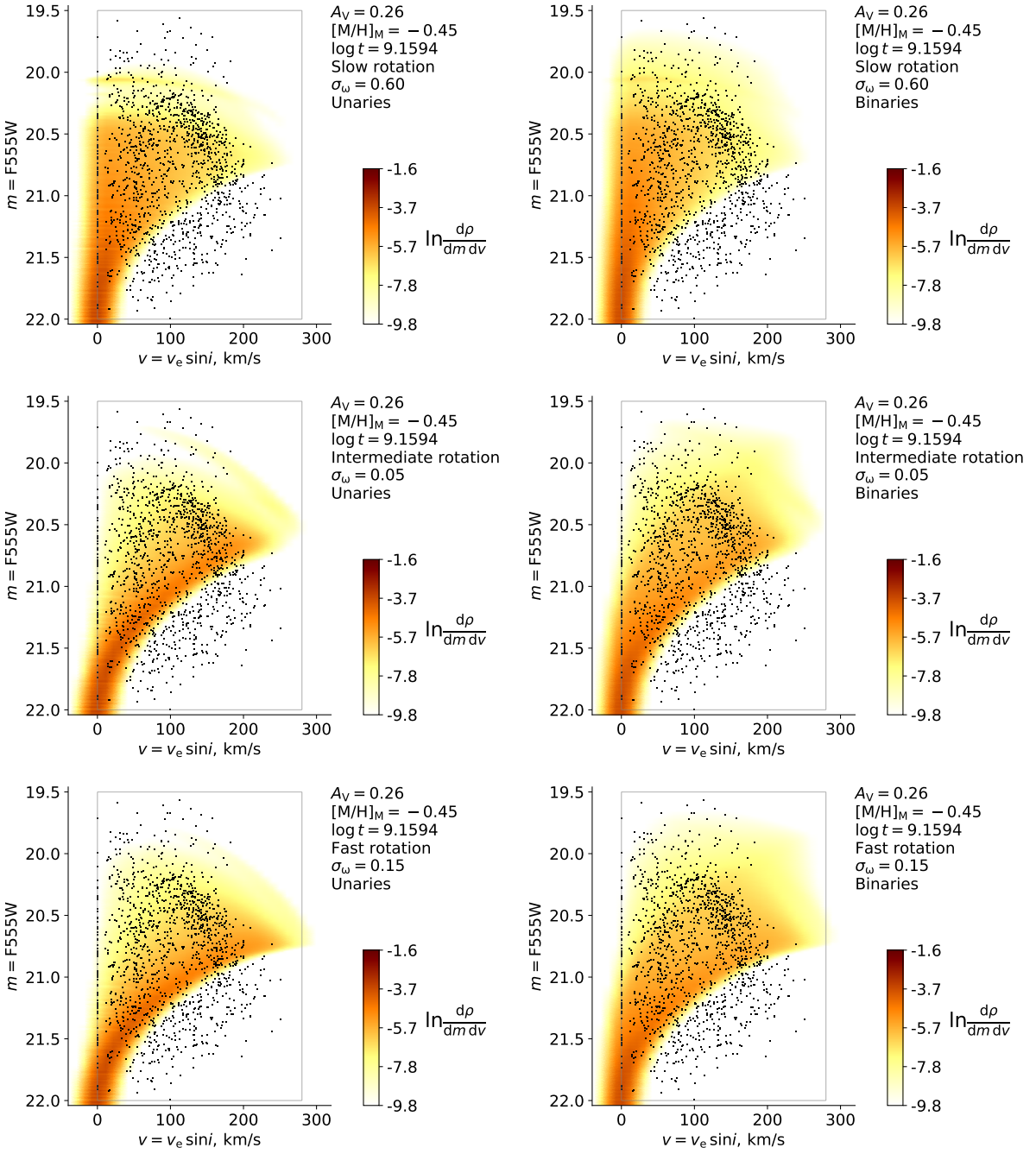

Figure 4.6 Same as Figure 4.5, except the probability densities are marginalized in color c. These densities are introduced in Section 4.3.4 as $\rho_{jk}(m, v; t)$.

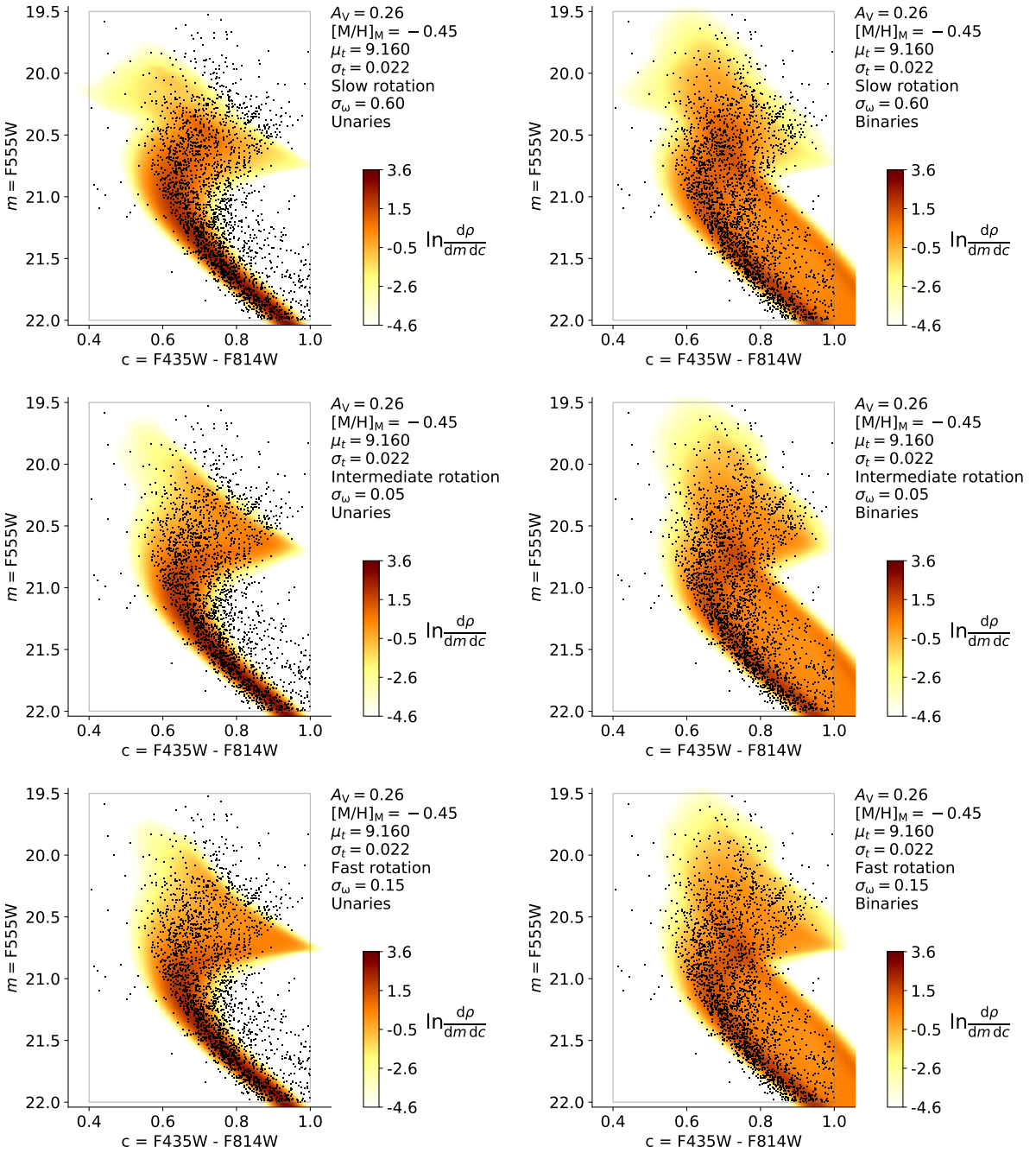

Figure 4.7 Same as Figure 4.5, except the probability densities incorporate a relatively narrow lognormal age prior. These densities are $\rho_{jk}(\boldsymbol{x}; \mu_t, \sigma_t)$ in Equation (4.23), marginalized in v.

De-Normalization Correction

The previous section described the computation of probability densities $\rho_{jk}(\boldsymbol{x};t)$ for the minimum observational uncertainties. We multiply these by the residual error kernel with standard deviation $\sigma'_{\boldsymbol{xp}}$, associated with each data point p, and integrate to obtain a probability density for each star's observed properties. This probability density is evaluated at the star's observables $\boldsymbol{x_p}$. The integral that calculates $\rho_{jkp}(\boldsymbol{x};t)$ for any observable vector $\boldsymbol{x}$ and finite error standard deviation on $v_{\rm e}\sin i$, σ_{vp}, is

$$\rho_{jkp}(\boldsymbol{x};t) = \int \mathrm{d}\boldsymbol{x}'\, \bar{G}\left(\boldsymbol{x}-\boldsymbol{x}';\boldsymbol{\sigma}'_{\boldsymbol{xp}}\right)\, \rho_{jk}(\boldsymbol{x}';t). \tag{4.24}$$

Here, $\boldsymbol{\sigma}'_{\boldsymbol{xp}}$ is the vector of residual standard deviations for data point p and $\bar{G}(\cdot)$ is the normalized Gaussian error kernel. Unlike $\rho_{jk}(\boldsymbol{x}';t)$, we only need $\rho_{jkp}(\boldsymbol{x};t)$ at a single value of $\boldsymbol{x}$, namely $\boldsymbol{x_p}$.

Convolving the minimum error probability density with a normalized error kernel preserves its normalization. However, it does not necessarily preserve its normalization over a restricted subset of the domain, e.g., our ROI. In order to treat the result of Equation (4.24) as a probability density, we must therefore ensure it remains normalized over the ROI. This section describes the procedure we follow in order to make sure that this requirement is met. We term this procedure denormalization correction.

Applying an additional error kernel can denormalize the probability density in magnitude m and color c, the dimensions where the ROI is finite. If the probability density

has a nonzero gradient across the boundary of the ROI, a convolution will move different amounts of probability from inside to outside the ROI as vice versa.

In particular, at m just inside the ROI, there is a contribution to $\rho_{jkp}(m;t)$ due to $\rho_{jk}(m';t)$ at m' outside the ROI. In other words, some amount of probability leaks into the ROI. Similarly, at m just outside the ROI, some amount of probability leaks out. In general, the amount that leaks in is not equal to the amount that leaks out, so that some net leakage occurs. This is a form of selection bias, where the selection is applied to the observed, rather than the intrinsic, properties of each star.

Accordingly, before performing the calculation of probability densities in Equation (4.24) at $\boldsymbol{x} = \boldsymbol{x_p}$ for each data point, we compute the net leakage of probability into or out of the ROI in the course of such calculation as a function of $\boldsymbol{\sigma'_{xp}}$. We perform this calculation separately for the integration in m and in c. For example, for integration in m, rotational population j, and multiplicity population k, we compute the de-normalization correction δ^m_{jk} for a given age t, as a function of residual standard error σ'_m:

$$\delta^m_{jk}(\sigma'_m;t) = \int_{\mathrm{ROI}} \mathrm{d}\boldsymbol{x} \int \mathrm{d}m' \, \bar{G}\left(m - m';\sigma'_m\right) \times \rho_{jk}(m', c, v; t) - 1, \tag{4.25}$$

Once we obtain $\delta^m_{jk}(\sigma'_m;t)$ on a discrete grid of σ'_m, we approximate the corresponding continuous function via cubic interpolation, extrapolating when σ'_{mp} is outside the grid. We obtain this function for c in addition to m in a similar fashion. The result, for both observables and a particular combination of t, j and k, is shown in Figure 4.8. The discrete grids of σ'_m and σ'_c are identical for all combinations of these parameters; for the

combinations where the maximum absolute value of de-normalization drops below 10^{-5} on the grids, we set the function equal to zero.

Rotational Measurement Status

All of our stars have measured colors and magnitudes. Some have positive measured values for $v_e \sin i$, while others either have no measurement due to inadequate signal-to-noise, or have upper limits on their $v_e \sin i$, with a reported $v_e \sin i = 0$. Each of these cases must be treated differently.

When a data point p includes a positive $v_{\rm e} \sin i$ measurement, i.e., when $v_p > 0$, the probability density associated with the point is 3-dimensional, given by Equation (4.24). Recall that we evaluate the integral in this equation, and thus the resulting density, only at the data point's observable vector, $\boldsymbol{x} = \boldsymbol{x_p}$.

Even though a star cannot have $v_{\rm e} \sin i \equiv v < 0$, density $\rho_{jkp}(\boldsymbol{x}; t)$ can be non-zero at negative v as a result of measurement error. This does not affect the densities for data points with $v_p > 0$, since these points never result from $v < 0$ instrument readings. However, a $v_p = 0$ measurement corresponds to $v \leq 0$ instrument readings. Thus, the 2-dimensional probability density at age t for such a measurement, $\rho^{v0}_{jkp}(m, c; t)$, results from integration over $v \leq 0$:

$$\rho^{v0}_{jkp}(m, c; t) = \int_{-\infty}^{0} {\rm d}v \, \rho_{jkp}(\boldsymbol{x}; t), \tag{4.26}$$

which we evaluate before applying the de-normalization correction, and only at the data

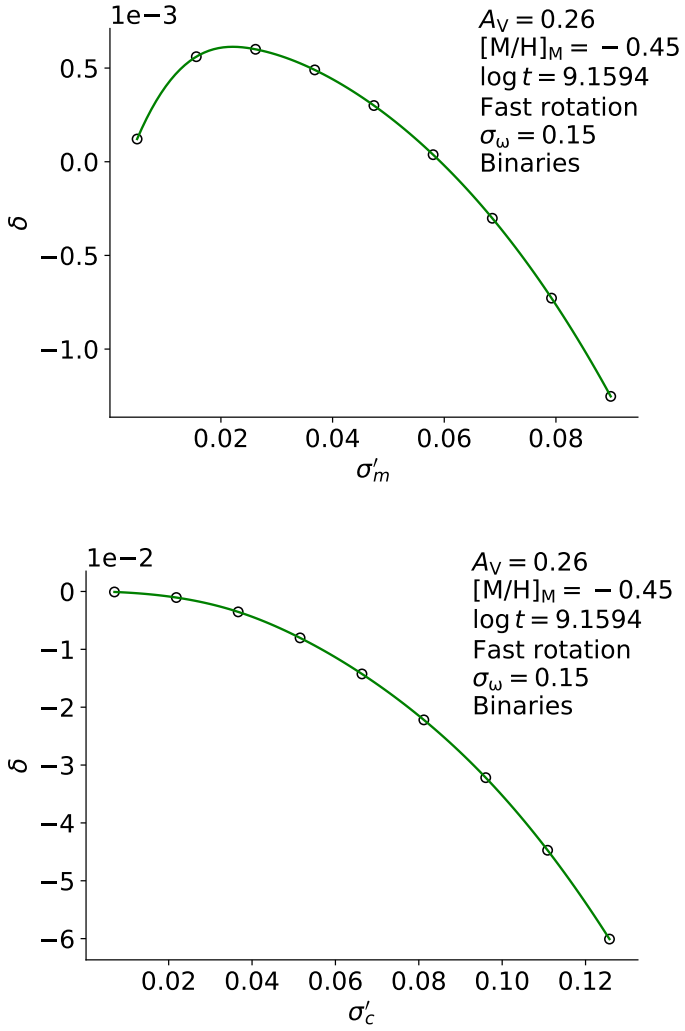

Figure 4.8 De-normalization, i.e., the net probability that leaks into the region of interest upon the convolution of a minimum-error probability distribution with a residual error kernel, versus the kernel's standard deviation σ'. Negative values correspond to net leakage out of the region. The left panel is due to convolution in the magnitude dimension, right panel – in the color dimension. Black open circles indicate the σ' grid where we calculate the de-normalization precisely, with grid range similar to that of the σ' values among the data points. Green lines indicate the cubic interpolant of the function, which we use to approximate the de-normalization between the grid points. The specific combination of age, rotational population, and multiplicity population are the same as in the lower right panel of Figure 4.5. De-normalization due to integration in magnitude remains on the order of 0.1%. On the other hand, that due to color can be on the order of several percent, indicating that the corresponding correction is necessary. These orders of magnitude for the de-normalization correction are typical for the two observables among the probability distributions.

point's observables $m = m_p$ and $c = c_p$.

About half the stars in the ROI have no measurements of v. For these stars, the appropriate probability density is integrated over v and becomes a two-dimensional density $\rho_{jkp}(m, c; t)$ in m and c, evaluated at $m = m_p$ and $c = c_p$.

Consequently, theoretical probability takes the form of the 3-dimensional density function $\rho_{jkp}(\boldsymbol{x}; t)$ only for $0 < v < v_1$. Here, $v_1 = 280\,\mathrm{km\,s^{-1}}$ is an upper limit on $v_\mathrm{e} \sin i$, which is larger than any of the $v_\mathrm{e} \sin i$ measurements. The theoretical probability density is 2-dimensional at $v = 0$ and at $v = v_1$. In particular, the density at $v = 0$ is $\rho^{v0}_{jkp}(m, c; t)$ and we do not need to calculate the density at $v = v_1$. The sum of the integral of the 3-dimensional density and the integrals of the 2-dimensional densities over the functions' respective domains equals 1.

The discussion of de-normalization in Section 4.3.4 applies to the 2-dimensional probability densities $\rho^{v0}_{jkp}(m, c; t)$ and $\rho_{jkp}(m, c; t)$ the same way it applies to the 3-dimensional density $\rho_{jkp}(\boldsymbol{x}; t)$. Accordingly, for example, $\rho_{jkp}(m, c; t)$ is multiplied by the de-normalization correction factor,

$$C_{jk}(\sigma'_{mp}, \sigma'_{cp}; t) = \frac{1}{1 + \delta^m_{jk}(\sigma'_{mp}; t)} \times \frac{1}{1 + \delta^c_{jk}(\sigma'_{cp}; t)}, \tag{4.27}$$

where functions of the form $\delta^m_{jk}(\sigma'_{mp}; t)$ are defined in Equation (4.25).

In the limit of a narrow residual error kernel, the kernel acts as a Dirac delta function. Multiplying with this error kernel and integrating simply picks out a value within the minimum error probability density. We therefore linearly interpolate within the minimum

error density for the dimension(s) in which the residual error σ' is smaller than $\frac{1}{2}$ the minimum error σ. Otherwise, we integrate the product of the minimum uncertainty density and the error kernel using a Riemann sum.

Once we have evaluated the probability densities $\rho_{jkp}(\boldsymbol{x};t)$, $\rho^{v0}_{jkp}(m,c;t)$, and $\rho_{jkp}(m,c;t)$ at $\boldsymbol{x}=\boldsymbol{x_p}$, we can compute the counterparts of these densities that take the age prior into account: $\rho_{jkp}(\boldsymbol{x};\mu_t,\sigma_t)$, $\rho^{v0}_{jkp}(m,c;\mu_t,\sigma_t)$, and $\rho_{jkp}(m,c;\mu_t,\sigma_t)$, which are similar to the minimum-error density $\rho_{jk}(\boldsymbol{x};\mu_t,\sigma_t)$ in Equation (4.23). For example, we can evaluate the following at $\boldsymbol{x}=\boldsymbol{x_p}$:

$$\rho_{jkp}(\boldsymbol{x};\mu_t,\sigma_t)=\int \mathrm{d}t\,\bar{\pi}(t;\mu_t,\sigma_t)\,\rho_{jkp}(\boldsymbol{x};t), \tag{4.28}$$

where $\bar{\pi}(t;\mu_t,\sigma_t)$ is the normalized age prior.

4.3.5 Background Densities

We do not expect our cluster model to describe all the stars in the ROI. Some stars will be interlopers physically unassociated with the cluster. Others will be poorly fit by the cluster model, whether because of neglected binary interactions, imperfect treatment of relevant physics in the stellar model, or something else. We include a background population to account for all of these stars.

We model the distribution of these data points in the space of observable vectors $\boldsymbol{x}$,

instead of model space:

$$\pi(\boldsymbol{x}) = H(v), \tag{4.29}$$

where $v \equiv v_{\rm e} \sin i$ and $H(v)$ is the Heaviside step function, with $H(0) = 1$. In other words, we take these background data points to be uniformly distributed over color, magnitude, and v, subject to the constraint that $v \geq 0$. The densities, after convolving with an error kernel, remain uniform in c and m, but are not uniform in v because of the physical constraint that $v \geq 0$. The background density becomes

$$\rho_{{\rm b}p}(\boldsymbol{x}) = \int {\rm d}\boldsymbol{x}' \, \pi(\boldsymbol{x}) \, G(\boldsymbol{x} - \boldsymbol{x}'; \boldsymbol{\sigma_{xp}}) = \frac{1}{V_x} \times \frac{1}{2} \left(1 + {\rm erf} \left[\frac{v}{\sigma_{vp}\sqrt{2}} \right] \right), \tag{4.30}$$

where erf is the error function, $G(\bullet)$ is the appropriate Gaussian error kernel, σ_{vp} is the error in v for point p, and V_x is a normalization constant. The density $\rho_{{\rm b}p}(\boldsymbol{x})$ in Equation (4.30) plays the same role for the background population as density $\rho_{jkp}(\boldsymbol{x}; \mu_t, \sigma_t)$ in Equations (4.18) and (4.28) for the modeled population. A key difference is in the treatment of the upper boundary at $v = v_1$. In the case of the modeled population, we had allowed for the possibility of data points with v measurement $v_p > v_1 = 280\,{\rm km\,s^{-1}}$, even if no such points were realized in our data set. For the background population, we assume that all data points with $v_p > v_1$ are ignored, so that no integrated probability value accumulates at this boundary, and we set V_x so that $\rho_{{\rm b}p}(\boldsymbol{x})$ integrates to 1 on the ROI that is restricted to $v \leq v_1$. With v_1 taken to be much greater than σ_{vp} for all p, we

obtain $V_x = (m_1 - m_0)(c_1 - c_0)v_1$.

On the other hand, we treat the $v = 0$ boundary for the background population density the same way we treat it in the case of modeled population densities. Thus, similarly to the manner of Section 4.3.4, we calculate the respective uniform background probability densities relevant for the data points with $v_p = 0$ and $\sigma_{vp} = \infty$ as

$$\rho_{\mathrm{b}p}^{v0}(m, c) = \int_{-\infty}^{0} \rho_{\mathrm{b}p}(\boldsymbol{x}) = \frac{1}{V_x} \frac{\sigma_{vp}}{\sqrt{2\pi}} \tag{4.31}$$

and

$$\rho_{\mathrm{b}p}(m, c) = \int_{-\infty}^{v_1} \rho_{\mathrm{b}p}(\boldsymbol{x}) = \frac{1}{(m_1 - m_0)(c_1 - c_0)}. \tag{4.32}$$

4.4 Statistical Model

In this section, we describe our statistical model, which combines theoretical probability densities for different rotational and multiplicity populations to infer the population parameters of the MSTO in NGC 1846 from the measurements of the turnoff's individual stars.

4.4.1 Combined Probability Densities

The cluster model in Section 4.3.1 allows for 6 combinations of rotational population and multiplicity in the case when a data point is due to the stellar model, as well as the

possibility that the datum is not due to the stellar model, but rather the background population. We now combine the probability densities for these 7 populations from Section 4.3 to obtain normalized densities for a given set of cluster parameters. For example, when a data point p has rotational measurement $v_p > 0$, the combined probability density $\rho_p(\boldsymbol{x}; \boldsymbol{\phi})$ is

$$\rho_p(\boldsymbol{x}; \boldsymbol{\phi}) = q(1-b) \sum_i w_i \, \rho_{i0p}(\boldsymbol{x}; \mu_t, \sigma_t) + qb \sum_i w_i \, \rho_{i1p}(\boldsymbol{x}; \mu_t, \sigma_t) + (1-q)\rho_{\mathrm{bp}}(\boldsymbol{x}), \tag{4.33}$$

where the cluster parameters $\boldsymbol{\phi}$ are composed of fit quality q (the fraction of stars described by the model), binary fraction b, rotational population proportions (w_0, w_1, w_2), and parameters of the age prior (μ_t, σ_t). These parameters obey $q \in (0,1)$, $b \in (0,1)$, $w_i \in (0,1) \, \forall \, i$, and $w_0 + w_1 + w_2 = 1$. Additionally, the second subscript k in $\rho_{ikp}(\cdot)$ is zero for the unaries and one for the binaries, $\boldsymbol{x} \equiv (m, c, v)$ is the observables vector, and $\rho_{\mathrm{bp}}(\boldsymbol{x})$ is the background density for point p. We similarly obtain densities $\rho_p^{v0}(m, c; \boldsymbol{\phi})$ and $\rho_p(m, c; \boldsymbol{\phi})$, relevant for the other two cases of rotational measurement status. Much like in Section 4.3, each probability density is only evaluated at the corresponding data point's observables, $\boldsymbol{x} = \boldsymbol{x}_p$. Additionally, we define a partial vector of cluster parameters $\boldsymbol{\phi}' = \{\mu_t, \sigma_t, w_0, w_2\}$ and, for every point p with $v_p > 0$, likelihood factor

$$\varrho_p \equiv \varrho_p(\boldsymbol{\phi}) \equiv \frac{\rho_p(\boldsymbol{x_p}; \boldsymbol{\phi})}{\rho_{\mathrm{bp}}(\boldsymbol{x_p})}. \tag{4.34}$$

Quantity ϱ_p is similarly defined when each relevant probability density has 2 dimensions instead of 3.

Next, we describe the statistical model that allows us to combine $\rho_p(\boldsymbol{x};\boldsymbol{\phi})$ and its lower-dimensional counterparts to obtain probabilities of all data under different cluster parameter combinations.

4.4.2 The Likelihood of a Cluster Model

Our model of data generation assumes stars to arise as from a Poisson process. It is closely related to an existing method for fitting data to stellar model distributions in color-magnitude space (Naylor & Jeffries, 2006), which was recently adapted to the space with dimensions of mass and rotational period (B21).

Given cluster parameters $\boldsymbol{\phi}$, we assume that the n_p data points with positive rotational measurement $v_p > 0$ result from an n_p-sized subset of $N_\mathrm{p} \gg n_\mathrm{p}$ Poisson processes, each non-homogeneous in $\boldsymbol{x}$-space and limited to the ROI. In other words, we assume a very large number of draws from underlying stellar probability distributions, a small fraction of which result in stars that appear in our data set. When we consider all the Poisson processes, we index them by $h \in \{1, \ldots, N_\mathrm{p}\}$. When we consider only the subset that produces data points, we use the same index we use for the points, $p \in \{1, \ldots, n_\mathrm{p}\}$. Let us say we have partitioned $\boldsymbol{x}$-space into a large number of bins, with widths Δm, Δc and Δv in each of the observable dimensions. In this case, the expected number of stars

($\ll 1$) resulting from process h at location $\boldsymbol{x}$ is

$$\lambda_h(\boldsymbol{x}) = \epsilon\, \rho_h(\boldsymbol{x})\, \Delta\boldsymbol{x}, \tag{4.35}$$

where $\epsilon \ll 1$, so that a given process does not produce more than one data point, $\rho_h(\boldsymbol{x})$ is a probability distribution normalized on the ROI and given by Equation (4.33), and we have suppressed $\boldsymbol{\phi}$ in this distribution's definition. In this case, $\Delta\boldsymbol{x} \equiv \Delta m \Delta c \Delta v$.

If $k_h(\boldsymbol{x})$ is the number of data points produced by process h in a bin centered on $\boldsymbol{x}$, the probability of all data is

$$\prod_h \prod_x \frac{\lambda_h(\boldsymbol{x})^{k_h(\boldsymbol{x})} e^{-\lambda_h(\boldsymbol{x})}}{k_h(\boldsymbol{x})!}, \tag{4.36}$$

where ! represents the factorial. The different Poisson processes indexed by h are distinguished by differing uncertainties on the measured color, magnitude, and $v_e \sin i$. In this case, since each Poisson process produces at most one star, the denominator is unity.

If all data points had the same uncertainties, then each distribution h would be identical. In this case, the total number of stars in the bin would be a Poisson random number with expectation value

$$\lambda(\boldsymbol{x}) = \sum_h \lambda_h(\boldsymbol{x}) \tag{4.37}$$

and an actually detected number of stars

$$k(\boldsymbol{x}) = \sum_h k_h(\boldsymbol{x}). \tag{4.38}$$

The probability of observing the data would then be

$$\prod_x \frac{\lambda(\boldsymbol{x})^{k(\boldsymbol{x})} e^{-\lambda(\boldsymbol{x})}}{k(\boldsymbol{x})!}. \tag{4.39}$$

This differs from Equation (4.36), but if all Poisson processes h are identical, it differs only by a constant independent of the model that gives λ. Specifically, the denominator in the two equations depends only on the number of stars actually observed in a given bin, and their exponential term is identical given Equation (4.37). The term $\lambda(\boldsymbol{x})^{k(\boldsymbol{x})}$ will differ by a constant, equal to $N_p^{k(\boldsymbol{x})}$, from its corresponding term in Equation (4.36). In sum, Equation (4.36) is more general than Equation (4.39) but the former equation reduces to the latter (up to a constant) if the uncertainties on all stellar measurements are identical.

Equation (4.36) gives the probability of detecting a given number of stars in discrete bins of color-magnitude-$v \sin i$ space. In color and magnitude alone, these bins form a Hess diagram (Bastian & Silva-Villa, 2013; Rubele et al., 2013), where an integer number of stars are present in each bin. Hess diagram approaches based on Equation (4.39) have often been used to infer cluster properties. However, they cannot account for differences in uncertainties between different stars and they cannot naturally account for $v \sin i$ as the

third dimension. Our approach is different: we take the limit where $\Delta m \to 0$, $\Delta c \to 0$, and $\Delta v \to 0$. In this limit, with $k(\boldsymbol{x})$ either 0 or 1, the probability of all data in Equation (4.36) becomes

$$\prod_h \left(\prod_x e^{-\lambda_h(\boldsymbol{x})} \prod_{\boldsymbol{x}:\, k_h(\boldsymbol{x})=1} \lambda_h(\boldsymbol{x}) \right). \tag{4.40}$$

In this limit, the probability distributions are continuous rather than discrete and $v \sin i$ information can be naturally incorporated. It does, however, require us to use the continuous probability distributions that we have computed in Section 4.3.4.

Equation (4.40) contains two components within the parentheses. The first term is nontrivial for all Poisson processes indexed by h. The second term, however, is unity unless Poisson process h actually results in a detected star, i.e., unless $k_h(\boldsymbol{x}) = 1$ for some $\boldsymbol{x}$ (otherwise λ_h is always raised to the zero power). Consequently, for the second term in Equation (4.40), we switch to indexing by p to indicate the processes that produce data points. Expression (4.40) becomes

$$\left(\prod_h \prod_x e^{-\lambda_h(\boldsymbol{x})} \right) \left(\prod_p \lambda_p \left(\boldsymbol{x_p} \right) \right), \tag{4.41}$$

where the right product is only over the Poisson processes that produce data points, since the product factor for other processes is equal to 1. Additionally, for now, this product is restricted to the data points with $v_p > 0$. With the help of Equation (4.35), the left

product in Expression (4.41) can be written as

$$\prod_h \exp\left(-\epsilon \sum_{\boldsymbol{x}} \rho_h(\boldsymbol{x})\, \Delta\boldsymbol{x}\right) = \prod_h \exp\left(-\epsilon \int_{\mathrm{ROI}} \rho_h(\boldsymbol{x})\, \mathrm{d}\boldsymbol{x}\right) = e^{-\epsilon N_{\mathrm{p}}}, \tag{4.42}$$

where we have applied the limit that turns $\Delta\boldsymbol{x}$ into $\mathrm{d}\boldsymbol{x}$ and the sum into an integral. We also used the fact that $\rho_h(\boldsymbol{x})$ is normalized on the ROI.

Application of Equation (4.35) allows us to write the right product in Expression (4.41) as

$$\prod_p \epsilon\, \rho_p\left(\boldsymbol{x_p}\right)\, \Delta\boldsymbol{x} = \epsilon^{n_{\mathrm{p}}} \left(\Delta\boldsymbol{x}\right)^{n_{\mathrm{p}}} \prod_p \rho_p\left(\boldsymbol{x_p}\right). \tag{4.43}$$

Multiplying Expressions (4.42) and (4.43) together, we see that the probability of the data points with $v_p > 0$, given by Expression (4.41), is

$$e^{-\epsilon N_{\mathrm{p}}} \epsilon^{n_{\mathrm{p}}} \left(\Delta\boldsymbol{x}\right)^{n_{\mathrm{p}}} \prod_p^{n_{\mathrm{p}}} \rho_p\left(\boldsymbol{x_p}\right). \tag{4.44}$$

We repeat the above procedure in this section for the data points with each of the remaining possibilities of the rotational measurement status, in each case substituting $\rho_p\left(\boldsymbol{x_p}\right)$ with the appropriate 2-dimensional distribution and $\Delta\boldsymbol{x}$ with $\Delta m\, \Delta c$. The probability of all data points with $v_p = 0$ turns out to be

$$e^{-\epsilon N_0} \epsilon^{n_0} \left(\Delta m\, \Delta c\right)^{n_0} \prod_p^{n_0} \rho_p\left(m_p, c_p\right), \tag{4.45}$$

and similarly for the data points with $\sigma_v = \infty$ (i.e., those without measured $v \sin i$). Now, we denote $\rho_p(\boldsymbol{x_p})$, $\rho_p(m_p, c_p)$ and $\rho_p^{v0}(m_p, c_p)$ collectively as ρ_p. Multiplying together Expressions (4.44), (4.45) and the remaining, similar expression, we obtain the probability of all the data:

$$e^{-\epsilon N} \epsilon^n (\Delta v)^{n_{\mathrm{P}}} (\Delta m \, \Delta c)^n \prod_p^n \rho_p, \tag{4.46}$$

where N is the total number of Poisson processes. We are free to define the likelihood of cluster parameters $\boldsymbol{\phi}$ as Equation (4.46) times any factor that doesn't depend on $\boldsymbol{\phi}$. We first retain only the right-most product over the data points indexed by p in this expression, since all other factors are independent of $\boldsymbol{\phi}$. We then divide this product by the product of the appropriate 2- and 3-dimensional background densities at data point observables, which is also independent of $\boldsymbol{\phi}$. This yields the following likelihood function:

$$\mathcal{L}(\boldsymbol{\phi}) = \prod_p^n \varrho_p, \tag{4.47}$$

where ϱ_p are the data point likelihood factors, defined in Equation (4.34). Appendix C.1 describes the procedure that leads to $\hat{\boldsymbol{\phi}}$, the cluster parameters that maximize $\mathcal{L}(\boldsymbol{\phi})$ in Equation (4.47). We split the data set into subsets that correspond to the three statuses of rotational measurement and calculate the relative differences in $\ln \rho_p$ at $\hat{\boldsymbol{\phi}}$ within each subset. These differences are presented in Figure 4.9. The exponent of the sum of these over all stars gives the likelihood of the set of cluster parameters $\hat{\boldsymbol{\phi}}$ that maximizes the

likelihood function.

4.4.3 Posterior Cluster Parameters

Equation (4.47) gives the likelihood of a set of cluster parameters. Our final step is to normalize the likelihood to obtain a posterior probability distribution of these cluster parameters. We do not use MCMC, but rather directly integrate the likelihood multiplied by our adopted priors on cluster parameters $\boldsymbol{\phi}$. We assume log-uniform priors on μ_t and σ_t and uniform priors on all other components of $\boldsymbol{\phi}$. This way, likelihood as a function of $\boldsymbol{\phi}$ can already be seen as the un-normalized posterior. We then define

$$\mathcal{L}(\boldsymbol{\phi}') = \int \mathrm{d}q\, \mathrm{d}b\, \mathcal{L}(\boldsymbol{\phi}). \tag{4.48}$$

Details of the integration procedure that we use to evaluate Equation (4.48) can be found towards the end of Appendix C.1.

If we normalize $\mathcal{L}$, we can interpret it as a Bayesian probability density, $P(\boldsymbol{\phi}) = \mathcal{L}(\boldsymbol{\phi}) Z_{\mathcal{L}}^{-1}$, where

$$Z_{\mathcal{L}} = \int \mathrm{d}\boldsymbol{\phi}\, \mathcal{L}(\boldsymbol{\phi}) \tag{4.49}$$

is an integral over some formal region of normalization.

We wish to obtain $P(\boldsymbol{\phi}') \propto \mathcal{L}(\boldsymbol{\phi}')$ after evaluating the likelihood over a subset of the

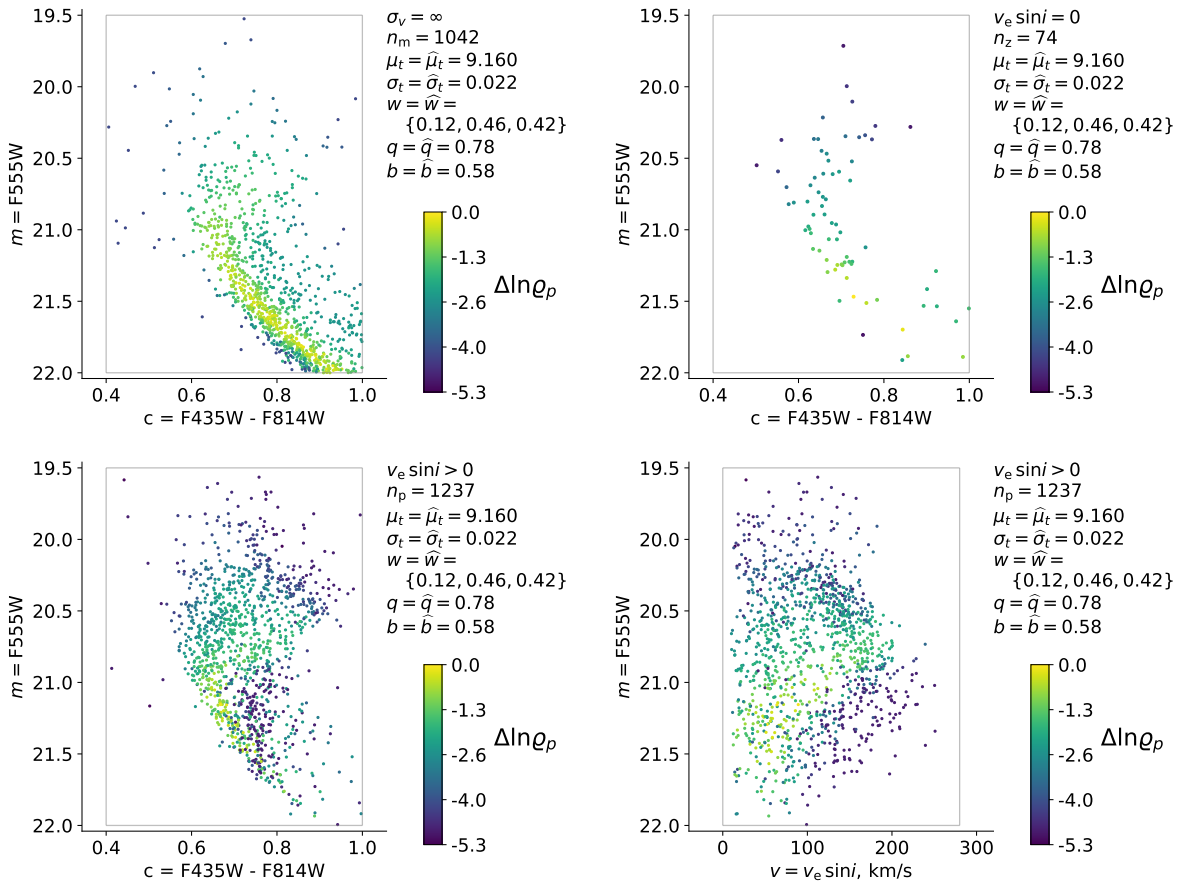

Figure 4.9 Color scheme shows the relative likelihood factors $\Delta \ln \varrho_p$ for individual points (defined due to Section 4.4.2) in our portion of the data from K20, at the maximum-likelihood cluster parameters $\hat{\boldsymbol{\phi}}$. Comparison of two factors is only meaningful when their rotational measurement status is the same. Thus, the top left panel compares the 1042 points without $v_e \sin i$ measurements, the top right panel – the 74 points with $v_e \sin i = 0$, and the bottom two panels – the 1237 points with $v_e \sin i > 0$. Likelihood factor difference of $\Delta \ln \varrho_p = 2$, such as between a yellow point and a green point, indicates a 7.4-fold difference in probability density between the locations of the two points in observable space, since $e^2 \approx 7.4$. Cluster model parameters A_V, $[\mathrm{M/H}]_\mathrm{M}$, and σ_ω are the same as in Figure 4.7.

normalization region. We can also marginalize $P(\boldsymbol{\phi}')$ in w_0 and w_2:

$$P(\mu_t, \sigma_t) = \int \mathrm{d}w_0 \, \mathrm{d}w_2 \, P(\boldsymbol{\phi}') \propto \int \mathrm{d}w_0 \, \mathrm{d}w_2 \, \mathcal{L}(\boldsymbol{\phi}'), \tag{4.50}$$

which would provide us with a confidence region for the age distribution parameters. Similarly, we can get a confidence region for the rotational population proportions by calculating $P(w_0, w_2)$. Appendix C.2 describes the integration procedures that produce $P(\mu_t, \sigma_t)$ and $P(w_0, w_2)$ in the fashion suggested by Equation (4.50).

Our final step is to assess the goodness of fit: whether the maximum likelihood cluster parameters, together with the stellar model, provide a good description of the cluster. We assess goodness of fit by the maximum likelihood value of parameter q, the fraction of stars that are described by the cluster model, given the maximum likelihood values of all the cluster parameters. The remainder of the stars, a fraction $1 - q$, must be accounted for in a background population. Our sample of stars near the main sequence turnoff is overwhelmingly dominated by real cluster members. A formally good model, then, should have q very close to one ($\gtrsim$0.95). Lower values of q indicate that many cluster stars cannot be well-fit by the stellar model, and that the rest of the cluster parameters should be interpreted cautiously.

4.5 Results

In this section, we present the maximum-likelihood (ML) cluster parameter estimates that result from the evaluation of likelihoods that we defined in Section 4.4.2. We also offer bounds on these estimates, which are based on the integration of the likelihoods, as described in Appendix C.1 and the integration of Bayesian probabilities in Appendix C.2. We caution that, due to the intermediate quality of the fit between the evolutionary model and the data, our cluster parameter estimates are only somewhat reliable. In this section and, especially, in Sections 4.6 and 4.7, we discuss the degree of reliability and the ways in which one might calibrate the stellar evolutionary model to better fit cluster data and consequently produce cluster parameter estimates that are more trustworthy.

Our ML estimate of the probability that an observed star is due to the evolutionary model is $\hat{q} = 0.78$. In other words, 22% of the stars are better explained by a uniform background distribution. The actual fraction of contaminants is expected to be much lower ($\approx 190/3189 = 6\%$, based on Sections 3.4 and 3.5 of K20). Even though our $\hat{q}$ indicates that the stellar model can account for the observed photometry and $v_{\rm e} \sin i$ measurements of most stars in the ROI, the remainder of the stars constitute a signficant minority. The $\sim$80% of stars that are accounted for by the stellar model contribute to the inference of cluster parameters w_0, w_2, μ_t, σ_t, and b in this work. An evolutionary model with a higher $\hat{q}$ would fit the data better, thus producing cluster parameter estimates that would be more reliable. Since $1 - \hat{q} = 0.22$ is appreciable, such new estimates could be very different from this work's. The parameter $\hat{q}$ can serve as a measure of the

goodness-of-fit of the stellar model.

Roughly speaking, the non-zero value of $1-\hat{q}$ results from 22% of the data points with the lowest likelihood factor offset $\Delta \ln \varrho_p$ within each subset of the rotational measurement status in Figure 4.9. These are the stars that are most inconsistent with our cluster model. The bottom panels of this figure present relative likelihood factors $\Delta \ln \varrho_p$ for individual stars with $v_{\rm e} \sin i > 0$ at ML cluster parameters. Of these stars, $316/1237 = 26\%$ have $\Delta \ln \varrho_p \leq -4$. We define these as the $v_{\rm e} \sin i > 0$ data points that poorly match the evolutionary model. Near the middle of the turnoff, at a magnitude $m \approx 20.7$, nearly all stars are satisfactorily accounted for by the model. At brighter magnitudes, the model predicts a smaller proportion of stars (see Figure 4.7). At fainter magnitudes, it predicts the stars to exist only in a narrow color spread around $c = 0.75$ and at very low rotational speeds (see Figure 4.6). As we discuss later, in Section 4.6, it is likely that reduction in the evolutionary model's magnetic braking may significantly improve the model's match to the dimmer points.

As furthermore discussed in Section 4.6, our ML estimate of the binary fraction, $\hat{b} = 0.58$, is almost certainly higher than the parameter's real value; a reduction in magnetic braking is likely to reduce our estimate significantly. Thus, we do not compute the formal confidence region for b, although Section C.1 shows that, generally, $\sim 99.9\%$ of the integrated likelihood lies between $b_0 = 0.40$ and $b_1 = 0.76$. We similarly treat the confidence region for q, with the following limits from Section C.1: $q_0 = 0.70$ and $q_1 = 0.84$.

In Section 4.3.1, we state our rotational population model, with slow rotators distributed according to a wide half-Gaussian peaked at zero rotation, fast rotators – according to a narrow half-Gaussian peaked at critical rotation, and intermediate rotators – according to a narrow Gaussian with a peak at the location where the other two probability densities are equal. We chose the widths of the three distributions to ensure that the ML estimates of the corresponding population proportions are all appreciably greater than zero, i.e., that the data distinguish between three separate populations to a large degree. The population proportion estimates are between the corresponding 1-dimensional boundaries of the 2-dimensional 95% confidence region in the right panel of Figure 4.10: $\hat{w}_0 = 0.11 \in [0.03, 0.21]$ and $\hat{w}_2 = 0.42 \in [0.19, 0.68]$ for the slow and the fast rotators, respectively. The width of the confidence region in the w_2 dimension is significantly larger than that in the w_0 dimension, indicating that the slow rotator population is more distinct from the fast and intermediate rotators than the latter are from each other. This interpretation makes sense in view of a qualitative comparison between the three populations' theoretical probability densities in Figure 4.5 and suggests that the true rotational distribution is bimodal instead of trimodal.

The population proportion of the intermediate and fast rotators is $\hat{w}_1 + \hat{w}_2 = 0.89$–the vast majority of stars. This combined population is somewhat larger than the population with high $v_\mathrm{e} \sin i$ in K20 with a distribution that peaks around $v_\mathrm{e} \sin i = 140\,\mathrm{km\,s^{-1}}$ and a population proportion of ~ 0.55. The correspondence is very rough, considering both the difference in the estimated proportions between the two studies and the fact that all

rotational populations in this work have probability distributions that extend over most of the $v_{\rm e} \sin i$ range (e.g., see Figure 4.6). Nonetheless, it is encouraging that our results, like those of K20, point to a bimodal rotational distribution.

Our ML estimates of the age distribution parameters are within the 95% confidence region in the left panel of Figure 4.10: $\hat{\mu}_t = 9.1600 \in [9.1569, 9.1628]$ and $\hat{\sigma}_t = 0.0225 \in [0.0193, 0.0260]$. The corresponding non-logarithmic values are $1.445 \in [1.435, 1.455]$ Gyr and $75 \in [64, 87]$ Myr, where the non-logarithmic equivalent of a logarithmic standard deviation σ_t is $10^{\hat{\mu}_t + (\sigma_t/2)} - 10^{\hat{\mu}_t - (\sigma_t/2)}$. Parameters $\hat{\mu}_t = 9.160$ and $\hat{\sigma}_t = 0.023$ correspond to an age distribution with high probability of $\log t = 9.14$, the age adopted in K20. The left panel of Figure 4.10 shows that the Bayesian probability distribution covariance between $\hat{\mu}_t$ and $\hat{\sigma}_t$ is small, which suggests that our age and age dispersion estimates are not greatly affected by the specific log-normal shape of the prior on stellar age. Furthermore, since the posteriors on μ_t and σ_t are both rather narrow, we conclude that our estimates of these parameters are not greatly affected by our specific choices of their relatively uninformative priors.

4.6 Discussion

Both the theory of stellar evolution and the theory of cluster formation have ingredients that are subject to considerable uncertainty. On the other hand, well-established ingredients of one of these theories could help reduce uncertainty in the other. We are specifically interested in a better understanding of the rotational and age distributions

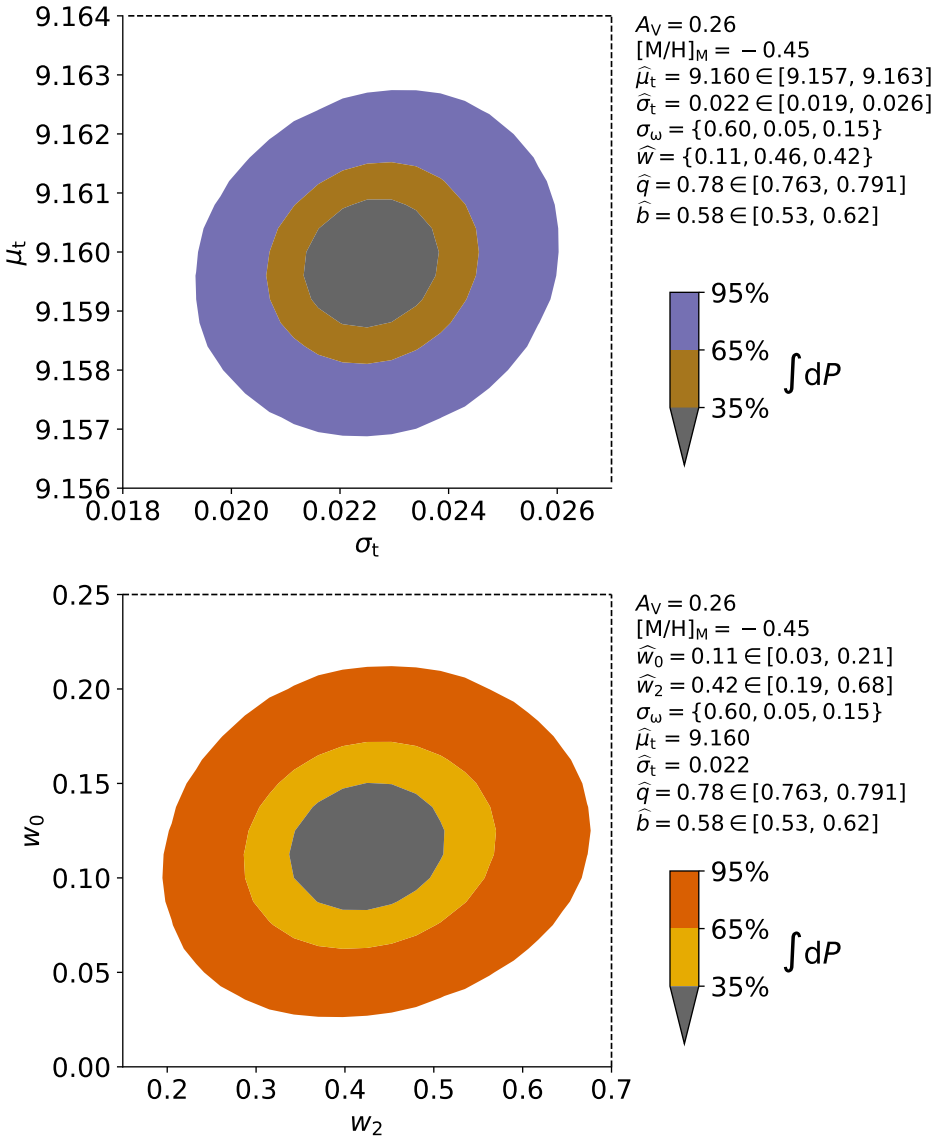

Figure 4.10 Contours designate 35%, 65% and 95% confidence regions due to marginalized Bayesian probability densities of cluster model parameters. Left panel: density over mean stellar age and age standard deviation, marginalized in all other parameters. Right panel: same, over the rotational population proportions. Intervals for $\hat{q}$ and $\hat{b}$ indicate the ranges of maximum-likelihood values of q and b over all combinations $(w_0, w_2, \mu_t, \sigma_t)$ in this figure.

of stars within clusters, as well as the internal transport processes that are linked to the rotation and evolution of individual stars. Our work offers a robust statistical framework that connects the theory of rotating star evolution and the theory of cluster formation in view of spectro-photometric data from many stars in a given cluster. Much of this work builds on the studies by G19 and BH15.

Our case study is based on the photometry and projected equatorial velocities $v_{\rm e} \sin i$ of main sequence turnoff (MSTO) stars in the intermediate-age globular cluster NGC 1846. We assume the `MIST` stellar evolution model and allow for rotational and age distributions in the cluster, constraining them using free parameters. We build a detailed statistical framework to obtain these constraints as posterior probability densities, but this entire framework operates under the fundamental assumption that the `MIST` models are accurate. Our probability distributions lead to estimates of cluster parameters that are tightly linked to the particulars of the evolutionary model.

When allowing for the cluster stars to possess a range of rotation rates, we obtain an age dispersion that is about half the previous estimates due to non-rotating models. This result agrees with the conjecture that rotational variation is at least partially responsible for eMSTOs. Still, both the age dispersion and the binary fraction that we obtain are greater than those suggested by previous, independent studies. Our relatively large age variations and binary frequencies may be compensating for other sources of physical variation that are not present (or insufficiently present) in the `MIST` models. Consideration of the fit suggests specific rotation-related processes that one may be able to tune in the

model to simultaneously improve the fit to individual data, produce a lower estimate of the binary fraction, and further lower the estimated age spread.

In sum, a comparison of theoretical probability distributions to individual star data and a comparison of inferred cluster parameters to independent estimates lead to suggestions of evolutionary processes that can improve both fits. In the remainder of this section, we offer a detailed account of this reasoning process and the evolutionary model tuning that it suggests. In future work we will apply our approach in the other direction: tuning stellar evolutionary parameters to better match the properties of cluster stars.

4.6.1 Reduced Magnetic Braking Of Low-Mass Stars

A population of single, nonrotating, coeval stars follows a line in color-magnitude space. Rotational variation, binarity, and age distributions will all broaden the main sequence, while rotational variations and age distributions can broaden the turnoff in particular.

As an example, consider that the single-age probability distributions in the left panels in Figure 4.5 are significantly narrower in color than the corresponding age-dispersed distributions in the left panels of Figure 4.7. Additionally, comparison between the left and the right panels in Figures 4.5 and 4.7 shows that binarity could be broadening the MSTO area in its own way, as well. BN15 obtain an age dispersion of 136 Myr from the eMSTO of NGC 1846 under the assumptions of zero binarity and rotation. In view of the discourse in Section 1, one wonders whether the inclusion of rotational and multiplicity degrees of freedom in the evolutionary model might allow for a narrower age

distribution. As mentioned in Section 4.5, the inclusion of these degrees of freedom, in addition to the rotational information inherent in projected equatorial velocities, yields an age dispersion estimate of $75 \in [64, 87]$ Myr. This estimate is, indeed, significantly lower than the above-mentioned estimate due to unary, non-rotating models.

A close look at Figures 4.5 and 4.7 reveals that the unary probability distributions at $m \gtrsim 21.0$ are generally narrow in color, even though they include dispersions in the initial rotation rate. This portion of the CMD contains relatively low-mass `MIST` models ($1.25\,M_\odot \lesssim M_\mathrm{i} \lesssim 1.5\,M_\odot$) that have spun down magnetically towards zero rotation rate, so that the corresponding rotational broadening is small. Age dispersion in `MIST` also does not widen this part of the distribution to match the observed color spread, although binarity does. Hence, our high estimate of the binary fraction, $\hat{b} = 0.58$. We emphasize that this estimate is driven by the lower portion of the main sequence turnoff, with magnitudes above 21.0 that correspond to masses below $1.5\,M_\odot$.

According to Figure 4.6, as m increases from 21.0, predicted probability densities become small beyond a decreasing upper limit in $v_\mathrm{e} \sin i$, although there are many observed stars beyond that limit, i.e., that remain rapidly rotating at the observed age of NGC 1846. In other words, the `MIST` implementation leads to a Kraft break that is higher on the CMD than it ought to be. We hypothesize that there is room for reduction in the magnetic braking efficiency of the `MIST` models in the dim portions of the CMD to significantly increase the models' rotational speeds and produce better-fitting probability densities. Such calibration of magnetic braking theory to an intermediate-age massive

cluster might both resemble and complement the recent calibrations of magnetic braking to open clusters by Gossage et al. (2021) and B21. Since the models with reduced braking would spin faster, the probability densities would also broaden at $m \gtrsim 21.0$ on the CMD, up to significant fractions of the current rotational broadening at $m \lesssim 21.0$. This would, in turn, reduce the need for a high binary fraction to broaden the dimmer portion of the MSTO on the CMD.

A lower estimate of the binary fraction would better agree with independent estimates for NGC 1846 and similar clusters. For example, K20 use the radial velocity (RV) variation technique to estimate that unresolved binaries constitute $\sim$6% of the stars in NGC 1846. Based on the CMD of this cluster's main sequence, Goudfrooij et al. (2009) estimate that its binary fraction is $\sim$ 15%, which is somewhat different than K20's estimate but still significantly lower than this work's value. Additionally, Galactic clusters that are similar to NGC 1846 appear to have comparatively low binary fractions, on the order of a few percent (Milone et al., 2012).

The reduction in magnetic braking that we suggest would not rotationally broaden the part of the CMD at $m \lesssim 21.0$ in Figures 4.5 and 4.7, since the stars with corresponding masses, $M_{\rm i} \gtrsim 1.5\,M_{\odot}$, do not brake very much in the first place. The poor agreement at the bright end of the MSTO must have another explanation; one possibility is

an age dispersion that is similar to this work's 75 Myr. On the other hand, several lines of evidence in Section 1.3.2 suggest that the age dispersion in NGC 1846 and similar clusters is lower than 10 Myr. In particular, BN15 find that the CMD spreads of the

cluster's sub-giant branch (SGB) and red clump (RC) regions are consistent with zero age spread. Furthermore, Bastian et al. (2013) find that clusters as young as 10 Myr and otherwise similar to NGC 1846 exhibit no evidence of on-going stellar formation. We now turn to possible physical explanations of the disagreement at the top of the turnoff other than a real age dispersion.

4.6.2 Enhanced Effect of Rotation on Internal Mixing

In looking for rotation-related processes other than magnetic braking that one could tune to further reduce the inferred age spread, we turn to the work of Brandt & Huang (2015b). Instead of `MIST`, these authors compare the `SYCLIST` library (Georgy et al., 2013) with NGC 1846 MSTO photometry. They find that the eMSTO of NGC 1846 is qualitatively consistent with instantaneous star formation, if rotational variation is present. A comparison of `MIST` and `SYCLIST` models at the MSTO suggests that rotation increases internal mixing in `SYCLIST` more than it does in `MIST`. As a result, rotating models age more slowly in `SYCLIST`, so that a distribution of rotation rates in this model library has a greater propensity to mimic an age distribution (Gossage et al., 2018, 2019; Brandt & Huang, 2015c). Future work might modify `MIST` v1.0 with enhanced internal mixing to test whether these changes to the mixing physics can explain the extent of this MSTO without any need for an age dispersion. Enhanced rotational mixing, combined with decreased magnetic braking for stars $\approx 1.3\,M_{\odot}$, could also modify the lower-end of the MSTO.

Future work could also re-construct `MIST` with a more recent version of `MESA`, a version that better incorporates the extreme effects of near-critical rotation (see the introduction to Section 4 in Paxton et al., 2019). In addition, our statistical approach offers a path to tune the coefficients that regulate the onset and the degree of mixing due to rotation in `MESA` (f_c and f_μ in Gossage et al., 2018).

4.6.3 Additional Remarks

On the whole, we have suggested several modifications to stellar evolution models, including reduction in magnetic braking for stars with $M_\mathrm{i} \lesssim 1.5\,M_\odot$ and enhancement of rotation's effect on internal chemical mixing. Future work will show how effectively such modifications can bring evolutionary models to an ideal fit with the data. It is possible, for example, that an increase in the models' internal chemical mixing will fail to account for the poorly matching points with magnitudes brighter than 21. In this case, an analysis such as ours will continue to largely model these points as part of the background distribution. As in all other such cases, the interpretation would be that the points are stars that are not included as a possibility in our stellar evolution model.

The current `MIST` library has an important limitation that might be affecting our conclusions: the library only allows for stellar models with initial dimensionless rotation rates $\omega_\mathrm{i} \leq 0.8590$. If rotation rates of a sizeable fraction of stars are above this limit, inclusion of models with $0.8590 < \omega_\mathrm{i} < 1$ would increase rotational broadening of the MSTO and consequently may reduce the required binary fraction and age spread. We

can estimate the extent of this putative effect, based on the evidence that near-critical rotation, i.e., with ω approaching 1, is quite common in clusters (Townsend et al., 2004; Bastian et al., 2017). The largest $v_{\rm e} \sin i$ measurements in our data set, $\gtrsim 200\,{\rm km/s}$, likely correspond to critical or near-critical rotation (e.g., see Section 5.5.1 and Figure A.1 in K20). Part of the uncertainty in this correspondence is due to the complications induced by gravity darkening (Townsend et al., 2004). Consequently, we can approximate the requirement that $\omega_{\rm i} > 0.8590$ with $v_{\rm e} \sin i > 200\,{\rm km/s}$. Since 32 stars in our data set meet the latter requirement, this is a rough estimate of the number of stars that would receive a more accurate treatment given models with $0.8590 < \omega_{\rm i} < 1$. This constitutes $\sim$24% of the poorly modeled stars at $m \gtrsim 21$ and high $v_{\rm e} \sin i$ (see the bottom-right panel of Figure 4.9).

In conclusion of this section, we recall from the beginning of Section 4.5 that better-fitting evolutionary models would produce cluster parameter estimates that would be more trustworthy and could be very different from this work's. In this section, we show how this can happen for binary fraction b and age dispersion σ_t. However, the same is true for cluster age μ_t and rotational population proportions w_0 and w_2. Accordingly, we recommend that the reader treat our numerical estimates of all cluster parameters with caution, pending the creation of better-fitting evolutionary models. Furthermore, we expect likelihoods of cluster parameters to drop less steeply away from the ML values for models that fit better, resulting in parameter confidence regions that are wider than the ones in Section 4.5.

4.7 Summary and Future Work

We jointly infer the age dispersion, the rotational distribution, and the binary fraction of the main sequence turnoff (MSTO) stars in the massive intermediate-age Large Magellanic Cloud cluster NGC 1846. This inference is based on cluster photometry and projected equatorial velocity measurements $v_{\rm e} \sin i$, as well as the `MIST` stellar evolution model library in combination with the `PARS` rotating star magnitude calculator. Our age dispersion estimate is $\sim 70 - 80\,$Myr, about half the earlier estimates due to non-rotating evolutionary models. This finding is consistent with the conjecture that rotational variation is at least partly responsible for the extended MSTO (eMSTO) in NGC 1846 and similar clusters. At the same time, independent lines of evidence indicate that the true age dispersion is probably even lower than the value we find. In addition, our binary fraction estimate is an order of magnitude higher than previous independent estimates for NGC 1846 and similar clusters.

Our methodology captures the pattern of the fit between the evolutionary model and the individual cluster stars in intricate detail. This, in combination with a poor quality of the fit, allows us to posit that a reduction in the magnetic braking of `MIST` models with initial masses between $\sim 1.25\,M_{\odot}$ and $\sim 1.5\,M_{\odot}$ would improve our fit to individual observed stars at magnitudes $\gtrsim 21.0$, increase rotational broadening in this portion of the CMD, and subsequently remove the need for broadening by the implausibly high inferred binary fraction.

However, due to the fact that reduction in magnetic braking would have little effect

at magnitudes $\lesssim 21.0$, this change would not improve the fit via increased rotational broadening in this brighter portion of the CMD and thus would probably not significantly alter the age dispersion estimate. On the other hand, our analysis, in combination with previous work, suggests that a greater enhancement of internal chemical mixing with rotation may provide the extra rotational broadening that would improve the fit throughout the CMD and would allow the inferred age dispersion to decrease.

Consequently, a fruitful future direction would be to calibrate magnetic braking and the effect of rotation on chemical mixing to better fit the individual data points in NGC 1846. If such work were to produce an age dispersion for NGC 1846 that is significantly lower than this work's estimate, this decrease would bring the analysis of photometry and $v_{\rm e} \sin i$ in MSTO stars closer to concordance with the evidence of $\lesssim 10$ Myr age dispersion in young clusters that are similar to NGC 1846.

In this work, we have assumed a stellar model and used it to infer cluster parameters. Future work can apply the same tools but in the other direction, or as a hierarchical model. By tuning both the cluster parameters and the stellar evolutionary model, our approach can enable new constraints on the rotation and evolution of intermediate-mass stars.

Finally, we point out that another worthwhile future direction would be to repeat this work's analysis for additional young and intermediate-age massive clusters in the Magellanic Clouds with photometry and $v_{\rm e} \sin i$ measurements, in order to provide further constraints on the theory that combines stellar evolution with cluster formation.

The `Python` code that produces the analysis in this chapter is available for download, along with the accompanying pseudo-code and usage instructions (Lipatov & Brandt, 2022).

Appendix A

Piecewise Integration in PARS

The following algorithm computes piecewise definite integrals of intensity in the azimuthal direction on the surface of a rotating star (see Section 2.3.2).

Require:

$$p_{kj}(\tilde{z},\phi) = 0 \;\text{ for }\; \{\tilde{z},\phi\} \;\text{ s.t. }\; \mu(\tilde{z},\phi) \notin m_j \equiv [\mu_j, \mu_{j+1}]$$

Ensure:

$$P_{kj}(\tilde{z}) = \int_0^{\phi_b(\tilde{z})} \mu(\tilde{z},\phi)\; p_{kj}\,(\tilde{z},\phi)\; d\phi$$

$$\text{is calculated } \forall\,\{k,j\} \text{ at a given } \tilde{z}$$

1: $a \leftarrow \sin i \,/\, n(\tilde{z})$
2: $b \leftarrow -\cos i\;\left[f \times \tilde{r}'(\tilde{z})\right] / \, n(\tilde{z})$
3: **function** $\mu(\phi)$ ▷ μ as a function of ϕ
4: **return** $a\,\cos\phi + b$
5: **function** $\phi(\mu)$ ▷ ϕ as a function of μ
6: **return** $\cos^{-1}\left[\,(\,\mu - b\,)\,/\,a\,\right]$
7: **procedure** INT(ϕ_a, ϕ_b, m_j) ▷ integrate w.r.t. ϕ on a fixed μ interval
8: **require** $\mu(\phi) \in m_j \quad \forall\phi \in [\phi_a, \phi_b]$
9: $P_{kj} \leftarrow P_{kj} + \int_{\phi_a}^{\phi_b} \mu(\tilde{z},\phi)\; p_{kj}\,(\tilde{z},\phi)\; d\phi \quad \forall k$

10: **global** $P_{kj} \leftarrow 0 \quad \forall \{k, j\}$ ▷ the integrals we aim to compute
11: $\phi_0 \leftarrow 0$ ▷ variable lower ϕ integration bound
12: $\mu_u \leftarrow \mu(\phi_0)$ ▷ fixed upper μ integration bound
13: $j \leftarrow \max_{\mu_u \in m_k} k$ ▷ index of the variable μ interval
14: **if** $a \neq 0$ **then** ▷ if μ changes during integration
15: **if** $z < z_b$ **then** ▷ if $\phi_b < \pi$
16: $\mu_l \leftarrow 0$ ▷ the fixed lower μ integration bound is zero
17: **else** ▷ if $\phi_b = \pi$
18: $\mu_l \leftarrow \mu(\pi)$ ▷ the fixed lower μ integration bound is above zero
19: **while** $\mu_j > \mu_l$ **do** ▷ while the μ interval's lower bound is above μ_l
20: INT(ϕ_0, $\phi(\mu_j)$, m_j) ▷ integrate from ϕ_0 to ϕ at the μ interval's lower bound
21: $\phi_0 \leftarrow \phi(\mu_j)$ ▷ set ϕ_0 to ϕ at the μ interval's lower bound
22: $j \leftarrow j - 1$ ▷ move to the next μ interval down
23: INT(ϕ_0, $\phi(\mu_l)$, m_j) ▷ integrate from ϕ_0 to ϕ at μ_l
24: **else** ▷ if μ is constant during integration
25: INT(ϕ_0, π, m_j) ▷ integrate from the lower ϕ integration bound to π

Appendix B

Refinement of the MIST Model Grid

B.1 Initial Stellar Parameters

Recall, from Section 4.3.2 and Equation (4.18), that we wish to compute $\rho_{jkp}(\boldsymbol{x}; \mu_t, \sigma_t)$, the theoretical probability density in observable space:

$$\rho_{jkp}(\boldsymbol{x}; \mu_t, \sigma_t) = \frac{1}{Z} \int \mathrm{d}\boldsymbol{\theta}\, \pi_{jk}(\boldsymbol{\theta}; \mu_t, \sigma_t)\; G(\boldsymbol{x} - \boldsymbol{x}(\boldsymbol{\theta}); \boldsymbol{\sigma_{xp}}). \tag{B.1}$$

Evolutionary theory implies that the observables vector $\boldsymbol{x}$ is a continuous function of stellar model parameters $\boldsymbol{\theta} \equiv (M_\mathrm{i}, r, \omega_\mathrm{i}, i, t)$, where M_i is the initial mass of the primary, r is the binary mass ratio, ω_i is the initial rotation rate of the primary, i is the inclination of its rotation axis, and t is age. In practice, however, we only evaluate $\boldsymbol{x}$ at a finite set of discrete $\boldsymbol{\theta}$. This discrete evaluation approximates the continuous $\boldsymbol{x}(\boldsymbol{\theta})$ sufficiently well when the $\boldsymbol{x}$ spacing between neighboring $\boldsymbol{\theta}$ is $\sim \boldsymbol{\sigma_x}$, i.e., on the order of minimum-error vector $\boldsymbol{\sigma_x}$. Such a spacing requirement guarantees that a discrete approximation

of the integral that involves Gaussian error kernel $G(\cdot)$ as one of the integrand factors in Equation (B.1) takes into account all $\boldsymbol{\theta}$ with $\boldsymbol{x}(\boldsymbol{\theta})$ within about the data point error of the target observables, i.e., within $\sim \boldsymbol{\sigma_{xp}} \geq \boldsymbol{\sigma_x}$ of $\boldsymbol{x}$. These are the values of $\boldsymbol{\theta}$ where $G(\boldsymbol{x} - \boldsymbol{x}(\boldsymbol{\theta}); \boldsymbol{\sigma_{xp}})$, and thus the entire integrand, is appreciable. We can state the spacing requirement in terms of the error kernel: $G(\boldsymbol{x} - \boldsymbol{x}(\boldsymbol{\theta}); \boldsymbol{\sigma_x})$ at neighboring $\boldsymbol{\theta}$ have to overlap or at least come close to overlapping. This requirement is uniform in $\boldsymbol{x}$ space; however, it translates to potentially non-uniform separations in $\boldsymbol{\theta}$ space. In particular, when the derivatives of $\boldsymbol{x}(\boldsymbol{\theta})$ with respect to $\boldsymbol{\theta}$ have high magnitudes, neighboring $\boldsymbol{\theta}$ have to be close.

The original set of discrete `MIST` models does not satisfy our spacing requirement. For example, Figure 4.4 shows `PARS` observables for these models at a fixed age, two inclinations, and zero binary mass ratio. In this figure, consider the magnitude spacing between neighboring discrete $\boldsymbol{\theta}$ that differ only in $M_{\rm i}$. This spacing is often significantly greater than the magnitude uncertainty σ_m, especially at bright magnitudes, where a stellar model is likely to have high $M_{\rm i}$ and to be near the end of its main sequence life. Thus, we have to refine the $M_{\rm i}$ grid at high $M_{\rm i}$. At the same time, we may be able to coarsen the grid at low $M_{\rm i}$. Similar reasoning applies to all other components of $\boldsymbol{\theta}$.

The spacing requirement on the `MIST` grid in this section is numerically similar to the spacing characteristics of the `PARS` grid in Section 4.2.3: both the `PARS` grid and the final `MIST` grid should have observable distances between neighboring models that are on the order of observation error. These requirements, however, are distinct and

have different reasons. In the former case, the requirement makes the interpolation on the PARS grid more accurate. In the latter case, it makes the subsequent integration, described in Section 4.3.4, more accurate.

We aim to satisfy the above spacing requirement with a new grid of initial model parameters $\boldsymbol{\theta}' \equiv (M_\mathrm{i}, r, \omega_\mathrm{i}, i)$, but without making the grid so large as to be computationally prohibitive. To do so, we begin with a relatively sparse $\{M_\mathrm{i}, \omega_\mathrm{i}, i\}$ grid at constant t and $r = 0$ and calculate $\boldsymbol{x}\,(M_\mathrm{i}, \omega_\mathrm{i}, i)$ via the interpolations on the MIST and PARS grids in Section 4.2. We then refine and coarsen the grid in M_i, according to the following algorithm. First, for each pair of neighboring M_i, we calculate the maximum absolute difference in any one observable over all (ω_i, i), divided by three minimum-error standard deviations, $d \equiv \max|\Delta\boldsymbol{x}/3\boldsymbol{\sigma}_{\boldsymbol{x}}|$. We then divide the corresponding interval into $\lceil d \rceil$ equal segments. For all original intervals with a size greater than $10^{-4}\,M_\odot$, we re-calculate the observables on the new grid. In the remaining cases, we interpolate the observables in M_i. We order the new, subdivided intervals according to decreasing d and go through them until we can merge one with a neighboring interval without violating $d \leq 1$. After the merge, we re-start at the beginning of the ordered interval list and repeat the procedure until no merges are possible.

For t_M, values of age t in the original MIST grid, we repeat the refinement and coarsening procedure in ω_i, then go on cycling through the three elements of $\{M_\mathrm{i}, \omega_\mathrm{i}, i\}$, until the grid satisfies $d \leq 1$ everywhere. Here, the threshold interval sizes are 10^{-4} and $10^{-4}\,\mathrm{rad}$ for ω_i and i, respectively. Our iterative refinement procedure takes exponentially longer

with the addition of each new model dimension. Thus, for t not in the original `MIST` grid, we only refine and coarsen in $M_{\rm i}$, adopting the $\omega_{\rm i}$ and i grids from the largest $t_{\rm M}$ that satisfies $t_{\rm M} < t$.

We now propose an approximation that will allow us to refine the binary mass ratio r grid independently of all other $\boldsymbol{\theta}$ grid dimensions, so that we do not have to include r in the iterative refinement procedure. Specifically, solely for the purpose of r grid refinement, we approximate the radiative flux from a star as proportional to its initial mass to some power s, e.g. $\mathcal{F} \propto M_{\rm i}^s$ for the primary. Under this approximation, Equation (4.15) can be written as

$$m = -2.5 \log\left(\mathcal{F}_{\rm p} + \mathcal{F}_{\rm c}\right) = m_{\rm p} - \frac{2.5}{\ln 10} \ln\left(1 + \frac{\mathcal{F}_{\rm c}}{\mathcal{F}_{\rm p}}\right) \approx m_{\rm p} - \frac{\mathcal{F}_{\rm c}}{\mathcal{F}_{\rm p}} = m_{\rm p} - r^s, \qquad \text{(B.2)}$$

where $\mathcal{F}_{\rm p}$, $\mathcal{F}_{\rm c}$, and $m_{\rm p}$ stand for the flux of the primary, the flux of the secondary, and the magnitude of the primary, respectively. Furthermore, the functionality of this procedure is not impaired when we approximate $\ln 10$ as 2.5 and retain only the first term in the Taylor expansion of the natural logarithm around $\mathcal{F}_{\rm c}/\mathcal{F}_{\rm p} = 0$. Equation (B.2) suggests that if we subdivide $r^s \in [0, 1]$ into at least $1/3\sigma_m \approx 34$ intervals, the resulting $\{M_{\rm i}, r, \omega_{\rm i}, i\}$ grid should satisfy $d \leq 1$ in the r dimension. In practice, the condition is satisfied for $r \in [0, r_1]$ with 66 intervals, $s = 4.6$ and $r_1 \geq 0.98$ for all t. For each t, $r \in [0, r_1]$ becomes the range over which we integrate. Figure B.1 shows the maximum distances between neighboring models in each of the $\boldsymbol{\theta}'$ dimensions for the resulting grid at a specific value of t that is also one of the ages in the original `MIST`

library. Although parameter spacing between models is large in some parts of Figure B.1, such as at low r, this corresponds to small enough distances in observable space that the integration remains accurate. We emphasize that we do not use approximation $\mathcal{F} \propto M_{\rm i}^s$ for magnitude calculations, which are outlined in Section 4.2.4.

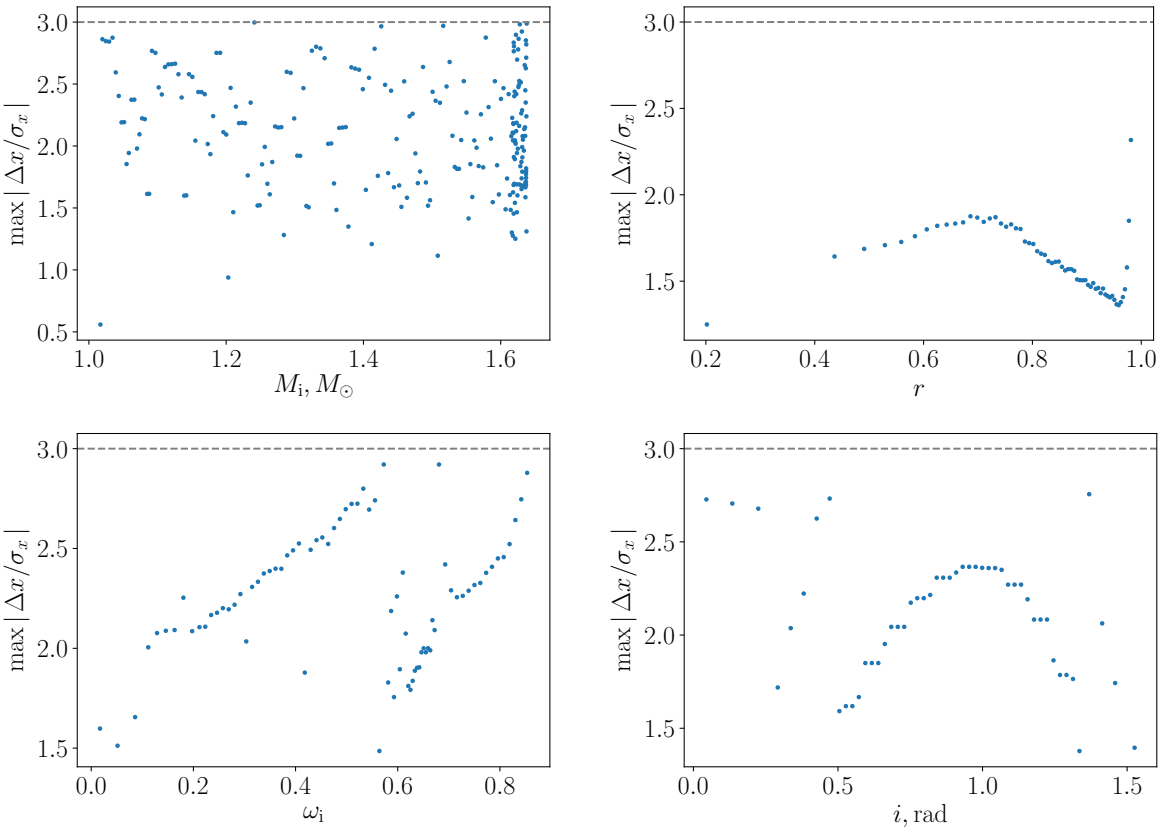

Figure B.1 Observable distances between neighboring models in each $\boldsymbol{\theta}'$ dimension, maximized over the remaining 3 dimensions. The corresponding 4-dimensional $\boldsymbol{\theta}'$ grid results from the model grid refinement procedure in Section 4.3.3 at $\log t = 9.1544$, one of the ages in the original `MIST` library. Horizontal axes show interval midpoints. Note that the density of models in the $M_{\rm i}$ dimension is especially high near the maximum value of $M_{\rm i}$, where the derivatives of magnitude and color as functions of this parameter can be large. For each $\boldsymbol{\theta}'$ dimension, the distances generally do not vary by more than a factor of 2, indicating a relative uniformity in the accuracy of integration on this grid.

B.2 Refinement of Model Age

Our spacing requirement for the $\boldsymbol{\theta'}$ grid is rather stringent. It is necessary if one cannot assume that numerical integration in Equation (B.1) is performed sequentially in each component of $\boldsymbol{\theta'}$. We make the requirement more lenient with respect to t by integrating with respect to this parameter after all the others in Equation (B.1). To characterize the resulting requirement on spacing in t, we re-write Equation (B.1) as

$$\rho_{jkp}(\boldsymbol{x};\mu_t,\sigma_t) = \frac{1}{Z}\int \mathrm{d}t\,\bar{\pi}(t;\mu_t,\sigma_t)\,\rho_{jkp}(\boldsymbol{x};t), \tag{B.3}$$

where

$$\rho_{jkp}(\boldsymbol{x};t) = \int \mathrm{d}\boldsymbol{\theta'}\,\pi_{jk}(\boldsymbol{\theta'})\,G\left(\boldsymbol{x}-\boldsymbol{x}(\boldsymbol{\theta'};t);\boldsymbol{\sigma_{xp}}\right) \tag{B.4}$$

is the theoretical probability density over observable space at age t, based on a Gaussian error kernel with width $\boldsymbol{\sigma_{xp}}$.

Let us define Θ as the full range of $\boldsymbol{\theta}$, $\Theta(t)$ as the subset of this range at age t, and $\Theta(a,t)$ as $\Theta(t)$ restricted to EEP a. Every $\Theta(a,t)$ extends over all i and r, but the requirement that EEP equals a selects for an age-specific range of M_i and ω_Mi. We further define $X(a,t)$ as the image of $\Theta(a,t)$ due to the function $\boldsymbol{x}(\boldsymbol{\theta})$. The continous volume $X(t) = \cup_a X(a,t)$ in $\boldsymbol{x}$-space is an isochrone in the general sense of Section 4.2.1, specified for three observables, i.e., components of $\boldsymbol{x}$, and four model parameters, i.e., components of $\boldsymbol{\theta'}$. Section 4.2.1 introduces the idea that shortest distances on the CMD between traditional isochrones, which are parametrized by M_i, are at fixed EEPs. Here, we extend this concept to three observable dimensions and four isochrone parameters.

Thus, we define the $\boldsymbol{x}$-space distance $\Delta\boldsymbol{x}(a, t_1, t_2)$ between the $t = t_1$ and $t = t_2$ isochrones at fixed EEP $= a$ as the average distance between $X(a, t_1)$ and $X(a, t_2)$; the overall distance $\Delta\boldsymbol{x}(t_1, t_2)$ between these isochrones is the same average, taken across all a. Intuitively, accurate integration in Equation (B.3) requires the order of $\Delta\boldsymbol{x}(t_1, t_2)$ to be no larger than about the minimum error $\boldsymbol{\sigma_x}$ for neighboring t_1 and t_2.

More formally, we require that appreciable $\rho_{jkp}(\boldsymbol{x}; t)$ in Equation (B.3) at neighboring t overlap in $\boldsymbol{x}$-space. This is equivalent to the error kernel formulation of the spacing requirement in Section B.1, with $\boldsymbol{\theta}$ replaced by t and $G(\boldsymbol{x}-\boldsymbol{x}(\boldsymbol{\theta}); \boldsymbol{\sigma_x})$ replaced by $\rho_{jkp}(\boldsymbol{x}; t)$. To determine where $\rho_{jkp}(\boldsymbol{x}; t)$ is appreciable, let us assume that the prior $\pi_{jk}(\boldsymbol{\theta'})$ in Equation (B.4) is appreciable over the entirety of $\Theta(t)$. In this case, Equation (B.4) tells us that the locus of points in $\boldsymbol{x}$-space with appreciable $\rho_{jkp}(\boldsymbol{x}; t)$ is $X(t)$ broadened by at least $\boldsymbol{\sigma_x}$. More precisely, $\rho_{jkp}(\boldsymbol{x}; t)$ is the convolution of a function that is appreciable solely over $X(t)$ and an error kernel that is at least as wide as $G\left(\boldsymbol{x} - \boldsymbol{x}(\boldsymbol{\theta'}; t); \boldsymbol{\sigma_x}\right)$. Hence, we confirm our intuition that $X(t)$ at neighboring t should be separated by $\sim \boldsymbol{\sigma_x}$. This is equivalent to the formulation of the spacing requirement in Section B.1, with $\boldsymbol{x}(\boldsymbol{\theta})$ replaced by $X(t)$.

The original `MIST` age grid is spaced uniformly with $\Delta\left(\log t_{\rm M}\right) = 0.020$. We start with the portion of this grid between $\log t_{\rm M} = 9.0537$ and $\log t_{\rm M} = 9.2550$ and insert intermediate ages, so that the new grid is spaced uniformly with $\Delta\left(\log t\right) = 0.005$. Additionally, for the lowest 5 values of $\log t_{\rm M}$, we append the grid with $(3/4)\log t_{\rm M} + (1/4)\left[\log t_{\rm M} + \Delta\left(\log t\right)\right]$. The resulting grid becomes our age grid for the rest of the arti-

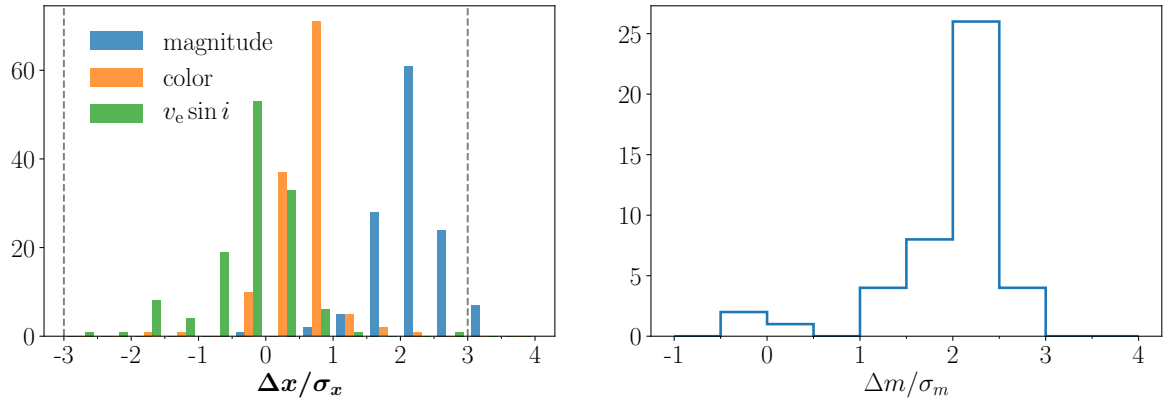

Figure B.2 Left panel: histogram of differences in each observable, averaged over $\boldsymbol{\theta}'$ and scaled by minimum-error standard deviation, between $\log t = 9.1544$ and $\log t = 9.1594$. Each difference is taken at one of the EEPs where each age has at least one stellar model. Most absolute differences for color and $v_e \sin i$ are below 1; most differences for magnitudes are below 3. Negative values for color and $v_e \sin i$ correspond to EEPs where average value of the observable decreases with increasing age. The space between vertical dashed lines is equal to the width of the Gaussian error kernels in our numerical integration procedure. Right panel: histogram of scaled differences in magnitude (as opposed to differences in each observable) between model grids for all neighbor pairs on the age grid (as opposed to one pair, as in the left panel). Absolute differences are below 3, indicating that integration in t is likely accurate.

cle. For two neighboring ages t_1 and t_2 on this grid, the left panel of Figure B.2 presents the distribution of $\Delta\boldsymbol{x}(a, t_1, t_2)$ across all a. This figure shows that most differences are no larger than a few $\boldsymbol{\sigma_x}$, suggesting that the isochrone spacing requirement is met for t_1 and t_2. For every such pair of neighboring ages on the grid, we further obtain $\Delta\boldsymbol{x}(t_1, t_2)$ and focus on $\Delta m(t_1, t_2)/\sigma_m$, generally the largest component of $\Delta\boldsymbol{x}(t_1, t_2)/\boldsymbol{\sigma_x}$. The right panel of Figure B.2 shows that the absolute value of $\Delta m(t_1, t_2)/\sigma_m$ across all neighbor pairs (t_1, t_2) is less than 3, supporting the idea that the isochrone requirement is met for all age neighbor pairs.

The main focus of this subsection has been to check and make sure that our inter-

polation between isochrones results in a model grid on which we accurately compute the probability densities, e.g., in Equations B.3 and B.4. We also want to check that this interpolation is accurate, in itself. To this end, we compare models on the isochrone at $\log t = 9.1544$ from the original `MIST` grid with the models we obtain by interpolating between this isochrone's neighbors, at $\log t = 9.1342$ and $\log t = 9.1745$. Specifically we compare two model parameters that determine magnitude – luminosity L and specially averaged radius $R_{\rm M}$. Figure B.3 shows that most differences in luminosity between the original isochrone and the interpolated version are $\sim 1\%$ and most differences in radius are lower. In the course of actual interpolation that yields our model grid, the average age difference between known isochrones is half the difference in this test case. Thus, we expect interpolation errors to be even lower for the actual interpolation procedure, by a factor of ~ 4 if linear and quadratic terms dominate the local series expansions of luminosity and radius as functions of age.

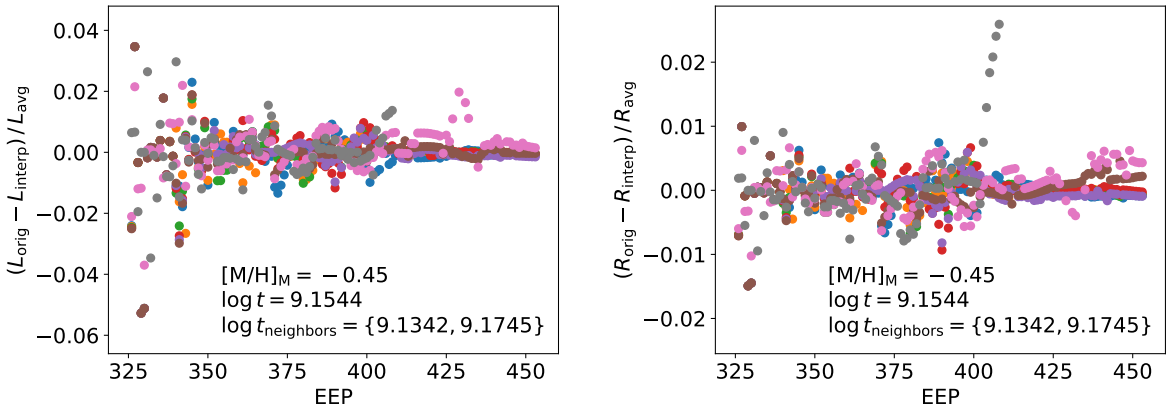

Figure B.3 Accuracy of interpolation between the isochrones. Left panel: proportional difference between the luminosity at the original `MIST` isochrone with $\log t = 9.1544$ and the luminosity that is interpolated between the isochrone's neighbors in age space. Right panel: same, for the specially averaged radius $R_{\rm M}$. Average luminosity is $L_{\rm avg} = (L_{\rm orig} + L_{\rm interp})/2$ and average radius is similar. Different colors indicate different initial rotational velocities in the same way they do in Figure 4.4. For example, gray markers correspond to $\omega_{\rm M} = 0.7$, pink – to $\omega_{\rm M} = 0.6$, and so on. Average distance between known isochrones in the course of actual interpolation that produces our model grid is half the distance in this test case, so that we expect the former interpolation procedure to be significantly more accurate than that which is pictured here.

Appendix C

Computation of Cluster Parameters

C.1 Likelihood

From the latter portions of Section 4.4.2, recall that we want to compute integrals of the form

$$P(\mu_t, \sigma_t) = \int \mathrm{d}w_0 \, \mathrm{d}w_2 \, P(\boldsymbol{\phi}') \propto \int \mathrm{d}w_0 \, \mathrm{d}w_2 \, \mathcal{L}(\boldsymbol{\phi}'), \tag{C.1}$$

where the likelihood function $\mathcal{L}$ over a limited set of cluster parameters $\boldsymbol{\phi}' = \{\mu_t, \sigma_t, w_0, w_2\}$ is

$$\mathcal{L}(\boldsymbol{\phi}') = \int \mathrm{d}q \, \mathrm{d}b \, \mathcal{L}(\boldsymbol{\phi}) \tag{C.2}$$

and the full likelihood function over all cluster parameters $\boldsymbol{\phi} = \{q, b, \mu_t, \sigma_t, w_0, w_2\}$ is the product of data point likelihood factors ϱ_p:

$$\mathcal{L}(\boldsymbol{\phi}) = \prod_p^n \varrho_p. \tag{C.3}$$

We also recall that Bayesian probability density is $P(\boldsymbol{\phi}) = \mathcal{L}(\boldsymbol{\phi}) Z_{\mathcal{L}}^{-1}$, where $Z_{\mathcal{L}}$ is a normalization constant, equal to

$$Z_{\mathcal{L}} = \int \mathrm{d}\boldsymbol{\phi}\, \mathcal{L}(\boldsymbol{\phi}). \tag{C.4}$$

In order to evaluate the rightmost integral in Equation (C.1), we first wish to determine $\mathcal{L}(\boldsymbol{\phi})$ up to a multiplicative constant for all $\boldsymbol{\phi}$ where the function is appreciable. The naive approach to this task, suggested by Equation (C.3), can easily encounter numerical overflow and underflow, due to the fact that the number of factors $n = 2353$ in Equation (C.3) is large and the fact that the differences between individual factors are also large.

In particular, standard, positive floating point values in the `Python` programming language cannot be closer than $f_{\min} = 2.2 \times 10^{-308}$ to zero or farther than $f_{\max} = 1.8 \times 10^{308}$ from zero. Thus, for example, if each factor is below $\sqrt[n]{f_{\min}} = 0.74$, Equation (C.3) evaluates to zero. If each factor is above $\sqrt[n]{f_{\max}} = 1.35$, the equation evaluates to infinity. In practice, $\log \varrho_p$ are more or less randomly distributed throughout some range in our implementation of the analysis. When $\boldsymbol{\phi}$ is closer to its maximum-likelihood value, this range is higher, and products of the form $\prod_p^k \varrho_p$ with $k \in [1, \ldots, n]$ can evaluate to values greater than $f_{\max}$.

A solution to this problem that is relatively slow but guaranteed to work involves taking the logarithm of every ϱ_p, at every $\boldsymbol{\phi}$. In this case, we can first evaluate

$$\ln \mathcal{L}(\boldsymbol{\phi}) = \sum_p^n \ln \varrho_p \quad \forall \boldsymbol{\phi}, \tag{C.5}$$

then compute likelihood as

$$\exp\left[\ln \mathcal{L}(\boldsymbol{\phi}) - \max_{\boldsymbol{\phi}} \ln \mathcal{L}(\boldsymbol{\phi})\right], \tag{C.6}$$

which is Equation (C.3) divided by $\max_{\boldsymbol{\phi}} \mathcal{L}$.

We offer an alternate solution, one that is faster by about a factor of two in our implementation. Towards this end, we define $\rho_{jp}(\mu_t, \sigma_t) = \sum_i w_i \, \rho_{ijp}(\boldsymbol{x_p}; \mu_t, \sigma_t)$ and use equations (4.33) and (4.34) to express likelihood factors ϱ_p as

$$\varrho_p \equiv \varrho_p(\boldsymbol{\phi}) = 1 + qA_p(\boldsymbol{\phi}') + qbB_p(\boldsymbol{\phi}'), \tag{C.7}$$

where $\boldsymbol{\phi}' \equiv \{\mu_t, \sigma_t, w_0, w_2\}$,

$$A_p(\boldsymbol{\phi}') = \frac{\rho_{0p}(\mu_t, \sigma_t)}{\rho_{\mathrm{b}p}(\boldsymbol{x_p})} - 1, \tag{C.8}$$

and

$$B_p(\boldsymbol{\phi}') = \frac{\rho_{1p}(\mu_t, \sigma_t) - \rho_{0p}(\mu_t, \sigma_t)}{\rho_{\mathrm{b}p}(\boldsymbol{x_p})}. \tag{C.9}$$

For each $\boldsymbol{\phi}'$, we choose some constant C, divide every ρ_p by this constant and multiply the resulting factors together. The constant should be large enough that there is no overflow, i.e.,

$$\prod_p^n \frac{\varrho_p}{C} = \frac{1}{C^n} \prod_p^n \varrho_p < f_{\max} \quad \forall k, q, b, \tag{C.10}$$

yet small enough that the maximum of the product is much greater than $f_{\min}$:

$$\max_{q,b} \prod_p^n \frac{\varrho_p}{C} = \frac{1}{C^n} \max_{q,b} \prod_p^n \varrho_p \gg f_{\min}. \tag{C.11}$$

In this case, the likelihood in Equation (C.3) is divided by C^n. To obtain a value of C that satisfies Equations (C.10) and (C.11), we aim to find the maximum of $\mathcal{L}$ across b and q, for a given set of the remaining cluster parameters $\boldsymbol{\phi}'$. Towards this goal, we use

Equations (C.3), (4.34), (C.8), and (C.9) to write down

$$\begin{aligned} \frac{\partial \ln \mathcal{L}}{\partial q} &= \sum_p \frac{1}{q + q_p(b)} \quad \text{and} \\ \frac{\partial \ln \mathcal{L}}{\partial b} &= \sum_p \frac{1}{b + b_p(q)}, \end{aligned} \tag{C.12}$$

where

$$\begin{aligned} q_p(b) &= \frac{1}{A_p + B_p b}, \\ b_p(q) &= \frac{1/q + A_p}{B_p}, \end{aligned} \tag{C.13}$$

A_p and B_p are given by Equations (C.8) and (C.9), and we have suppressed arguments $\boldsymbol{\phi}'$. Further differentiating (C.12), we get

$$\begin{aligned} \frac{\partial^2 \ln \mathcal{L}}{\partial q^2} &= -\sum_p \frac{1}{\left[q + q_p(b)\right]^2} \quad \text{and} \\ \frac{\partial^2 \ln \mathcal{L}}{\partial b^2} &= -\sum_p \frac{1}{\left[b + b_p(q)\right]^2}. \end{aligned} \tag{C.14}$$

One can show that neither $q_p(b)$ nor $b_p(q)$ can be on the open interval $(-1, 0)$. Thus, as long as $q \in (0, 1)$ and $b \in (0, 1)$, second derivatives in Equation (C.14) are always defined and negative. This suggests that the likelihood function has a single extremum on this domain – a maximum. We assume that the latter assertion is true, solely for the purposes of finding a constant to divide ϱ_p. We set both derivatives in Equation (C.12) to zero and solve the system of equations using a modified Powell's method to find $\tilde{q}$ and $\tilde{b}$ – the

values of q and b where the likelihood reaches $\tilde{\mathcal{L}}$, which is probably its maximum. We set $C = \sqrt[n]{\tilde{\mathcal{L}}}$ and perform the procedure discussed around Equations (C.10) and (C.11). Consider that, in the course of this procedure, we reduce the order of magnitude of every ϱ_p by the average order of magnitude at maximum likelihood:

$$\log \frac{\varrho_p(q, b)}{C} = \log \varrho_p(q, b) - \frac{1}{n} \sum_p \log \varrho_p(\tilde{q}, \tilde{b}). \tag{C.15}$$

In other words, even at $(\tilde{q}, \tilde{b})$, the average order of magnitude is now zero. Thus, Equation (C.11) is satisfied, and it is very likely that Equation (C.10) is satisfied as well. On the other hand, the reduction in the magnitude of ϱ_p has made underflow more probable. We can think of the multiplication on the left hand side expression of Equation (C.10) as a biased pseudo-random walk in the magnitude of the running product, starting at zero. The longer the walk, the more likely it is to reach $\log f_{\min}$ and result in underflow. To minimize the probability of such an occurrence, we split the multiplication into 10 products, each composed of $\sim$ 235 factors. Having completed the multiplication, we compute

$$\ln \mathcal{L}(\boldsymbol{\phi}) = \ln \prod_p \frac{\varrho_p(\boldsymbol{\phi})}{C(\boldsymbol{\phi}')} + \ln \tilde{\mathcal{L}}(\boldsymbol{\phi}'), \tag{C.16}$$

and determine $\hat{\boldsymbol{\phi}}$, where $\mathcal{L}(\boldsymbol{\phi})$ has its maximum over $\boldsymbol{\phi}$. The additive term $\ln \tilde{\mathcal{L}}$ removes the effect of dividing ϱ_p by $\boldsymbol{\phi}'$-dependent C and $\boldsymbol{\phi}$ have been restored as arguments. We compute the logarithm of $\mathcal{L}(\boldsymbol{\phi})$, since the function itself could be larger than $f_{\max}$.

In addition to maximum log likelihood in Equation (C.16), we now aim to calculate the logarithm of the likelihood marginalized in q and b, on a grid of $\boldsymbol{\phi}'$:

$$\ln \mathcal{L}(\boldsymbol{\phi}') = \ln \int \mathrm{d}q \, \mathrm{d}b \prod_p \frac{\varrho_p(\boldsymbol{\phi})}{C(\boldsymbol{\phi}')} + \ln \tilde{\mathcal{L}}(\boldsymbol{\phi}'), \tag{C.17}$$

with $\mathcal{L}(\boldsymbol{\phi})$ and $\mathcal{L}(\boldsymbol{\phi}')$ as defined in Equations (C.3) and (C.2), respectively. The integrand in Equation (C.17) is a negligible fraction of its maximum over most of its domain. When this kind of an integrand is approximated via Monte Carlo methodologies, frequent sampling of the domain where the integrand is large ensures accuracy. Although our integration method is deterministic, we will similarly sample the domain densely where the integrand is large by making the (q, b) grid in such portions of the domain relatively fine. We apply the following procedure to find a grid that meets this requirement. First, we define a subset of the domain $\mathcal{R} \equiv [q_0, q_1] \cap [b_0, b_1]$ where the grid will be fine. We initialize $q_0 = b_0 = 0$, $q_0 = q_1 = 1$, an equally spaced grid of 11 values between q_0 and q_1, and similarly in the b dimension. Then, at every other value of each component of $\boldsymbol{\phi}'$, we compute the integrand value I versus the fraction of the total integral that accumulates at the locations where the integrand is above I, fit this dependence to a linear spline, and use the latter to compute I corresponding to 99.9% of the total integral. We next narrow down $\mathcal{R}$ as much as possible under the condition that the integrand is always below I outside the new $\mathcal{R}$. In each dimension, we allot 11 points to $\mathcal{R}$ as before and 4 additional points to the complement of $\mathcal{R}$ and repeat computation of I. We repeat this procedure, starting with the narrowing down of $\mathcal{R}$, until the new $\mathcal{R}$ does not differ much from its value in the previous iteration. After three iterations, this procedure results in $[q_0, q_1] = [0.70, 0.84]$ and $[b_0, b_1] = [0.40, 0.76]$.

At this point, we perform the integral in Equation (C.17) for every $\boldsymbol{\phi}'$, on an equally

spaced grid of 21 values in each dimension to cover $\mathcal{R}$ and 7 additional points allotted to the complement of $\mathcal{R}$ in each dimension. We check that 99.9% of the integral still always falls within $\mathcal{R}$, so that most of the integration is over the fine grid. We then subtract from $\ln \mathcal{L}(\boldsymbol{\phi}')$ its maximum and take the exponent of the result, which gives us a new version of $\mathcal{L}(\boldsymbol{\phi}')$, one that is below $f_{\max}$ and with a maximum significantly above $f_{\min}$. It turns out that $\mathcal{L}(\boldsymbol{\phi}')$ is unimodal.

C.2 Bayesian Probability Density

Computation of $\mathcal{L}(\boldsymbol{\phi}')$ in Section C.1 is on a grid of 21 equally spaced values in each component of $\boldsymbol{\phi}'$, centered around $\hat{\boldsymbol{\phi}}'$. This grid covers set $\mathcal{T} \cap \mathcal{W}$. Here, $\mathcal{T}$ is the intersection of $\mu_t \in [9.154, 9.165]$ and $\sigma_t \in [0.036, 0.047]$; $\mathcal{W}$ is the intersection of $w_0 \in [0.025, 0.225]$ and $w_2 \in [0.4, 0.9]$. However, the integral in Equation (C.4), for example, is over a much larger formal region of normalization in $\boldsymbol{\phi}$. To calculate such integrals, we make the following approximations with respect to $\mathcal{L}(\boldsymbol{\phi}')$ outside $\mathcal{T} \cap \mathcal{W}$.

We assume that when the likelihood integral in Equation (C.1) is limited to $\mathcal{W}$, it is multiplied by some value that is slightly less than 1 and doesn't depend on (μ_t, σ_t). This ensures that the limited integral, which we call $\mathcal{L}(\mu_t, \sigma_t)$, is still proportional to $P(\mu_t, \sigma_t)$. We now wish to compute the corresponding normalization constant,

$$Z_t = \int \mathrm{d}\mu_t \, \mathrm{d}\sigma_t \, \mathcal{L}(\mu_t, \sigma_t). \tag{C.18}$$

On $\mathcal{T}$, we numerically approximate the integral in Equation (C.18) in the usual fashion. To estimate the integral outside $\mathcal{T}$, we calculate $p = \mathcal{L}_{\mathrm{p}}/\mathcal{L}_{\max}$. Here, $\mathcal{L}_{\mathrm{p}}$ is the average

$\mathcal{L}(\mu_t, \sigma_t)$ on the perimeter of $\mathcal{T}$ and $\mathcal{L}_{\max}$ is the maximum $\mathcal{L}(\mu_t, \sigma_t)$ over $\mathcal{T}$. We then approximate $P(\mu_t, \sigma_t)$ as a two-dimensional normal density distribution with zero covariance and a maximum at the location of $\mathcal{L}_{\max}$. In this case, cumulative density over the locations where density drops below fraction p of its peak is simply equal to p. Thus, we assume that fraction p of the integral in Equation (C.18) is outside $\mathcal{T}$, so that

$$Z_t = \frac{1}{1-p} \int_{\mathcal{T}} \mathrm{d}\mu_t \, \mathrm{d}\sigma_t \, \mathcal{L}(\mu_t, \sigma_t) \tag{C.19}$$

and $P(\mu_t, \sigma_t) = \mathcal{L}(\mu_t, \sigma_t)/Z_t$. We exchange the roles of $\mathcal{T}$ and $\mathcal{W}$ in the above procedure to calculate $P(w_0, w_2)$. Figure 4.10 presents the 35%, 65% and 95% confidence regions for $P(\mu_t, \sigma_t)$ and $P(w_0, w_2)$.

Bibliography

Ackerman, A. S., & Marley, M. S. 2001, ApJ, 556, 872, doi: 10.1086/321540

Allard, F., Hauschildt, P. H., Alexander, D. R., & Starrfield, S. 1997, ARA&A, 35, 137, doi: 10.1146/annurev.astro.35.1.137

Anders, E., & Grevesse, N. 1989, GeoCoA, 53, 197, doi: 10.1016/0016-7037(89)90286-X

Arny, T. 1990, Vistas in Astronomy, 33, 211, doi: https://doi.org/10.1016/0083-6656(90)90021-Y

Asplund, M., Grevesse, N., Sauval, A. J., & Scott, P. 2009, ARA&A, 47, 481, doi: 10.1146/annurev.astro.46.060407.145222

Aufdenberg, J. P., Mérand, A., Coudé du Foresto, V., et al. 2006, ApJ, 645, 664, doi: 10.1086/504149

Bacon, R., Accardo, M., Adjali, L., et al. 2010, in Society of Photo-Optical Instrumentation Engineers (SPIE) Conference Series, Vol. 7735, Ground-based and Airborne Instrumentation for Astronomy III, ed. I. S. McLean, S. K. Ramsay, & H. Takami, 773508, doi: 10.1117/12.856027

Baraffe, I., Chabrier, G., Barman, T. S., Allard, F., & Hauschildt, P. H. 2003, A&A, 402, 701, doi: 10.1051/0004-6361:20030252

Barnes, J. W. 2009, ApJ, 705, 683, doi: 10.1088/0004-637X/705/1/683

Barnes, J. W., & Fortney, J. J. 2003, ApJ, 588, 545, doi: 10.1086/373893

Barnes, J. W., Linscott, E., & Shporer, A. 2011, ApJS, 197, 10, doi: 10.1088/0067-0049/197/1/10

Basri, G. 2000, ARA&A, 38, 485, doi: 10.1146/annurev.astro.38.1.485

Bastian, N., Cabrera-Ziri, I., Davies, B., & Larsen, S. S. 2013, MNRAS, 436, 2852, doi: 10.1093/mnras/stt1779

Bastian, N., & de Mink, S. E. 2009, MNRAS, 398, L11, doi: 10.1111/j.1745-3933.2009.00696.x

Bastian, N., & Lardo, C. 2018, ARA&A, 56, 83, doi: 10.1146/annurev-astro-081817-051839

Bastian, N., & Niederhofer, F. 2015, MNRAS, 448, 1863, doi: 10.1093/mnras/stv116

Bastian, N., & Silva-Villa, E. 2013, MNRAS, 431, L122, doi: 10.1093/mnrasl/slt024

Bastian, N., Cabrera-Ziri, I., Niederhofer, F., et al. 2017, MNRAS, 465, 4795, doi: 10.1093/mnras/stw3042

Batalha, N., Rooney, C., Blanch, N. R., & MacDonald, R. 2022, natashabatalha/picaso: Release 2.3, v2.3.0, Zenodo, doi: 10.5281/zenodo.6419943

Batalha, N. E., Marley, M. S., Lewis, N. K., & Fortney, J. J. 2019, ApJ, 878, 70, doi: 10.3847/1538-4357/ab1b51

Bate, M. R., Bonnell, I. A., & Bromm, V. 2002, MNRAS, 332, L65, doi: 10.1046/j.1365-8711.2002.05539.x

—. 2003, MNRAS, 339, 577, doi: 10.1046/j.1365-8711.2003.06210.x

Bohlin, R. C., Gordon, K. D., & Tremblay, P. E. 2014, PASP, 126, 711, doi: 10.1086/677655

Bouchaud, K., Domiciano de Souza, A., Rieutord, M., Reese, D. R., & Kervella, P. 2020, A&A, 633, A78, doi: 10.1051/0004-6361/201936830

Brandt, G. M., Brandt, T. D., Dupuy, T. J., Li, Y., & Michalik, D. 2021, AJ, 161, 179, doi: 10.3847/1538-3881/abdc2e

Brandt, T. D., & Huang, C. X. 2015a, ApJ, 807, 24, doi: 10.1088/0004-637X/807/1/24

—. 2015b, ApJ, 807, 25, doi: 10.1088/0004-637X/807/1/25

—. 2015c, ApJ, 807, 58, doi: 10.1088/0004-637X/807/1/58

Breimann, A. A., Matt, S. P., & Naylor, T. 2021, ApJ, 913, 75, doi: 10.3847/1538-4357/abf0a3

Brott, I., de Mink, S. E., Cantiello, M., et al. 2011, A&A, 530, A115, doi: 10.1051/0004-6361/201016113

Cabrera-Ziri, I., Bastian, N., Longmore, S. N., et al. 2015, MNRAS, 448, 2224, doi: 10.1093/mnras/stv163

Cargile, P. A., Conroy, C., Johnson, B. D., et al. 2020, ApJ, 900, 28, doi: 10.3847/1538-4357/aba43b

Carmichael, T. W., Quinn, S. N., Mustill, A. J., et al. 2020, AJ, 160, 53, doi: 10.3847/1538-3881/ab9b84

Carroll, B. W., & Ostlie, D. A. 2007, An Introduction to Modern Astrophysics, 2nd edn. (Addison-Wesley, San Francisco: Pearson)

Castelli, F., & Kurucz, R. L. 2004, New Grids of ATLAS9 Model Atmospheres. https://arxiv.org/abs/astro-ph/0405087

Chabrier, G. 2003, PASP, 115, 763, doi: 10.1086/376392

Chabrier, G., & Baraffe, I. 2000, ARA&A, 38, 337, doi: 10.1146/annurev.astro.38.1.337

Che, X., Monnier, J. D., Zhao, M., et al. 2011, ApJ, 732, 68, doi: 10.1088/0004-637X/732/2/68

Chilcote, J., Pueyo, L., De Rosa, R. J., et al. 2017, AJ, 153, 182, doi: 10.3847/1538-3881/aa63e9

Choi, J., Dotter, A., Conroy, C., et al. 2016, ApJ, 823, 102, doi: 10.3847/0004-637X/823/2/102

Christensen-Dalsgaard, J. 2021, Living Reviews in Solar Physics, 18, 2, doi: 10.1007/s41116-020-00028-3

Chulkov, D. 2021, MNRAS, 501, 769, doi: 10.1093/mnras/staa3601

Claret, A. 2000, A&A, 363, 1081

—. 2018, A&A, 618, A20, doi: 10.1051/0004-6361/201833060

Corsaro, E., Lee, Y.-N., García, R. A., et al. 2017, Nature Astronomy, 1, 0064, doi: 10.1038/s41550-017-0064

Cranmer, S. R., & Owocki, S. P. 1995, ApJ, 440, 308, doi: 10.1086/175272

Crossfield, I. J. M. 2014, A&A, 566, A130, doi: 10.1051/0004-6361/201423750

D'Antona, F., Di Criscienzo, M., Decressin, T., et al. 2015, MNRAS, 453, 2637, doi: 10.1093/mnras/stv1794

Dantona, F., & Mazzitelli, I. 1985, ApJ, 296, 502, doi: 10.1086/163470

D'Antona, F., Milone, A. P., Tailo, M., et al. 2017, Nature Astronomy, 1, 0186, doi: 10.1038/s41550-017-0186

de Juan Ovelar, M., Gossage, S., Kamann, S., et al. 2019, MNRAS, 2735, doi: 10.1093/mnras/stz3128

Díaz, C. G., González, J. F., Levato, H., & Grosso, M. 2011, A&A, 531, A143, doi: 10.1051/0004-6361/201016386

Dolphin, A. E. 2002, MNRAS, 332, 91, doi: 10.1046/j.1365-8711.2002.05271.x

Domiciano de Souza, A., Kervella, P., Moser Faes, D., et al. 2014, A&A, 569, A10, doi: 10.1051/0004-6361/201424144

Dotter, A. 2016, ApJS, 222, 8, doi: 10.3847/0067-0049/222/1/8

Eggenberger, P. 2013, in European Physical Journal Web of Conferences, Vol. 43, European Physical Journal Web of Conferences, 01005, doi: 10.1051/epjconf/20134301005

Eislöffel, J., & Scholz, A. 2007, in Star-Disk Interaction in Young Stars, ed. J. Bouvier & I. Appenzeller, Vol. 243, 241–248, doi: 10.1017/S174392130700960X

Ekström, S., Meynet, G., Chiappini, C., Hirschi, R., & Maeder, A. 2008, A&A, 489, 685, doi: 10.1051/0004-6361:200809633

Ekström, S., Georgy, C., Eggenberger, P., et al. 2012, A&A, 537, A146, doi: 10.1051/0004-6361/201117751

Elvey, C. T. 1930, ApJ, 71, 221, doi: 10.1086/143249

Endal, A. S., & Sofia, S. 1976, ApJ, 210, 184, doi: 10.1086/154817

Espinosa Lara, F., & Rieutord, M. 2011, A&A, 533, A43, doi: 10.1051/0004-6361/201117252

Fitzpatrick, E. L. 1999, PASP, 111, 63, doi: 10.1086/316293

Fodor, F. 1999, Geometriae Dedicata, 74, 139, doi: 10.1023/A:1005091317243

Fortney, J. J., Helled, R., Nettelmann, N., et al. 2018, in Saturn in the 21st Century, ed. K. H. Baines, F. M. Flasar, N. Krupp, & T. Stallard (Cambridge University Press), 44–68, doi: 10.1017/9781316227220.003

Freedman, R. S., Lustig-Yaeger, J., Fortney, J. J., et al. 2014, ApJS, 214, 25, doi: 10.1088/0067-0049/214/2/25

Georgy, C., Ekström, S., Granada, A., et al. 2013, A&A, 553, A24, doi: 10.1051/0004-6361/201220558

Georgy, C., Granada, A., Ekström, S., et al. 2014, A&A, 566, A21, doi: 10.1051/0004-6361/201423881

Giesers, B., Kamann, S., Dreizler, S., et al. 2019, A&A, 632, A3, doi: 10.1051/0004-6361/201936203

Glebocki, R., & Gnacinski, P. 2005, VizieR Online Data Catalog, III/244

Godoy-Rivera, D., Pinsonneault, M. H., & Rebull, L. M. 2021, arXiv e-prints, arXiv:2101.01183. https://arxiv.org/abs/2101.01183

Gossage, S., Conroy, C., Dotter, A., et al. 2018, ApJ, 863, 67, doi: 10.3847/1538-4357/aad0a0

Gossage, S., Dotter, A., Garraffo, C., et al. 2021, ApJ, 912, 65, doi: 10.3847/1538-4357/abebdf

Gossage, S., Conroy, C., Dotter, A., et al. 2019, ApJ, 887, 199, doi: 10.3847/1538-4357/ab5717

Goudfrooij, P., Girardi, L., & Correnti, M. 2017, ApJ, 846, 22, doi: 10.3847/1538-4357/aa7fb7

Goudfrooij, P., Puzia, T. H., Chandar, R., & Kozhurina-Platais, V. 2011a, ApJ, 737, 4, doi: 10.1088/0004-637X/737/1/4

Goudfrooij, P., Puzia, T. H., Kozhurina-Platais, V., & Chandar, R. 2009, AJ, 137, 4988, doi: 10.1088/0004-6256/137/6/4988

—. 2011b, ApJ, 737, 3, doi: 10.1088/0004-637X/737/1/3

Graham, R. L., Lubachevsky, B. D., Nurmela, K. J., & Östergård, P. R. 1998, Discrete Mathematics, 181, 139

Gratton, R. G., Carretta, E., & Bragaglia, A. 2012, A&A Rv, 20, 50, doi: 10.1007/s00159-012-0050-3

Green, G. M., Schlafly, E. F., Finkbeiner, D. P., et al. 2014, ApJ, 783, 114, doi: 10.1088/0004-637X/783/2/114

Hayashi, C., & Nakano, T. 1963, Progress of Theoretical Physics, 30, 460, doi: 10.1143/PTP.30.460

Healy, B. F., & McCullough, P. R. 2020, ApJ, 903, 99, doi: 10.3847/1538-4357/abbc03

Helled, R., Schubert, G., & Anderson, J. D. 2009, Planet. Space Sci., 57, 1467, doi: 10.1016/j.pss.2009.07.008

Herbig, G. H., & Spalding, John F., J. 1955, ApJ, 121, 118, doi: 10.1086/145969

Howard, R., Gilman, P. I., & Gilman, P. A. 1984, ApJ, 283, 373, doi: 10.1086/162315

Hunter, J. D. 2007, Computing in Science & Engineering, 9, 90, doi: 10.1109/MCSE.2007.55

Johansson, F., et al. 2018, mpmath: a Python library for arbitrary-precision floating-point arithmetic (version 1.1.0)

Kaehler, H. 1978, in The HR Diagram - The 100th Anniversary of Henry Norris Russell, ed. A. G. D. Philip & D. S. Hayes, Vol. 80, 303

Kamann, S., Bastian, N., Gossage, S., et al. 2020, MNRAS, 492, 2177, doi: 10.1093/mnras/stz3583

Kippenhahn, R. 1977, A&A, 58, 267

Klessen, R. S. 2001, ApJ, 556, 837, doi: 10.1086/321626

Kraft, R. P. 1967, ApJ, 150, 551, doi: 10.1086/149359

Kraus, S., Le Bouquin, J.-B., Kreplin, A., et al. 2020, ApJL, 897, L8, doi: 10.3847/2041-8213/ab9d27

Kroupa, P. 2001, MNRAS, 322, 231, doi: 10.1046/j.1365-8711.2001.04022.x

Kumar, S. S. 1963, ApJ, 137, 1121, doi: 10.1086/147589

Lagrange, A. M., Gratadour, D., Chauvin, G., et al. 2009, A&A, 493, L21, doi: 10.1051/0004-6361:200811325

Lagrange, A. M., Bonnefoy, M., Chauvin, G., et al. 2010, Science, 329, 57, doi: 10.1126/science.1187187

Larson, R. B. 2010, Reports on Progress in Physics, 73, 014901, doi: 10.1088/0034-4885/73/1/014901

Lew, B. W. P., Apai, D., Zhou, Y., et al. 2020, AJ, 159, 125, doi: 10.3847/1538-3881/ab5f59

Lipatov, M., & Brandt, T. D. 2020a, mlipatov/paint_atmospheres, v1.2.0, Zenodo, doi: 10.5281/zenodo.3955185

—. 2020b, ApJ, 901, 100, doi: 10.3847/1538-4357/aba8f5

—. 2022, mlipatov/calc_cluster: ApJ Publication 2022, v1.0.0, Zenodo, doi: 10.5281/zenodo.6633623

Lipatov, M., Brandt, T. D., & Gossage, S. 2022, ApJ, 934, 105, doi: 10.3847/1538-4357/ac78e1

Luhman, K. L. 2014, ApJL, 786, L18, doi: 10.1088/2041-8205/786/2/L18

Lupu, R., Freedman, R., Gharib-Nezhad, E., & Molliere, P. 2022, High resolution opacities for H2/He atmospheres, Zenodo, doi: 10.5281/zenodo.6600976

Mackey, A. D., & Broby Nielsen, P. 2007, MNRAS, 379, 151, doi: 10.1111/j.1365-2966.2007.11915.x

Maeder, A., & Meynet, G. 2000, ARA&A, 38, 143, doi: 10.1146/annurev.astro.38.1.143

Mang, J., Gao, P., Hood, C. E., et al. 2022, ApJ, 927, 184, doi: 10.3847/1538-4357/ac51d3

Marley, M., Saumon, D., Morley, C., & Fortney, J. 2018, Sonora 2018: Cloud-free, solar composition, solar C/O substellar atmosphere models and spectra, nc_m+0.0_co1.0_v1.0, Zenodo, doi: 10.5281/zenodo.1309035

Marley, M. S., & McKay, C. P. 1999, Icarus, 138, 268, doi: 10.1006/icar.1998.6071

Marley, M. S., Saumon, D., Visscher, C., et al. 2021, ApJ, 920, 85, doi: 10.3847/1538-4357/ac141d

Martocchia, S., Cabrera-Ziri, I., Lardo, C., et al. 2018, MNRAS, 473, 2688, doi: 10.1093/mnras/stx2556

Masuda, K. 2015, ApJ, 805, 28, doi: 10.1088/0004-637X/805/1/28

Matt, S. P., Brun, A. S., Baraffe, I., Bouvier, J., & Chabrier, G. 2015, ApJL, 799, L23, doi: 10.1088/2041-8205/799/2/L23

Meynet, G., & Maeder, A. 2000, A&A, 361, 101. https://arxiv.org/abs/astro-ph/0006404

Milone, A. P., Piotto, G., Bedin, L. R., et al. 2012, A&A, 540, A16, doi: 10.1051/0004-6361/201016384

Moe, M., & Di Stefano, R. 2013, ApJ, 778, 95, doi: 10.1088/0004-637X/778/2/95

Monnier, J. D. 2003, Reports on Progress in Physics, 66, 789, doi: 10.1088/0034-4885/66/5/203

Monnier, J. D., Zhao, M., Pedretti, E., et al. 2007, Science, 317, 342, doi: 10.1126/science.1143205

Mucciarelli, A., Carretta, E., Origlia, L., & Ferraro, F. R. 2008, AJ, 136, 375, doi: 10.1088/0004-6256/136/1/375

Muench, A. A., Alves, J., Lada, C. J., & Lada, E. A. 2001, ApJL, 558, L51, doi: 10.1086/323420

Nakajima, T., Oppenheimer, B. R., Kulkarni, S. R., et al. 1995, Nature, 378, 463, doi: 10.1038/378463a0

Natta, A., & Testi, L. 2001, A&A, 376, L22, doi: 10.1051/0004-6361:20011055

Naylor, T., & Jeffries, R. D. 2006, MNRAS, 373, 1251, doi: 10.1111/j.1365-2966.2006.11099.x

Ni, D. 2018, A&A, 613, A32, doi: 10.1051/0004-6361/201732183

Niederhofer, F., Georgy, C., Bastian, N., & Ekström, S. 2015, MNRAS, 453, 2070, doi: 10.1093/mnras/stv1791

Noyes, R. W., Hartmann, L. W., Baliunas, S. L., Duncan, D. K., & Vaughan, A. H. 1984, ApJ, 279, 763, doi: 10.1086/161945

Oppenheimer, B. R., Kulkarni, S. R., Matthews, K., & Nakajima, T. 1995, Science, 270, 1478, doi: 10.1126/science.270.5241.1478

Orlov, A. A. 1961, Soviet Ast., 4, 845

Owocki, S. P., Cranmer, S. R., & Blondin, J. M. 1994, ApJ, 424, 887, doi: 10.1086/173938

Paxton, B., Bildsten, L., Dotter, A., et al. 2011, ApJS, 192, 3, doi: 10.1088/0067-0049/192/1/3

Paxton, B., Cantiello, M., Arras, P., et al. 2013, ApJS, 208, 4, doi: 10.1088/0067-0049/208/1/4

Paxton, B., Marchant, P., Schwab, J., et al. 2015, ApJS, 220, 15, doi: 10.1088/0067-0049/220/1/15

Paxton, B., Smolec, R., Schwab, J., et al. 2019, ApJS, 243, 10, doi: 10.3847/1538-4365/ab2241

Phillips, M. W., Tremblin, P., Baraffe, I., et al. 2020, A&A, 637, A38, doi: 10.1051/0004-6361/201937381

Piatti, A. E. 2020, A&A, 642, A114, doi: 10.1051/0004-6361/202038625

Piatti, A. E., & Bailin, J. 2019, AJ, 157, 49, doi: 10.3847/1538-3881/aaf572

Piotto, G. 2009, in The Ages of Stars, ed. E. E. Mamajek, D. R. Soderblom, & R. F. G. Wyse, Vol. 258, 233–244, doi: 10.1017/S1743921309031883

Pompéia, L., Hill, V., Spite, M., et al. 2008, A&A, 480, 379, doi: 10.1051/0004-6361:20064854

Prentice, A. J. R., & Ter Haar, D. 1971, MNRAS, 151, 177, doi: 10.1093/mnras/151.2.177

Press, W. H., Teukolsky, S. A., Vetterling, W. T., & Flannery, B. P. 2007, Numerical Recipes 3rd Edition: The Art of Scientific Computing, 3rd edn. (New York, NY, USA: Cambridge University Press)

Raghavan, D., McAlister, H. A., Henry, T. J., et al. 2010, ApJS, 190, 1, doi: 10.1088/0067-0049/190/1/1

Rieutord, M., & Espinosa Lara, F. 2009, Communications in Asteroseismology, 158, 99

Rieutord, M., Espinosa Lara, F., & Putigny, B. 2016, Journal of Computational Physics, 318, 277, doi: 10.1016/j.jcp.2016.05.011

Robbins-Blanch, N., Kataria, T., Batalha, N. E., & Adams, D. J. 2022, arXiv e-prints, arXiv:2204.03545. https://arxiv.org/abs/2204.03545

Rodrigo, C., Solano, E., & Bayo, A. 2012, SVO Filter Profile Service Version 1.0, Tech. rep., International Virtual Observatory Alliance, doi: 10.5479/ADS/bib/2012ivoa.rept.1015R

Rolleston, W. R. J., Trundle, C., & Dufton, P. L. 2002, A&A, 396, 53, doi: 10.1051/0004-6361:20021088

Royer, F., Gerbaldi, M., Faraggiana, R., & Gómez, A. E. 2002a, A&A, 381, 105, doi: 10.1051/0004-6361:20011422

Royer, F., Grenier, S., Baylac, M. O., Gómez, A. E., & Zorec, J. 2002b, A&A, 393, 897, doi: 10.1051/0004-6361:20020943

Rubele, S., Girardi, L., Kozhurina-Platais, V., et al. 2013, MNRAS, 430, 2774, doi: 10.1093/mnras/stt079

Salpeter, E. E. 1955, ApJ, 121, 161, doi: 10.1086/145971

Sanghavi, S., & Shporer, A. 2018, ApJ, 866, 28, doi: 10.3847/1538-4357/aadf94

Saumon, D., Hubbard, W. B., Burrows, A., et al. 1996, ApJ, 460, 993, doi: 10.1086/177027

Saumon, D., & Marley, M. S. 2008, ApJ, 689, 1327, doi: 10.1086/592734

Schlafly, E. F., Green, G., Finkbeiner, D. P., et al. 2014, ApJ, 786, 29, doi: 10.1088/0004-637X/786/1/29

Snellen, I. A. G., Brandl, B. R., de Kok, R. J., et al. 2014, Nature, 509, 63, doi: 10.1038/nature13253

Sorahana, S., Yamamura, I., & Murakami, H. 2013, ApJ, 767, 77, doi: 10.1088/0004-637X/767/1/77

Speagle, J. S. 2020, MNRAS, 493, 3132, doi: 10.1093/mnras/staa278

Tan, X., & Showman, A. P. 2021, MNRAS, 502, 678, doi: 10.1093/mnras/stab060

Tannock, M. E., Metchev, S., Heinze, A., et al. 2021, AJ, 161, 224, doi: 10.3847/1538-3881/abeb67

Tomisaka, K. 2000, ApJL, 528, L41, doi: 10.1086/312417

Toon, O. B., McKay, C. P., Ackerman, T. P., & Santhanam, K. 1989, J. Geophys. Res., 94, 16287, doi: 10.1029/JD094iD13p16287

Townsend, R. H. D., Owocki, S. P., & Howarth, I. D. 2004, MNRAS, 350, 189, doi: 10.1111/j.1365-2966.2004.07627.x

van Belle, G. T. 2012, A&A Rv, 20, 51, doi: 10.1007/s00159-012-0051-2

Van der Swaelmen, M., Hill, V., Primas, F., & Cole, A. A. 2013, A&A, 560, A44, doi: 10.1051/0004-6361/201321109

van der Walt, S., Colbert, S. C., & Varoquaux, G. 2011, Computing in Science & Engineering, 13, 22, doi: 10.1109/MCSE.2011.37

van Dyk, D. A., Degennaro, S., Stein, N., Jefferys, W. H., & von Hippel, T. 2009, Annals of Applied Statistics, 3, 117, doi: 10.1214/08-AOAS219SUPP

van Leeuwen, F. 2007, A&A, 474, 653, doi: 10.1051/0004-6361:20078357

Villaume, A., Brodie, J., Conroy, C., Romanowsky, A. J., & van Dokkum, P. 2017, ApJL, 850, L14, doi: 10.3847/2041-8213/aa970f

Virtanen, P., Gommers, R., Oliphant, T. E., et al. 2020, Nature Methods, 17, 261, doi: 10.1038/s41592-019-0686-2

von Zeipel, H. 1924, MNRAS, 84, 665, doi: 10.1093/mnras/84.9.665

Walmswell, J. J., Eldridge, J. J., Brewer, B. J., & Tout, C. A. 2013, MNRAS, 435, 2171, doi: 10.1093/mnras/stt1444

Yoon, J., Peterson, D. M., Kurucz, R. L., & Zagarello, R. J. 2010, ApJ, 708, 71, doi: 10.1088/0004-637X/708/1/71

Zhang, Z., Liu, M. C., Marley, M. S., Line, M. R., & Best, W. M. J. 2021, ApJ, 916, 53, doi: 10.3847/1538-4357/abf8b2

Zhao, M., Monnier, J. D., & Che, X. 2010, Proceedings of the International Astronomical Union, 6, 44–55, doi: 10.1017/S1743921311009963

Zorec, J., & Royer, F. 2012, A&A, 537, A120, doi: 10.1051/0004-6361/201117691

Zorec, J., Frémat, Y., Domiciano de Souza, A., et al. 2011, A&A, 526, A87, doi: 10.1051/0004-6361/201015691

Zucker, C., Speagle, J. S., Schlafly, E. F., et al. 2020, A&A, 633, A51, doi: 10.1051/0004-6361/201936145

—. 2019, ApJ, 879, 125, doi: 10.3847/1538-4357/ab2388